國立交通大學

機械工程學系

博士論文

固態層狀結構中微觀熱傳現象之分析

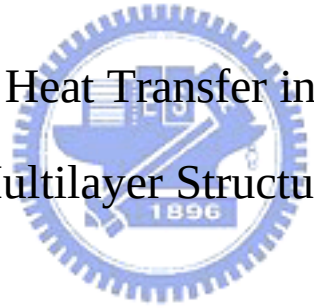

Microscale Heat Transfer in Solid-State Multilayer Structures

研 究 生：吳世國

指導教授：曲新生 教授

中華民國九十三年十月

固態層狀結構中微觀熱傳現象之分析

學生：吳世國　　指導教授：曲新生

摘　要

本文主要是探討固態層狀結構中之微觀熱傳現象。首先，我們分別從巨觀和微觀的觀點探討介電薄膜內的熱傳行為。聲子輻射熱傳模式、傅立葉定律以及熱波理論分別被用來分析介電薄膜內的暫態熱傳現象。當薄膜厚度小於聲子平均自由徑(mean free path)時，由於聲子穿透傳播(ballistic transport)的緣故，聲子輻射熱傳模式預測到在邊界處會有溫度不連續的情形產生。相反地，當薄膜厚度遠大於聲子平均自由徑時，聲子輻射熱傳模式會趨近於傅立葉定律。結果顯示，當薄膜厚度與聲子平均自由徑的比值大於 100 時，描述巨觀熱傳現象之傅立葉定律便很適合處理介電薄膜內的熱傳問題。

其次，本文分析了雙層同心微圓管中微觀熱傳的現象。應用聲子輻射熱傳方程式模擬固態材料內的熱傳導行為。同時以散異模型(diffuse mismatch model)來描述兩層材料交界處的介面條件。結果顯示，當微圓管厚度縮小時，材料的熱傳導係數也隨之降低。而數值模擬的結果與實驗數據非常吻合。除了尺寸效應外，微圓管曲率的縮減也會使得材料的熱傳導係數降低。不過，微圓管的尺寸及曲率對介面熱阻的影響並不明顯。

接下來，我們推導出二維聲子輻射熱傳方程式，用以模擬微圓管內的熱傳行為。本研究檢視了微圓管尺寸和曲率對其熱傳導係數的影響。結果顯示，當微圓管的高度或管壁厚度小於或相當於聲子平

均自由徑時，聲子穿透傳播主宰了整個熱傳行為。尺寸的縮減造成等效熱傳導係數變小。不過，曲率對等效熱傳導係數的影響並不明顯。

將上述微觀熱傳的分析擴展，本研究檢視了尺寸效應對熱電微冷卻器性能的影響。本研究應用了聲子輻射熱傳方程式和散異模型來模擬超晶格薄膜、超晶格奈米線以及超晶格奈米管內的微觀熱傳行為。結果顯示，具超晶格結構的熱電材料會因其組成材料層厚度降低而使得其等效熱傳導係數下降。更進一步地，當超晶格薄膜、超晶格奈米線和超晶格奈米管的厚度相同時，超晶格奈米線和超晶格奈米管具有較低的等效熱傳導係數。因此，超晶格奈米線或是超晶格奈米管很有潛力製成高性能熱電裝置。

由以上分析得知，在奈米尺度的系統內，尺寸縮減會造成等效熱傳導係數降低。因此，為了確保散熱的能力，我們利用了由微觀熱傳模式所計算出的等效熱傳導係數去推估薄膜/基材系統的表面溫度。結果顯示，即使在薄膜/基材介面處有急劇的溫度變化，逆運算法仍能準確地預測薄膜/基材系統的表面狀況。當輸入的溫度資訊為正確值(即沒有量測誤差)時，溫度感測器的擺放位置和介面熱阻對逆運算法的準確性影響非常小。不過，若是有量測誤差存在時，不準度便會被介面熱阻和溫度感測器的擺放位置給放大。

Microscale Heat Transfer in Solid-State Multilayer Structures

Student: Shih-Kuo Wu Advisor: Hsin-Sen Chu

ABSTRACT

This thesis discusses microscale heat transfer phenomena in solid-state multilayer structures. First, we discuss heat transfer in dielectric thin films from both macroscopic and microscopic points of view. Phonon radiative transfer model as well as Fourier law and thermal wave theory are utilized to analyze the transient heat conduction phenomena in dielectric thin films. Phonon radiative transfer model predicts temperature discontinuities at boundaries due to its ballistic nature when the thickness of the film is less than the phonon mean free path. In contrast, the results predicted by the phonon radiative transfer model approaches to that of Fourier law when the thickness of the film is much grater than the phonon mean free path. The results show that as the ratio of thin film thickness to phonon mean free path, L/Λ, is greater than 100, Fourier law, a macroscopic heat transfer model, is a good approximation to deal with the transient heat transfer problems in dielectric thin films.

Second, we present a numerical analysis on estimating the microscale heat transfer in a two-layer concentric circular tube. The phonon radiative heat conduction equation and the diffuse mismatch model are utilized to simulate the microscale heat conduction in solids. The results show that the reduction of layer thickness will reduce the effective thermal conductivity. Moreover, the numerical predictions agree with the experimental data very well. Besides the size effect, the reduction of curvature will also reduce the effective thermal conductivity. However, the size and curvature effects on the interface thermal resistance are not significant.

Third, we concern microscale heat transfer in micro tubes. A two-dimensional

equation of phonon radiative transfer was derived to simulate this system. The influences of size and curvature on thermal conductivity are examined closely. The results show that ballistic transport dominates if the tube thickness or height is comparable or less than phonon mean free path. The reduction of size reduces the effective thermal conductivity. However, the curvature effect on the effective thermal conductivity is not significant.

Extending the foregoing analysis on microscale heat transfer, size effects on the performance of thermoelectric micro coolers are examined in detail. EPRT and DMM are utilized to model the microscale heat transfer in thin film, nano wire and nano tube superlattices. The results show that the effective thermal conductivity of thermoelectric materials in superlattice structures decreases as the layer thickness decreases. In addition, the thermal conductivities of nano wire and nano tube superlattices are less than that of thin film superlattices when they have the same layer thickness. Thus, nano wire and nano tube superlattices are potential materials for high performance thermoelectric devices.

From the above studies, it is observed that the reduction of size causes the reduction of thermal conductivity. Thus, to assure the heat dissipation ability, we utilize the effective thermal conductivity calculated by the microscale heat transfer model to estimate the surface temperature in thin-film/substrate systems. Numerical results show that the inverse method accurately estimates surface conditions and temperature distributions in a two-layer system even with an abrupt temperature drop at the interface. Sensor locations and interface thermal resistance only slightly affect the accuracy of the inverse estimation when the exact input data (without measurement errors) are applied. However, the inaccuracy might be amplified by the interface thermal resistance and sensor locations if measurement errors exist.

誌　謝

首先要感謝的是恩師　曲新生博士。恩師除了指導我學術上的研究之外，對於做人處世方面更是我等學習的標竿。其次要感謝的是系上熱流組諸位老師以及論文口試委員翁政義、陳朝光、王國雄、陳發林、盧定昶、陳俊勳諸位教授對本論文的批評指教，使得其內容更加完整且充實。

此外，要特別感謝森溥、凌家、志文、志平、志堅等學長對我的關心與勉勵。也感謝時明與建評以及諸位學弟妹們多年來在課業上與生活上的協助。

最後要感謝的是我的家人。在這段為期不短的求學過程中，如果沒有爸爸、媽媽、弟弟、妹妹的支持與體諒，我是絕不可能順利完成學業的。僅以此文獻給所有關心我、照顧我的人。

TABLE OF CONTENTS

LIST OF TABLES

LIST OF FIGURES

NOMENCLATURE

C	volumetric specific heat [$J/K\,m^3$]
D	density of states [$1/m^3$]
$\vec{e}_v$	unit vector of the phonon velocity, $\vec{e}_v = \vec{v}/v$
E_{int}	estimation error at the interface, $\lvert T_{est} - T_{exa} \rvert / T_{exa}$
f	phonon distribution function
F	force [N]
G	coupling factor
$\hbar$	Planck's constant divided by $2p$ = 1.055 ×10^{-34} [Js]
I	phonon intensity [$W/m^2 sr$]
ITR	interface thermal resistance [m^2K/W]
J	phonon radiosity, $\int I\, dm$
k	thermal conductivity [$W/(m\,K)$]
k_B	Boltzmann constant = 1.381 ×10^{-23} [J/K]
k_{eff}	effective thermal conductivity [$W/(m\,K)$]
L	film thickness [m]
L_1	thickness of layer 1, $L_1 = r_b - r_i$
L_2	thickness of layer 2, $L_2 = r_o - r_b$
L_a	tube height $[m]$
L_f	thickness of the thin-film/substrate system $[m]$
L_{f1}	location of the interface in the thin-film/substrate system $[m]$
L_r	first sensor location [m]

m	mass $[kg]$
q	heat flux $[W/m^2]$
$\overline{Q}$	dimensionless heat flux, $L_f q / kT_L$
Q_a	dimensionless heat flux, $q / s_s(T_r^4 - T_0^4)$
Q_T	total net radial heat transfer, $[W]$
r	radial distance $[m]$
r_a	tube thickness, $r_a = r_o - r_i$
r_i, R_i	inner radius $[m]$
r_b	the location of the interface $[m]$
r_o, R_o	outer radius $[m]$
R	radius of nano wire superlattices $[m]$
R_{ij}	reflectivity from medium i to medium j
S	Seebeck coefficient $[V/K]$
t	time $[s]$
T	temperature $[K]$
T_o	initial temperature; temperature of the outer surface $[K]$
T_i	temperature of the inner surface $[K]$
v	phonon group velocity $[m/s]$
w	weighting factor
x	coordinate direction and length $[m]$
Y_1,Y_2	temperature histories at the first and second sensor locations
z	axial distance $[m]$
ZT	thermoelectric figure of merit

Greek Symbols

a	thermal diffusivity [m^2/s]
a_{ij}	transmissivity at the interface from layer i to layer j
Δq	dimensionless temperature difference in the interface
e_{LJ}	well depth of the potential
z	polar angle [rad]
h	$h = \sin z \sin j$
q	dimensionless temperature, T/T_L
q_a	dimensionless temperature, $(T-T_0)/(T_r-T_0)$
k	constant
l , L	phonon mean free path [m]
l_d	dominant phonon wavelength [m]
m	$m = \sin z \cos j$
x	dimensionless length, x/L_f
x_a	dimensionless length, x/L
x_1	dimensionless interface location, L_{f1}/L_f
x_r	dimensionless first sensor location, L_r/L_f
r	density [kg/m^3]
s	bound of random error
$\overline{s}$	mean interfacial roughness [m]
s_e	electrical conductivity [sm]
s_{LJ}	equilibrium separation parameter
s_s	Stefan-Boltzmann constant for phonons = 50.47 [W/m^2K^4]

t	dimensionless time, $a_1 t / L_f^2$
t_a	dimensionless time, $t/(L/v)$
t_N	relaxation time of elastically scattering [s]
t_R	relaxation time [s]
f_{LJ}	Lennard-Jones potential function
j	azimuth angle [rad]
y	$h = \cos z$
w	angular frequency of phonons [$1/s$]
v	random error
W	solid angle

Superscripts

0	equilibrium
+	forward direction
-	backward direction
est	estimated
exa	exact

Subscripts

p	phonon polarization index
coll	collision

1. INTRODUCTION

1.1 Motivation

Owing to the trend towards miniaturization in engineering systems, the study of microscale phenomena has attracted significant attention for the past two decades. Reducing sizes have increased device switching speed, and thus have also increased heat generation [1]. Since the temperature of solid-state devices significantly influences their performance, heat dissipation becomes a vital issue. Experimental results of thermal conductivity measurements demonstrate that the thermal conductivities of thin films are frequently smaller than those of corresponding bulk materials [2-4]. This phenomenon implies that the Fourier law of heat conduction, which is derived from the macroscopic point of view, is inappropriate for treating microscale heat transfer in solids. Thus, heat transport mechanisms and thermophysical properties of materials must be known prior to dealing with microscale heat transfer problems.

From a microscopic perspective, heat carriers in solids include both free electrons and phonons. In metals, free electrons dominate heat conduction, while phonons are the major heat carriers in dielectrics and semiconductors [3, 5]. The macroscopic heat transfer model such as Fourier law requires hundreds of thousands of energy carrier collisions. However, if the length and/or time scales are shrinking into the micro/nano scale, there is no sufficient space or time for the process of heat transport to occur. The macroscale heat transfer model can result in a significant error in the calculated heat transfer rate or temperature distribution in the devices involving the miniaturization length and time scales.

Since multilayer structures have been widely used in many solid-state devices

such as microelectronic, optical, and superconducting devices, it is important to realize the microscale heat transfer in multilayer structures. In practical engineering applications, thin films are almost always on supporting substrates and/or in multilayer configurations. Besides the size effect, interface thermal resistance also is important in determining heat flow in thin-film/substrate systems. For example, a restriction in heat flow from the superconducting film can cause a transition from the superconducting state to the normal state during operation of the device, resulting in device failure. The interface thermal resistance prevents heat transporting from one medium to another and this thus reduces the overall thermal conductivity of materials. It is undesired for heat dissipation. However, the lower thermal conductivity makes high performance thermoelectric devices.

Thermoelectric devices are solid-state energy conversion devices. Since they have no moving parts, they have no noise and are reliable. They have small size and light weight. Moreover, unlike the conventional compressor-based refrigerators, thermoelectric refrigerators use no CFC gas or any other refrigerant gas so they are environmentally friendly [6]. Owing to these advantages, the thermoelectric devices have found a large range of applications [7].

To describe the performance of the thermoelectric materials, an index called the dimensionless thermoelectric figure of merit, ZT, was defined as [8]

$$ZT = \frac{S^2 \sigma_e T}{k}, \tag{1-1}$$

where S is the Seebeck coefficient, σ_e is the electrical conductivity, T is the temperature and k is the thermal conductivity. To increase the performance of a thermoelectric device, the figure of merit must be maximizing. In general, metals have high electrical conductivity and high Seebeck coefficient. However, their high

thermal conductivity makes the thermoelectric devices impracticable. Materials with high Seebeck coefficients generally have low thermal conductivity, but their electrical conductivity are too low. The properties of semiconductors lie between conductors and insulators and make for the best thermoelectric materials.

By the end of 1950' s, the best thermoelectric materials were found to be alloys of bismuth telluride and antimony telluride and the ZT value was about unity. A ZT value of 4 would make thermoelectric refrigerators economically competitive with conventional compressor-based refrigerators [9]. Over the past 40 years, the ZT value has improved very little. In the 1990' s, the rapid development of semiconductor industrial makes the searching for thermoelectric materials with high ZT values hopeful.

It is clear that high Seebeck coefficient, high electrical conductivity and low thermal conductivity maximize the ZT value. There are several methods to increase the ZT value. One approach is the use of low-dimensional nanostructures like superlattices, nanowires and quantum dots [10, 11]. Superlattices are periodic structures consisted of hundreds of layers of thin films [12]. Due to the confinement of phonon in superlattices, the thermal conductivity will be reduced and then increases the ZT value [13].

1.2 Nano Technology in Energy and Heat Transfer

Nano technology has become a very hot topic in recent years. Nano machines and nano materials are very important issues in the area of nano technology. As the advancement in fabrication, the device size is shrinking into micro/nano meter and it is possible to produce a nano machine. A nanoscale submarine might be useful in medicine by navigating through the blood, seeking out cancer cells and destroying

them [14]. Besides developing a novel nanomachine, a material with desired physical characteristics is also helpful to improve the performance of the current machines or devices. The past nano science researches told us that the physical properties of materials are different from their bulk values when the size of a device is reduced to nanometer scale. Thus, new structures with novel physical properties can be designed with known materials. There are many potential engineering applications associated with nano technology in energy and heat transfer such as thermoelectric superlattices, carbon nanotubes, electrokinetic microchannel battery, nanofluids and solar cells. The brief introductions of carbon nanotubes, electrokinetic microchannel battery, nanofluids and solar cells are presented as below.

Carbon Nanotubes

Carbon nanotubes, as shown in Fig. 1.1, have attracted many researchers' attention due to their widely possible applications. They are constructed by rolling up an infinite stripe of graphite sheet and can be described as graphite cylinders. The extraordinary high and reversible hydrogen absorption in single walled carbon nanotubes make it possible that using them as high capacity hydrogen storage media, which is important for fuel cells [15]. Besides, single walled carbon nanotubes are used as battery electrodes owing to their large irreversible capacities and voltage hysteresis [16].

Electrokinetic Microchannel Battery

Yang et al. [17] developed an electrokinetic battery consisting of an array of microchannels to convert the hydrostatic pressure of a liquid into electrical work. Electrically neutral liquids perform a charge distribution near the solid-liquid interface,

as illustrated in Fig. 1.2, owing to a charged solid surface and this region is known as electrical double layer. Due to the presence of an electrical double layer pressure-driven flow in a microchannel will induce a streaming current.

Nanofluids

Solid particle suspensions with high thermal conductivity have the potential to enhance the heat transfer in liquids. Nanofluid, as illustrated in Fig. 1.3, is a new kind of heat transfer medium containing uniformly and stably distributed nanoparticles [18]. Recent measurements showed that the thermal conductivity of nanofluids increases as the particle size decreases. To explain this phenomenon, Keblinski et al. [19] proposed four possible mechanisms: (1) Brownian motion of the particles, (2) molecular-level layering of the liquid at the liquid/particle interface, (3) ballistic heat transfer in the nanoparticles, and (4) the effects of nanoparticle clustering. However, these mechanisms are insufficient in explaining the dramatic increasing thermal conductivity of nanofluids. There is a need to explore other heat transfer mechanisms to complete the heat transfer enhancement theory of nanofluids.

Solar Cells

The polymer-based devices are mostly attractive due to their easy production technology and lower costs [20]. However, the efficiencies of polymer solar cells are much lower than those of conventional solar cells. Solar cells assembled from blending inorganic nanorods with polymers have the potential to enhance the efficiency of solar power conversion [21]. Controlling inorganic materials on the nanoscale opens new opportunities for the development of novel solar cells because of the nanoscale nature of light absorption and photocurrent generation in solar energy

conversion [22]. Since inorganic nanorods naturally provide a directed path for electrical transport, they are preferable in solar energy conversion. By altering the radius of CdSe nanorods, as shown in Fig. 1.4, the quantum size effect can be used to control the band gap. Moreover, quantum confinement enhances the absorption coefficient and thus the devices can be made more compact.

1.3 Microscale Heat Transfer Models

1.3.1 Molecular Dynamics Simulation

Utilizing a true representation of the intermolecular potential in molecular dynamics simulations is critical for ensuring that the physics underlying microscale heat transfer phenomena is accurate [23]. However, it is difficult to obtain a precise potential function. One of the well established intermolecular potential functions is the Lennard-Jones (LJ) potential. The LJ 12-6 potential is

$$f_{LJ}(r_{ij}) = 4e_{LJ}\left[\left(\frac{s_{LJ}}{r_{ij}}\right)^{12} - \left(\frac{s_{LJ}}{r_{ij}}\right)^{6}\right], \tag{1-2}$$

where r_{ij} is the distance between atoms i and j, e is the well depth of the potential and s_{LJ} is the equilibrium separation parameter. The Lennard-Jones potential is a two-body potential and it is valid for inert gases. Another frequently mentioned two-body potential called Morse potential is adequate for metals. The two-body potential functions are the simplest potential functions since only the interactions between two atoms are considered. Thus, many-body potential functions, such as tight-binding potential, Stillinger-Weber potential and the embedded-atom method, are developed to describe the interactions among atoms more precisely.

The first derivative of Eq. (1-2) is the force experienced by an atom due to the presence of another atom. Using Newton's second law of motion, a relation between

force and acceleration can be established as

$$m\frac{d^2 r_i}{dt^2} = \sum_{j\neq 1} \vec{F}(r_{ij}), \tag{1-3}$$

where m represents the atom mass and F is the force. Substituting the first derivative of Eq. (1-2) into Eq. (1-3), a relation between the interatomic potential and the vibrational motion of the atoms in the system will be established.

1.3.2 Thermal Wave Model

The original thought of the thermal wave theory is that the speed of heat propagation cannot be infinity. Thus, there must be a time lag between heat flux and temperature gradient [24]. Cattaneo [25] and Vernotte [26] proposed a modified model as following:

$$\vec{q}(\vec{r},t) + t_R \frac{\partial \vec{q}(\vec{r},t)}{\partial t} = -k\nabla T, \tag{1-4}$$

where q is the heat flux, t_R is the relaxation time, k is the thermal conductivity and T is the temperature. Substitution the above equation into the energy conservation equation, then an alternative heat transfer model which is known as thermal wave model or hyperbolic heat conduction equation was developed. The hyperbolic heat conduction equation can be expressed as

$$\frac{t_R}{a}\frac{\partial^2 T}{\partial t^2} + \frac{1}{a}\frac{\partial T}{\partial t} = \nabla^2 T, \tag{1-5}$$

where a is the thermal diffusion coefficient.

1.3.3 Phonon-Electron Interaction Model

Heat transfer in metals are attributed to electron and phonon transport. Since the heat capacity of electron is much smaller than that of phonon, the heating of electron

and phonon can be described as a two-step process [27-29].

$$C_e \frac{\partial T_e}{\partial t} = \nabla \cdot (k_e \nabla T_e) - G(T_e - T_p), \text{ heating of electron,} \tag{1-6a}$$

$$C_p \frac{\partial T_p}{\partial t} = G(T_e - T_p), \text{ heating of phonon,} \tag{1-6b}$$

where C is the heat capacity, k is the thermal conductivity, and the subscript indices e and p denoting for electron and phonon, respectively. The energy exchange between electrons and phonons is characterized by the coupling factor G.

1.3.4 Phonon Scattering Model

The phonon scattering model was developed by solving the linearized Boltzmann transport equation for the pure phonon field [30]. Only heat transport by phonon scattering was emphasized and the contribution of electron in conducting heat was neglected.

$$C_p \frac{\partial T}{\partial t} + \nabla \cdot \vec{q} = 0, \tag{1-7}$$

$$\frac{\partial \vec{q}}{\partial t} + \frac{v^2 C_p}{3} \nabla T + \frac{1}{t_R} \vec{q} = \frac{t_N v^2}{5} \left[\nabla^2 \vec{q} + 2\nabla(\nabla \cdot \vec{q}) \right], \tag{1-8}$$

where C_p is the heat capacity, v is the phonon velocity, t_R is the relaxation time, and t_N is the relaxation time of elastically scattering.

1.3.5 Phonon Radiative Transfer Model

The phonon radiative heat transfer model starts from the solution of the linearized Boltzmann transport equation. The collision term in the Boltzmann transport equation is very complicated and make the Boltzmann equation difficult to solve. By using the relaxation-time approximation, the linearized Boltzmann equation

becomes

$$\frac{\partial f}{\partial t} + v\frac{\partial f}{\partial x} = \frac{f^0 - f}{t_R}. \tag{1-9}$$

Where f^0 is the equilibrium phonon distribution, which follows the Bose-Einstein distribution. Majumdar transformed the Boltzmann equation to an equation of phonon radiative transfer (EPRT) in the form [31]

$$\frac{1}{v}\frac{\partial I}{\partial t} + m\frac{\partial I}{\partial x} = \frac{1}{vt_R}\left(\frac{1}{2}\int_{-1}^{1} I dm - I\right), \tag{1-10}$$

where I is the phonon intensity, and m is the direction cosine. This equation has the same form as the equation of radiative transfer. Therefore, Majumdar called it the equation of phonon radiative transfer.

1.4 Interface Thermal Resistance Models

1.4.1 Interfacial Layer Model

The interfacial layer model assumes an interfacial layer with variable thickness and thermal conductivity in between two dissimilar materials. Two very important parameters directly and significantly affecting heat transport across the two dissimilar materials are the thermal and thickness ratios of the interfacial layer to the reference material. For example, according to the experimental results of Marshall et al. [32] the thermal conductivity and thickness ratios of the interfacial layer to YBa-Cu-O thin film are 0.01 and 0.02, respectively. However, these parameters are strongly depending on the contact conditions such as contact areas and contact pressure. Thus, it is difficult to estimate the thermal and thickness ratios of the interfacial layer to the reference material.

1.4.2 Acoustic Mismatch Model

The acoustic mismatch model starts by assuming that phonons are the major carriers of heat. The interface thermal resistance is attributed to the transmitting and reflecting of phonons at the interface. The interface is perfect and structureless so there is no scattering occurring at the interface. The phonon transmission probability from medium 1 to medium 2 is governed by the Fresnel equations and can be expressed as [33]

$$a_{12} = \frac{4 r_1 v_1 r_2 v_2}{(r_1 v_1 + r_2 v_2)^2}, \tag{1-11}$$

where r is the density and v is the sound velocity. Before proceeding the AMM, the range of validity of assumptions should be checked. At very low temperatures, the phonon wavelength is much smaller than the interfacial roughness and the size of defect near the boundary. The interface may appear to be a perfectly flat plane, which is the basic assumption in the acoustic mismatch model. Thus, the AMM works well at low temperatures. For example, Herth and Weis [34] measured the interface resistance between gold film and sapphire substrate at 100K and confirmed that the AMM predictions matched the experimental results.

1.4.3 Diffuse Mismatch Model

For most interfaces above a few Kelvin, the interface itself is a very strong scatterer of phonons. The analog to the Fresnel equations is no longer valid. Instead, Swartz and Pohl [35] assumed that all the phonons are diffusely scattered at the interface and derived the phonon transmissivity from medium 1 to medium 2 as

$$a_{12} = \frac{\sum_m v_{m2}^{-2}}{\sum_m v_{m1}^{-2} + \sum_m v_{m2}^{-2}}, \tag{1-12}$$

where v_m is the sound velocity of mode m (longitudinal or transverse).

The acoustic mismatch model is valid for smooth interfaces and the diffuse mismatch model is adequate for rough interfaces. The ratio of phonon wavelength to the interface roughness determines the applicability of AMM and DMM. When the phonon wavelength is far small than the interface roughness, the interface can be seen as a rough interface and the diffuse mismatch model is applicable. Otherwise, the acoustic mismatch model is more suitable for a smooth interface which roughness is small compared to the phonon wavelength.

1.4.4 Scattering-Mediated Acoustic Mismatch Model

Scattering-mediated acoustic mismatch model (SMAMM) was developed by observing the close analog between radiative and phonon heat transport [36]. Scattering near the interface is dominant than any other mechanism [35]. At high temperatures, the phonon mean free path is short, so that the phonon wave will attenuate rapidly. In contrast, scattering has hardly any effect on the transmission and reflection of acoustic waves at very low temperatures. The reflectivity from medium 1 to medium 2 predicting by SMAMM can be expressed as

$$R_{12}(q_1)=\frac{\left[\frac{\cos(q_1)}{r_1 v_1}a_1'-\frac{A}{r_2}\right]^2+\left[\frac{\cos(q_1)}{r_1 v_1}b_1'+\frac{B}{r_2}\right]^2}{\left[\frac{\cos(q_1)}{r_1 v_1}a_1'+\frac{A}{r_2}\right]^2+\left[\frac{\cos(q_1)}{r_1 v_1}b_1'-\frac{B}{r_2}\right]^2}, \tag{1-13}$$

and the transmissivity is

$$a_{12}(q_1)=1-R_{12}(q_1), \tag{1-14}$$

where

$$a'=\sqrt{1+\left(\frac{1}{2tw}\right)^2}, \tag{1-15a}$$

$$b' = \frac{1}{2tw}, \tag{1-15b}$$

$$A = \left\{ \frac{1}{2}\left[\left(\frac{a_2'^2 - b_2'^2}{v_2^2} - \frac{a_1'^2 - b_1'^2}{v_1^2}\sin^2(q_1) \right)^2 + 4\left(\frac{a_1' b_1'}{v_1^2}\sin^2(q_1) - \frac{a_2' b_2'}{v_2^2} \right)^2 \right]^{1/2} + \frac{1}{2}\left(\frac{a_2'^2 - b_2'^2}{v_2^2} - \frac{a_1'^2 - b_1'^2}{v_1^2}\sin^2(q_1) \right) \right\}^{1/2}, \tag{1-15c}$$

$$B = \left\{ \frac{1}{2}\left[\left(\frac{a_2'^2 - b_2'^2}{v_2^2} - \frac{a_1'^2 - b_1'^2}{v_1^2}\sin^2(q_1) \right)^2 + 4\left(\frac{a_1' b_1'}{v_1^2}\sin^2(q_1) - \frac{a_2' b_2'}{v_2^2} \right)^2 \right]^{1/2} - \frac{1}{2}\left(\frac{a_2'^2 - b_2'^2}{v_2^2} - \frac{a_1'^2 - b_1'^2}{v_1^2}\sin^2(q_1) \right) \right\}^{1/2}. \tag{1-15d}$$

SMAMM accurately describes the behavior of interface thermal resistance at high temperatures and it can reduce to AMM at low temperatures.

1.5 Literature Survey

1.5.1 Microscale Heat Transfer

As mentioned before, Fourier law, a macroscale model, is inadequate to deal with microscale heat transfer problems. Thus, it is important to develop microscale heat transfer model. Preliminary to develop microscale heat transfer models, the thermophysical characteristics of heat carriers must be clarified. An understanding of heat carriers is the first step toward solving microscale heat transfer problems. The major heat carriers for heat transfer in solids are free electrons, phonons, and photons. Tien and Chen [3] listed important features of heat carriers and the motion of which governs heat transport, as illustrated in Table 1.1. After knowing the general features of heat carriers, one question is raised-which heat transport model is adequate under a given time- and length scales. Flik et al. [37] developed regime maps showing the

boundary between the macroscale and microscale transfer regimes. Further, Majumdar [38] listed the characteristic time- and length scales and corresponding transport phenomena of energy carriers, as shown in Table 1.2. Wave transport and microscopic particle transport are suitable for describing microscale heat transfer in solids. The wave and particle nature of phonons can be obtained from classical text by Kittel [39]. Recently, Chen [40] studied the phonon wave effects on heat conduction in thin films. The results had demonstrated that it is safe to treat the phonon transport based on the phonon particle picture for thin films of practical thickness. The Boltzmann Transport Equation (BTE) is the most suitable model for describing phonon transport in solids due to its ability to correctly describe both equilibrium and non-equilibrium phenomena [41]. To solve the Boltzmann transport equation, several approximation methods had been proposed by numerous researchers [42]. According to BTE, Majumdar [31] developed an equation of phonon radiative transfer (EPRT) to deal with microscale heat conduction in dielectric thin films. Later, Joshi and Majumdar [43] employed the EPRT to study heat transfer across diamond thin films for both steady-state and transient cases. In their studies, the results demonstrated that the geometric size has a great influence on the thermal properties of materials, which is so-called size effect.

1.5.2 Interface Thermal Resistance

The interface thermal resistance also plays an important role in determining heat flow in thin-film/substrate systems. The existence of interface thermal resistance prevents the heat from propagating and may cause device failure. Many experiments [44-48] have been conducted to determine the interface thermal resistance between thin films and substrates. Besides the experimental quantification of interface thermal

resistance, theoretical analysis also has been done by many researchers. Little [49] predicted interface thermal resistance by treating phonons as plane waves and proposed the acoustic mismatch model (AMM). An essential assumption of the AMM is that no scattering occurs at the interface. Swartz and Pohl [35] considered the diffuse scattering occurring at the interface and proposed the diffuse mismatch model (DMM). Phelan [50] pointed out that the applicability of AMM and DMM is determined by the ratio, $l_d/\bar{s}$, where l_d is the dominant phonon wavelength, and $\bar{s}$ is the mean interfacial roughness. When $l_d/\bar{s} >> 1$, the AMM is applicable, otherwise, the DMM applies. Chen [51] examined the effect of interface conditions on the thermal conductivity of superlattices in the direction parallel to the film plane. He divided the interface conditions into diffuse scattering and specular scattering. It was concluded that diffuse interface scattering, rather than specular scattering, is the cause of the observed reduction in thermal conductivity of superlattices. Later, Chen [52] investigated the interface effect on the thermal conductivity of superlattices in the cross-plane direction. The results based on DMM were in reasonable agreement with experimental results by Capinski and Maris on a GaAs/AlAs superlattices [53]. Zeng and Chen [54] examined the applicability of the thermal boundary resistance to the case with internal heat generation. Prasher and Phelan [36] developed a model, called the scattering-mediated acoustic mismatch model (SMAMM), to exploit the analogy between phonon and radiative transport by developing a damped wave equation to describe the phonon transport. More recently, Chantrenne and Raynaud [55] developed the simulations of heat transfer through an interface by molecular dynamics.

1.5.3 Thermoelectrics

In 1821, Seebeck discovered that when two different conductors were joined together and one of the junctions was heated, a voltage appeared. Later, Peltier discovered the reverse phenomenon that a temperature gradient appeared when an electric current passed through the junction between two conductors [56]. The discovery of thermoelectric materials offers the conversion between heat and electricity [57]. A typical thermoelectric power generator, as illustrated in Fig. 1.5, is based on the Seebeck effect. Both electrons in n-type semiconductors and holes in p-type semiconductors transport from the hot side toward the cold side due to thermal diffusion. Thus, a closed loop is formed and the current flows through an external load to do useful work [58]. Thermoelectric coolers, as shown in Fig. 1.6, is based on Peltier effect and work in reverse to thermoelectric power generators. A current flows through all the elements in series such that both electrons in n-type semiconductors and holes in p-type semiconductors leave the cold side to the hot side. During the transport process, electrons and holes carry thermal energy from the cold side to the hot side and served as heat pumps. In general, practical thermoelectric coolers are consisted of a number of n- and p-type thermoelements [59], as illustrated in Fig. 1.7. The current flows in series through all the semiconductor thermoelements and energy flows in parallel from the cold side to the hot side.

The most important issue in thermoelectrics is to increase the figure of merit, ZT. High electrical conductivity, high Seebeck coefficient and low thermal conductivity are desired to improve the performance of thermoelectric devices. Slack [60] introduced a concept of "phonon-glass electron-crystal" (PGEC) to describe the best thermoelectric materials. PGEC means that the thermoelectric materials should possess a low thermal conductivity as in glass and a high electrical conductivity as in

crystal. For bulk materials, the use of "phonon rattlers" [61] will reduce the phonon thermal conductivity. Phonon rattlers are interstitial atoms inserted into the empty space in the host material. These atoms are weakly bound by the host material [62]. Their vibrations are not consistent with atoms in the host material and thus scatter the phonon in the original lattice. As a result of phonon scattering, the lattice thermal conductivity will decrease. Another approach to reduce thermal conductivity of thermoelectric materials is to develop low-dimensional thermoelectric materials, such as nanodots (0D), nanowires (1D) and thin films (2D) [63, 64]. Low dimensionality provides several advantages: (1) one way for enhancing the density of states near the Fermi energy, resulting in an increasing Seebeck coefficient; (2) opportunities to take advantage of the anisotropic Fermi surfaces in multi-valley cubic semiconductors; and (3) opportunities to increase boundary scattering of phonons at the barrier-well interfaces, without an large increase in electron scattering at the interface [65]. An increase in boundary scattering of phonons reduces the lattice thermal conductivity of materials. Size and interface effects are utilized to develop novel thermoelectric materials. Thin film superlattices and nanowire superlattices are very popular in designing high performance thermoelectric devices.

Since many applications require materials in large quantities, it is desired to develop a bulk material with high ZT value. The highest ZT in a bulk thermoelectric material at $300\,K$ is 1.14 for p-type $(Bi_2Te_3)_{0.25}(Sb_2Te_3)_{0.72}(Sb_2Se_3)_{0.03}$ alloy [66]. Polvani et al. [67] reported a $ZT > 2$ at $300\,K$ in $Bi_{0.5}Sb_{1.5}Te_3$ alloy. However, the hydrostatic pressure is as high as $2\,GPa$. It is not adequate for practical engineering applications. Recently, Hsu et al. [68] discovered that the ZT of $Ag_{1-x}Pb_mSbTe_{2+m}$ reached a value of 2.2 at $800\,K$. The $Ag_nPb_mSb_nTe_{m+2n}$ materials may find potential applications in thermoelectric power generation. Like the

enhancement of ZT in bulk materials, the thermoelectric figure of merit of low-dimensional materials gets great improvement in recent years. Venkatasubramanian et al. [69] reported a maximum ZT of 2.4 for the p-type Bi_2Te_3/Sb_2Te_3 thin-film superlattices devices. Up to date, it is the highest value observed by researchers.

1.5.4 Thermal Conductivity Measurements in Micro/Nano Structures

Many studies on the thermal conductivity of thin films have been carried out [1]. Besides the establishment of theoretical models, measurements of thermophysical properties are also very important. Thermal conductivity characterization of micro/nano structures is challenging since it is difficult to establish and to measure the temperature difference over a small distance [63]. Some researchers developed several measurement methods to quantify the thermal conductivity of materials. Yao [70] measured the thermal properties of GaAs/AlAs superlattice. Yu et al. [71] reported the temperature dependence of thermophysical properties of GaAs/AlAs superlattices. Both Yu and Yao et al. measured the thermal conductivity of superlattices in the in-plane direction. By contrast, a popular method developed by Cahill [72] for measuring the thermal conductivity of thin films in the cross-plane direction is the 3ω method. Lee and Cahill [73] measured the thermal conductivity of Si/Ge superlattices. Capinski and Maris [53] presented measurements of the thermal conductivity of GaAs/AlAs superlattices. Venkatasubramanian et al. [69] measured the thermal conductivity of Bi_2Te_3/Sb_2Te_3 thin-film superlattices. Huxtable et al. [74] measured the thermal conductivity of Si/SiGe and SiGe/SiGe superlattices over a temperature range of 50 to 320 K. Additionally, Yang et al. [75] developed a method based on the 3ω method to simultaneously measure the Seebeck coefficient and thermal

conductivity of an n-type Si/Ge quantum-dot superlattice in the cross-plane direction.

In the 3ω method, a metal line that was used as a heater/thermometer was deposited onto the sample, as illustrated in Fig. 1.8. Since thermoelectric thin films are electrically conducting, there is a need to deposit an electrically insulating layer to isolate the thermoelectric film from the heater. An ac current with angular frequency w is applied to the heater and then generates a $2w$ temperature variation inside the sample. Since the variation of electrical resistance of a metal is proportional to its temperature variation, the electrical resistance of the metal line oscillates at $2w$. Multiplying the current and the electrical resistance together, and the product is the voltage drop across the heater. Thus, the voltage contains a $3w$ signal that depends on the temperature rise. Measuring the voltage change and the temperature rise and then substituting them into the equation derived by Lee and Cahill [76] will get the thermal conductivity of thin films.

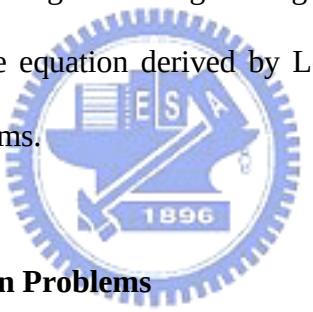

1.5.5 Inverse Heat Conduction Problems

Over the past three decades, a considerable amount of work has been done on the study of inverse heat transfer problems by either analytical methods or numerical methods. The analytical methods include exact methods, polynomial methods, and integral methods [77]. These methods are only useful for solving linear one-dimensional problems with particular initial and boundary conditions. Numerical methods, on the other hand, have the advantage of being applicable to any problem type.

In general, inverse heat transfer problems are classified into 5 groups [77-79]: (1) inverse boundary problem; (2) inverse initial problems; (3) inverse geometry problems; (4) parameter estimation; (5) other problems. The intrinsic characteristic of

inverse problems is that they are ill-posed [78]. By contrast, a well-posed problem meets the following three requirements: existence, uniqueness and stability. It has been proved that solutions to inverse heat conduction problems usually exist and are unique. However, the obtained estimates are not always numerically stable [77-80]. In other words, small inaccuracies in the measured interior temperatures may cause large oscillations in the calculated surface conditions. Thus, many special methods have been proposed to solve inverse heat conduction problems (IHCPs) [81-84]. The main purpose of these inverse methods is to improve the stability of numerical calculation results.

1.6 Objectives

This study primarily deals with microscale heat transfer in solids. First, it discusses transient heat transfer phenomena in solid dielectric thin films from both macroscopic and microscopic points of view. Phonon radiative transfer model as well as Fourier law and thermal wave theory are utilized to analyze the transient heat conduction phenomena in dielectric thin films. Diamond and GaAs thin films are chosen as the examples to demonstrate the differences between the macroscale and microscale heat transfer models.

Second, we examine microscale heat transfer in multilayer structures. The size and interface effects on the effective thermal conductivity will be checked. Furthermore, curvature effects on the effective thermal conductivity for a two-layer concentric micro tube will also be examined. EPRT is employed to analyze the transient heat transport in the micro tube along radial direction. The DMM is utilized to model the interface condition between layers. Due to the similarity of EPRT and ERT (Equation of Radiative Transfer), the numerical approach based on the Discrete

Ordinate Method [85] is adopted to solve the integro-differential equation. Besides the influences of size and curvature on thermal conductivity, the size and curvature effects on interface thermal resistance are also studied. Furthermore, the numerical predictions are compared to the experimental data to demonstrate the validity of the microscale heat conduction model.

Third, we examine microscale heat transfer in two-dimensional micro tubes. The past literature contains many theoretical and experimental studies of thermal characteristics of thin films, but very few of them paid attention to the thermal characteristic of micro tubes. There is no existing study, which shows that the size (thickness and height) and the curvature effects will change the effective thermal conductivity for micro tubes. In this study, the EPRT is employed to analyze the transient heat transfer in micro tubes. The influences of size and curvature on the thermal conductivity are examined closely.

By extending the foregoing analysis, we examine size effects on the performance of thermoelectric micro coolers. Superlattice structures are widely used to create high performance thermoelectric device because they can greatly reduce the phonon thermal conductivity of materials without much degrading the power factor ($S^2 s_e$). In this study, microscale heat transfer in thin film, nano wire and nano tube superlattices is simulated and then the effective thermal conductivity is calculated. Understanding the influence of device sizes on the their thermal conductivity gives the designing guides for high performance thermoelectric devices.

After knowing what parameters affecting the effective thermal conductivity and how they influencing, the thermophysical properties of materials can be properly defined. The effective thermal conductivity and the temperature histories in the interior points are used to estimate the surface temperature in thin-film/substrate

systems. In this study, a space-marching technique [84] is adopted to estimate the temperature distributions and unknown boundary conditions from internal measurements. A radiation-boundary-condition model based on the AMM is employed to consider the interface thermal resistance between the thin-film and substrate. The influences of interface thermal resistance, measurement errors, and measurement locations are studied. Furthermore, the results of the estimation for the cases with or without interface thermal resistance are also compared.

Table 1.1 General features of heat carriers [3]

	Free Electron	Phonon	Photon
Generation	valence or excited electrons	lattice vibration	atomic, molecule transition
Propagating Media	in vacuum or media	in media	in vacuum or media
Statistics	Fermion	Boson	Boson
Frequency	0~infinite	Debye cut-off	0~infinite
Dispersion	$E = \hbar^2 q^2 / (2m)$	$E = E(q)$	$n = c/l$
Velocity (m/s)	~10^6	~10^3	~10^8

Table 1.2 Characteristic time- and length scales and corresponding transport phenomena of energy carriers [38]

<table>
<tr><td rowspan="2">Time Scales</td><td colspan="4">Length Scales</td></tr>
<tr><td>Wavelength</td><td>Mean Free Path</td><td>Relaxation Length</td><td>Diffusion Length</td></tr>
<tr><td>Collision Time</td><td></td><td colspan="2">Wave Transport</td><td></td></tr>
<tr><td>Mean Free Time</td><td rowspan="2">Wave Transport</td><td colspan="3" rowspan="2">Microscopic Particle Transport Theory</td></tr>
<tr><td>Relaxation Time</td></tr>
<tr><td>Diffusion Time</td><td></td><td></td><td></td><td>Macroscopic Transport</td></tr>
</table>

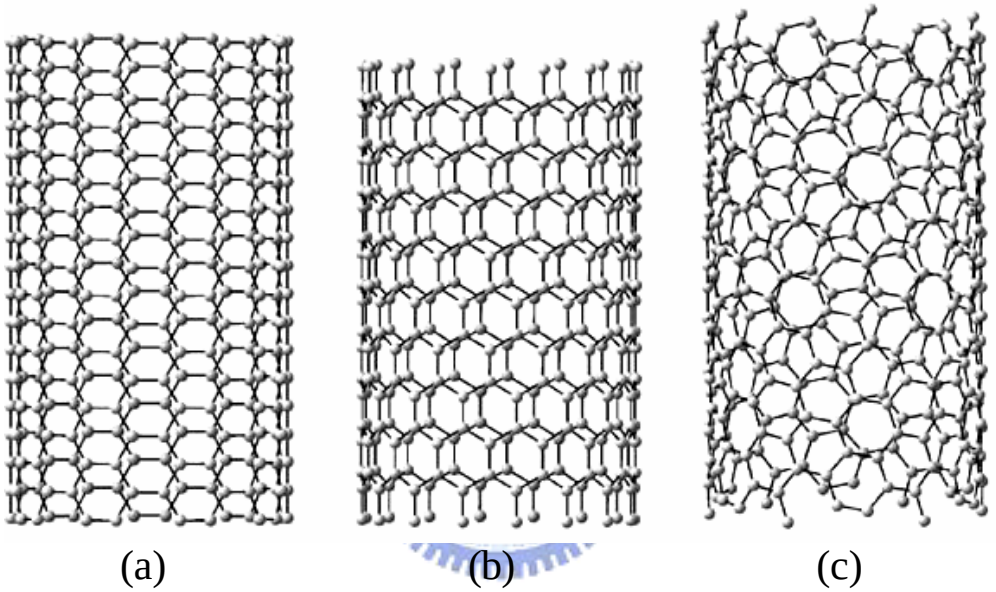

Fig. 1.1 Schematic diagram of single-walled carbon nanotubes: (a) armchair, (b) zigzag, and (c) chiral [86].

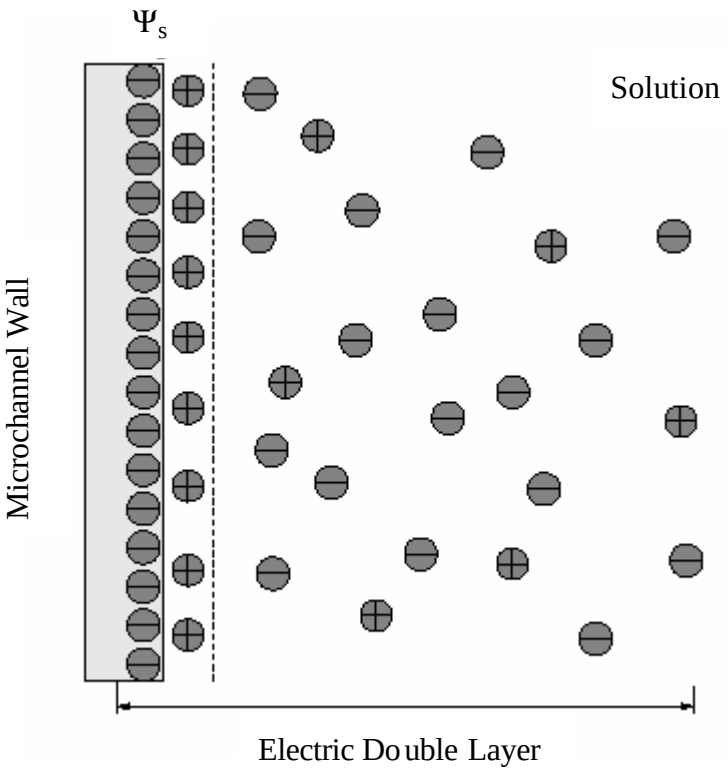

Fig. 1.2 Schematic diagram of electric double layer [17].

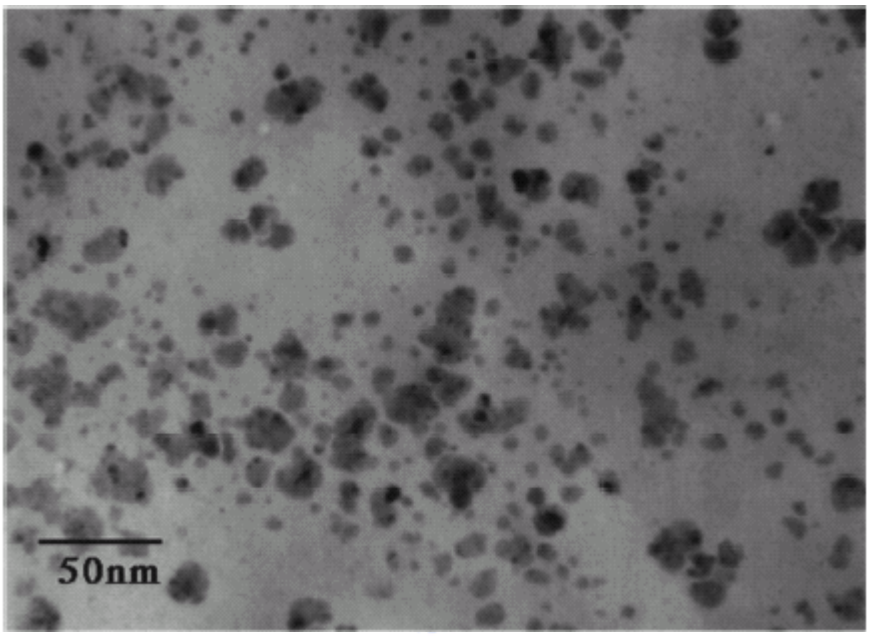

Fig. 1.3 Bright-field transmission electron micrograph of Cu nanoparticles dispersed in ethylene glycol [87].

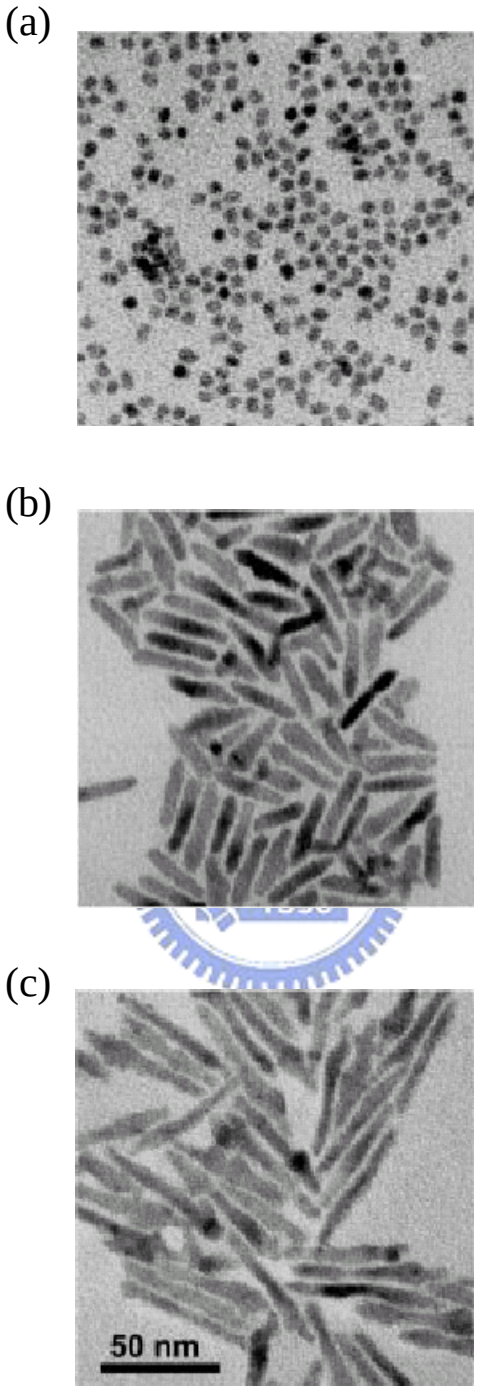

Fig. 1.4 TEM images of CdSe nanorods with various aspect ratios: (a) 7nm by 7nm, (b) 7nm by 30nm, and (c) 7nm by 60nm [22].

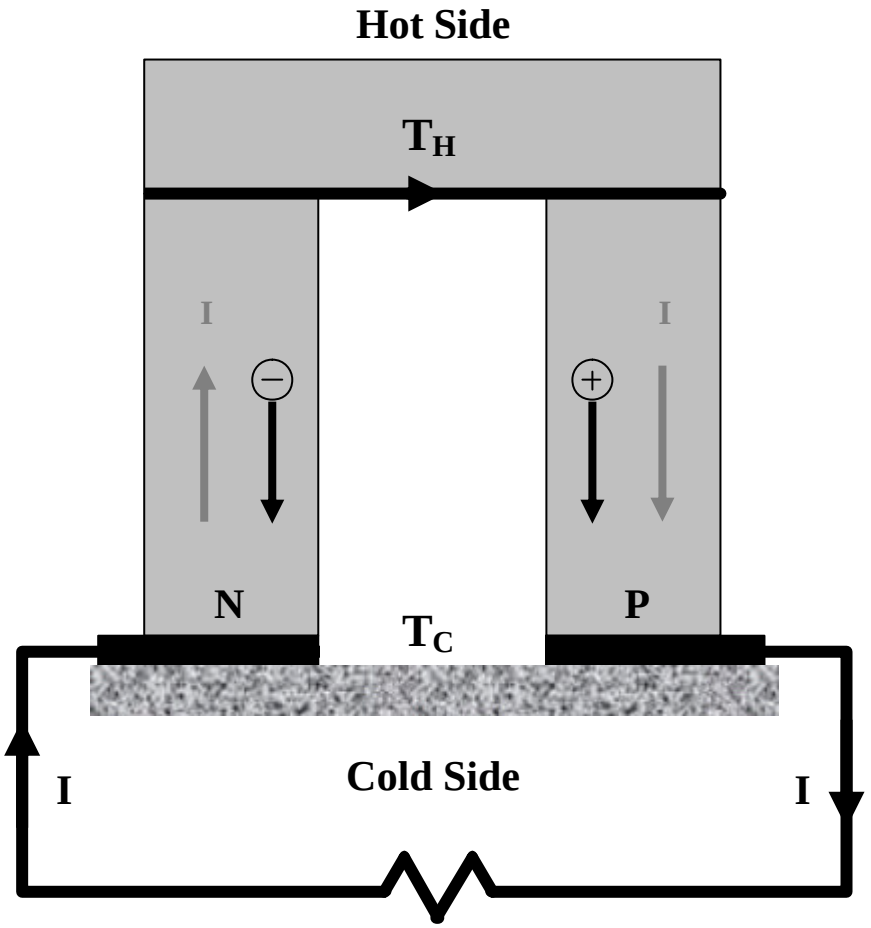

Fig. 1.5 Schematic diagram of a thermoelectric power generator.

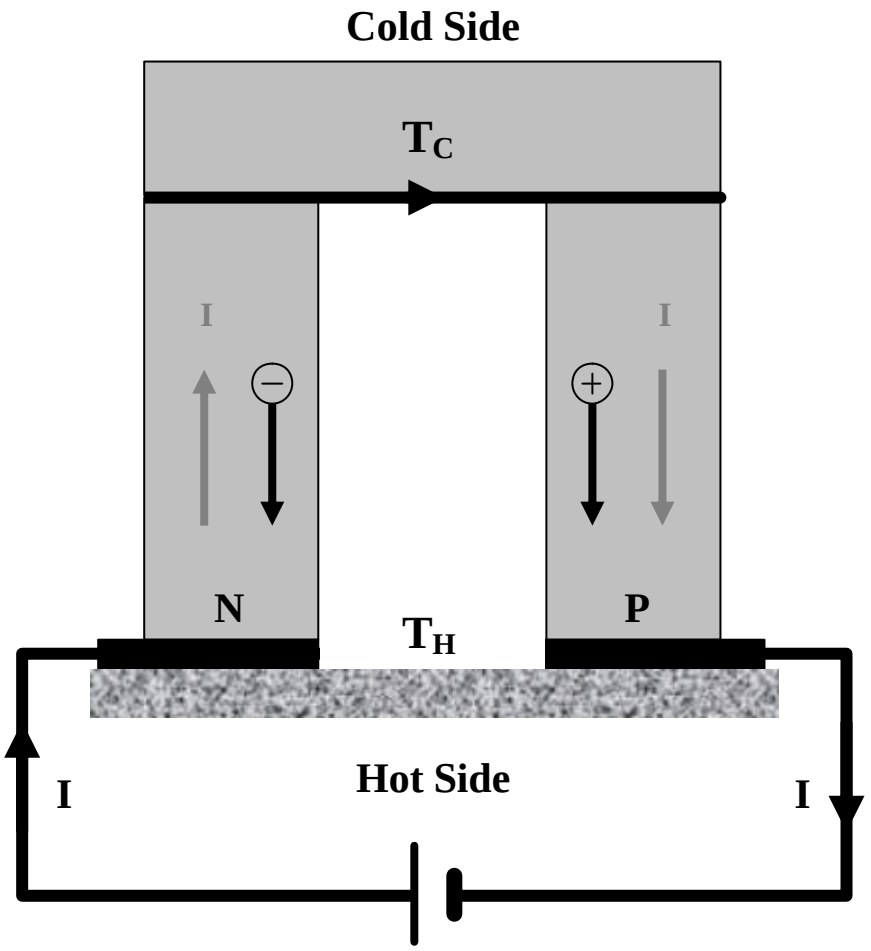

Fig. 1.6 Schematic diagram of a thermoelectric cooler.

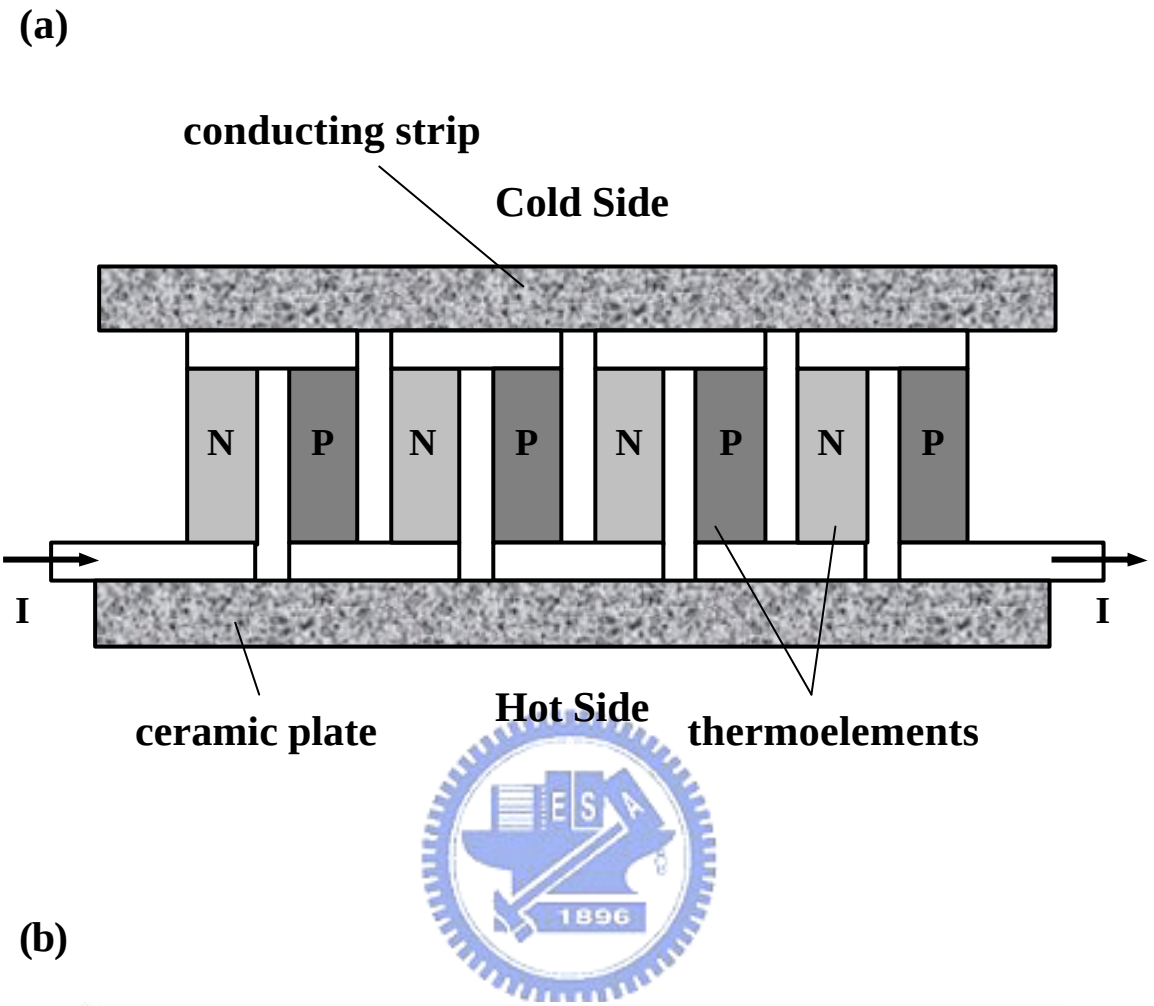

Fig. 1.7 (a) Schematic diagram of a practical thermoelectric cooler [7]. (b) Actual device [88].

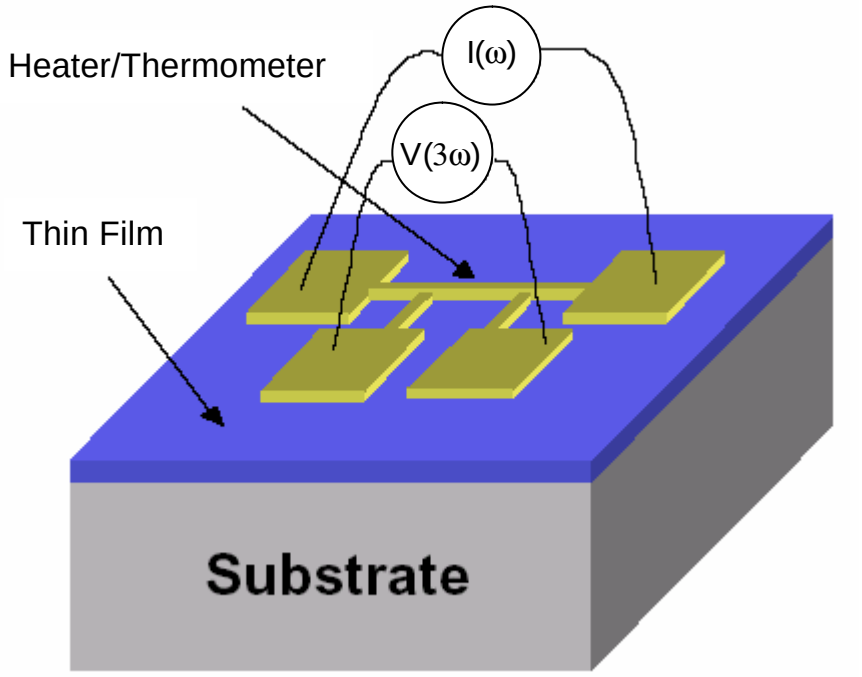

Fig. 1.8 Schematic diagram for the 3ω method to measure the thermal conductivity of thin films [89].

2. MICROSCALE HEAT TRANSFER IN SOLID THIN FILMS

Microscale heat transfer in solid thin films is attracting many researchers' notice in recent years. To find out the difference between macroscopic and microscopic points of view is of great importance. In this chapter, diamond and GaAs thin films are chosen as the examples to illustrate the discrepancy between the macroscale and microscale heat transfer models. Fourier law, thermal wave theory and phonon radiative transfer model are utilized to analyze the transient heat conduction phenomena in solid thin films. Comparison of the temperature distributions predicted by Fourier law and EPRT has been done to seek the boundary between macroscale and microscale transfer regimes.

2.1 Analysis

2.1.1 Mathematical Formulation

Consider a dielectric thin film of thickness L with temperature T_0 initially. At time $t = 0$, the temperature at $x = 0$ is risen to T_r. Meanwhile, the temperature at $x = L$ is still maintained at T_0. The schematic diagram is shown in Fig. 2.1. Phonon radiative transfer model as well as Fourier law and thermal wave theory are utilized to analyze heat conduction in the dielectric thin film. The dimensionless variables are defined as follows:

$$q_a = \frac{T - T_0}{T_r - T_0},\ x_a = \frac{x}{L},\ t_a = \frac{t}{(L/v)},\ Q_a = \frac{q}{s_s(T_r^4 - T_0^4)}, \tag{2-1}$$

where v is the speed of sound.

Fourier Law

The governing equation of the above problem according to Fourier law is

$$\frac{\partial q_a}{\partial t_a} = \frac{a}{vL}\frac{\partial^2 q_a}{\partial x_a^2}, \tag{2-2}$$

with initial condition

$$q_a(x_a,0) = 0, \tag{2-3}$$

and boundary conditions

$$q_a(0,t_a) = 1, \tag{2-4a}$$

$$q_a(1,t_a) = 0. \tag{2-4b}$$

Thermal Wave Theory

The equation of thermal wave theory can be written as

$$\frac{t_R v^2}{a}\frac{\partial^2 q_a}{\partial t_a^2} + \frac{Lv}{a}\frac{\partial q_a}{\partial t_a} = \frac{\partial^2 q_a}{\partial x_a^2}, \tag{2-5}$$

with initial conditions

$$q_a(x_a,0) = 0, \tag{2-6a}$$

$$\frac{\partial q_a(x_a,0)}{\partial t_a} = 0, \tag{2-6b}$$

and boundary conditions

$$q_a(0,t_a) = 1, \tag{2-7a}$$

$$q_a(1,t_a) = 0. \tag{2-7b}$$

Phonon Radiative Transfer Model

The semi-classical Boltzmann transport equation for the case of one dimensional heat transport by phonons between two parallel plates is

$$\frac{\partial f}{\partial t}+v\frac{\partial f}{\partial x}=\left(\frac{\partial f}{\partial t}\right)_{coll}. \tag{2-8}$$

Here f is the distribution function of phonons. The collision term, $\left(\frac{\partial f}{\partial t}\right)_{coll}$, is very complicated and makes the Boltzmann equation difficult to be solved. By using the relaxation-time approximation, the Boltzmann equation becomes

$$\frac{\partial f}{\partial t}+v\frac{\partial f}{\partial x}=\frac{f^0-f}{t_R}. \tag{2-9}$$

Where f^0 is the equilibrium phonon distribution, which follows the Bose-Einstein distribution. At 1993, Majumdar transformed the Boltzmann equation to an equation of phonon radiative transfer (EPRT) in the form [31]

$$\frac{1}{v}\frac{\partial I}{\partial t}+m\frac{\partial I}{\partial x}=\frac{I^0-I}{vt_R}, \tag{2-10}$$

where I represents the intensity of phonons and m is the direction cosine. I^0 is the equilibrium intensity which can be transformed by the following relation

$$I^0=\frac{1}{2}\int_{-1}^{1}Idm. \tag{2-11}$$

Replacing I^0 in the EPRT by the integral in Eq. (2-11) obtains

$$\frac{1}{v}\frac{\partial I}{\partial t}+m\frac{\partial I}{\partial x}=\frac{1}{vt_R}\left(\frac{1}{2}\int_{-1}^{1}Idm-I\right). \tag{2-12}$$

Once the intensity of phonons is solved from the above equation, the temperature distribution is obtained from the Bose-Einstein distribution function at an equilibrium state:

$$I^0(T)=\frac{1}{2}\int_{-1}^{1}Idm=\sum_p v_p\frac{\hbar wD(w)}{\exp\left[\frac{\hbar w}{k_BT}\right]}, \tag{2-13}$$

where $\hbar$ is the Planck's constant divided by $2p$, k_B is the Boltzmann constant,

$D(w)$ is the density of states, and subscript p is the polarization index.

2.1.2 Numerical Method

Fourier Law

The governing system is solved using the finite difference technique with implicit algorithm in time and central difference in space. Thus, the difference equation becomes

$$\frac{q_{a,i}^{n+1}-q_{a,i}^{n}}{Dt_a}=\frac{a}{vL}\frac{q_{a,i+1}^{n+1}-2q_{a,i}^{n+1}+q_{a,i-1}^{n+1}}{(Dx_a)^2}, \tag{2-14}$$

where $q_{a,i}^{n}$ represents the dimensionless temperature at $x_a=(i-1)Dx_a$ and $t_a=(n-1)Dt_a$. The computational grid number in the thin film are taken 31 points and the time step (Dt_a) is 10^{-5}. The corresponding grid test has been carried out and is shown in Fig. 2.2.

Thermal Wave Theory

By using the technique of Laplace transform, the solution can be obtained

$$\bar{q}_a=\frac{1}{u}\left[\left(1-\frac{1}{1-e^{2\sqrt{u\left(\frac{Lv}{a}+\frac{t_Rv^2}{a}u\right)}}}\right)e^{-\sqrt{u\left(\frac{Lv}{a}+\frac{t_Rv^2}{a}u\right)}x_a}+\frac{1}{1-e^{2\sqrt{u\left(\frac{Lv}{a}+\frac{t_Rv^2}{a}u\right)}}}e^{\sqrt{u\left(\frac{Lv}{a}+\frac{t_Rv^2}{a}u\right)}x_a}\right], \tag{2-15}$$

where

$$\bar{q}_a(x_a;u)=\int_0^{\infty}q_a(x_a,t)e^{-ut_a}dt_a. \tag{2-16}$$

The temperature is obtained by the Laplace inversion:

$$q_a(x_a,t_a)=\frac{1}{2pi}\int_{g-i\infty}^{g+i\infty}\bar{q}_a(x_a;u)e^{ut_a}du. \tag{2-17}$$

Let $u = g + iV$ and substitute it into the above equation. Eq. (2-17) is reduced to a Fourier transform:

$$q_a(x_a, t_a) = \frac{e^{gt_a}}{2p}\int_{-\infty}^{\infty} \bar{q}_a(x_a, u = g + iV)e^{iVt_a}dV . \tag{2-18}$$

The Fourier integral can be approximated by its Riemann sum. Let $V = np / b$ and $DV_n = p / b$, where b is the half-period, Eq. (2-18) can be expressed as

$$\begin{aligned} q_a(x_a, t_a) &= \frac{e^{gt_a}}{2b}\sum_{n=-\infty}^{\infty} \bar{q}_a(x_a, g + \frac{inp}{b})e^{-int_a p/b} \\ &= \frac{e^{gt_a}}{b}\left[\frac{1}{2}\bar{q}_a(x_a, g) + \mathrm{Re}\sum_{n=1}^{\infty}\bar{q}_a(x_a, g + \frac{inp}{b})e^{int_a p/b}\right]. \end{aligned} \tag{2-19}$$

At $b = t_a$, Eq. (2-19) yields

$$q_a(x_a, t_a) \cong \frac{e^{gt_a}}{t_a}\left[\frac{1}{2}\bar{q}_a(x_a, g) + \mathrm{Re}\sum_{n=1}^{N}\bar{q}_a(x_a, g + \frac{inp}{t_a})(-1)^n\right]. \tag{2-20}$$

The temperature distribution in the thin film can be obtained by using the above equation.

Phonon Radiative Transfer Model

Eq. (2-12) is an integro-differential equation and difficult to obtain the exact solution. Numerical approach is utilized to solve it. It's convenient to separate the intensity I into a forward component $I^+(x, m)$ and a backward component $I^-(x, m)$. Defining the forward and backward radiosities as

$$J^+ = \int_0^1 I^+ dm, \qquad 0 < m < 1, \tag{2-21a}$$

$$J^- = \int_{-1}^0 I^- dm, \qquad -1 < m < 0. \tag{2-21b}$$

Under the Schuster-Schwarzschild approximation, the nondimensional governing equations become [90]

$$\frac{\partial J^+}{\partial t_a}+\frac{1}{2}\frac{\partial J^+}{\partial x_a}+\frac{L}{vt_R}J^+=\frac{L}{2vt_R}(J^++J^-),\qquad 0<m<1, \tag{2-22a}$$

$$\frac{\partial J^-}{\partial t_a}-\frac{1}{2}\frac{\partial J^-}{\partial x_a}+\frac{L}{vt_R}J^-=\frac{L}{2vt_R}(J^++J^-),\quad -1<m<0. \tag{2-22b}$$

The initial condition can be written as

$$I(x_a,0,m)=I(q_a=0). \tag{2-23}$$

And boundary conditions are

$$I(0,t_a,m)=I^0(q_a=1), \tag{2-24a}$$

$$I(1,t_a,m)=I^0(q_a=0). \tag{2-24b}$$

Backward difference is used in space when $0<m<1$ and forward difference is used in space when $-1<m<0$. Thus, the governing equations can be expressed as

$$\frac{J_i^{+,n+1}-J_i^{+,n}}{Dt_a}+\frac{1}{2}\frac{J_i^{+,n}-J_{i-1}^{+,n}}{Dx_a}+\frac{L}{vt_R}J_i^{+,n}=\frac{L}{2vt_R}(J_i^{+,n}+J_i^{-,n}),\ 0<m<1, \tag{2-25a}$$

$$\frac{J_i^{-,n+1}-J_i^{-,n}}{Dt_a}-\frac{1}{2}\frac{J_{i+1}^{-,n}-J_i^{-,n}}{Dx_a}+\frac{L}{vt_R}J_i^{-,n}=\frac{L}{2vt_R}(J_i^{+,n}+J_i^{-,n}),\ -1<m<0, \tag{2-25b}$$

where n and i are the time and space index, respectively. 31 computational grids are used in this study and the dimensionless time step (Dt_a) is 0.01. Grid refinement study, as shown in Fig. 2.3, has been done to ensure that the essential physics are independent of grid size.

2.2 Results and Discussion

In order to dissipate the heat generated in electronic packages, dielectric films with high thermal conductivity are highly desirable. Diamond has excellent conductivity of heat but high electrical thermal resistance, so the diamond thin film is chosen as the demonstrating case in this study.

Fig. 2.4 displays the temperature profiles for the films of thickness $L = 0.1$, 1, and $10L$ at dimensionless time $t_a = 0.5$. Fourier law predicts diffusion behavior and thermal wave theory predicts wavelike behavior. EPRT is essentially a wave equation. It has not only wavelike nature but also diffusive one. The propagation speed of heat predicted by Fourier law is fastest. Because it has no time delay between temperature gradient and heat flux, the speed of heat transfer is infinity. However, the propagation speed of heat predicted by EPRT is v and that is $v/\sqrt{3}$ by thermal wave theory. For examples, at $t_a = 0.5$, the temperature predicted by Fourier law within the thin film isn't zero anywhere, i.e. heat has already reached the other side of the thin film, whose thickness is $0.1L$. At the same time, it reaches $x_a = 0.3$ by thermal wave theory and near $x_a = 0.7$ by EPRT.

Fig. 2.5 shows the temperature profiles for the films of thickness $L = 0.1$, 1, and $10L$ at dimensionless time $t_a = 10$. For such long time, thermal wave model approaches to Fourier law. It has no difference from thermal wave theory and Fourier law in the cases of thickness $L = 1$ and $10L$. However, in the case of thickness $L = 0.1L$, heat predicted by thermal wave theory gets to reflect from the boundaries and then raises the temperature within the film. Meanwhile, the temperature predicted by Fourier law has already reached its steady-state in such small film thickness. EPRT has already reached its steady-state and then shows a linear temperature profile, like Fourier law. The most obvious difference between EPRT and the other two models is that EPRT predicts temperature jump at boundaries. It is similar to the pure radiation heat transfer problem. Thus the phonon transport is partially ballistic, partially wavelike, and partially diffusive. As film is getting thicker, the temperature jump at boundaries is getting smaller. The ratio of film thickness to the phonon mean free path,

L/L, is the most important parameter to determine the heat transfer behavior in thin films. Diffusion effects dominate for the case that L/L is greater than 1, and wavelike and ballistic heat transfer behavior are much more dominant for the case that L/L is less than 1.

Fig. 2.6 shows the heat flux history at $x_a = 0$ for the films of thickness $L = 0.1$, 1, and $10L$. The heat transfer predicted by Fourier law reaches steady-state very soon for the case of $L = 0.1L$, and the heat flux is unchanged after steady-state. For the same case, thermal wave theory predicts a toothed heat flux profile due to reflections from boundaries. EPRT predicts a lower value of heat flux than Fourier law at steady-state for L/L less than 1. Contrarily, EPRT predicts a higher value for L/L greater than 1.

Sound velocity, phonon mean free path, film thickness, and Debye temperature determine the heat transfer phenomena in solids. However, the ratio of film thickness to phonon mean free path is the most important parameter for microscale heat transfer. Fig. 2.7 demonstrates the temperature distributions of diamond and GaAs thin films of the same dimensionless film thickness at the same dimensionless time. It can be found that L/L is the only parameter to determine the temperature distribution.

From the above discussion, the microscale heat transfer model, EPRT, approaches the macroscale heat transfer model, Fourier law, as the film is getting thicker. It is important to find out the criterion whether Fourier law is applicable in a given thin film. It can be seen that EPRT approaches to Fourier law when the film is getting thick. From Fig. 2.8, no observable difference could be detected between EPRT and Fourier law when $L/L = 100$.

Fig. 2.9 displays the steady-state boundary temperature of GaAs and diamond

thin films predicted by Fourier law and EPRT for different L/L. The boundary temperature approaches to 1 as the film is getting thick. On the other hand, it approaches to 0.5 when the film is getting thin. The right hand limit is called the Fourier limit, and the left hand limit is called Casimir limit. The EPRT of GaAs thin film approaches to Fourier law as the film thickness is great than 2 μm, and reduces to Casimir limit when the film thickness is less than 5 nm. In the case of diamond, those limits are 10 μm and 80 nm respectively. This profile offers a simple way to judge which conduction heat transfer model is applicable in a given film thickness.

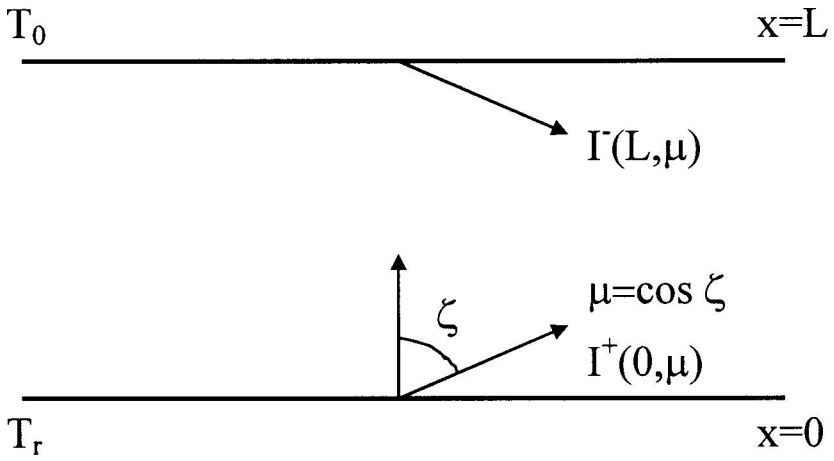

Fig. 2.1 Schematic diagram of a dielectric thin film.

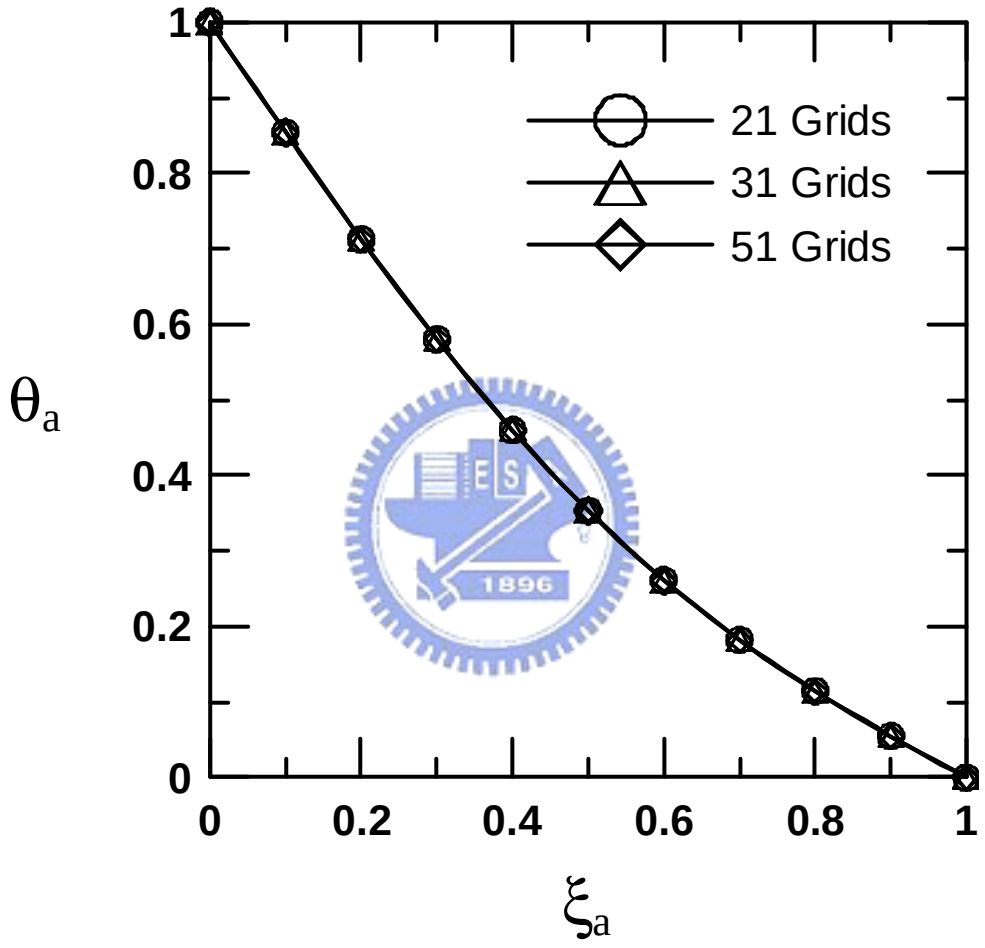

Fig. 2.2 Grid-refinement test for the numerical scheme used to solve Fourier law.

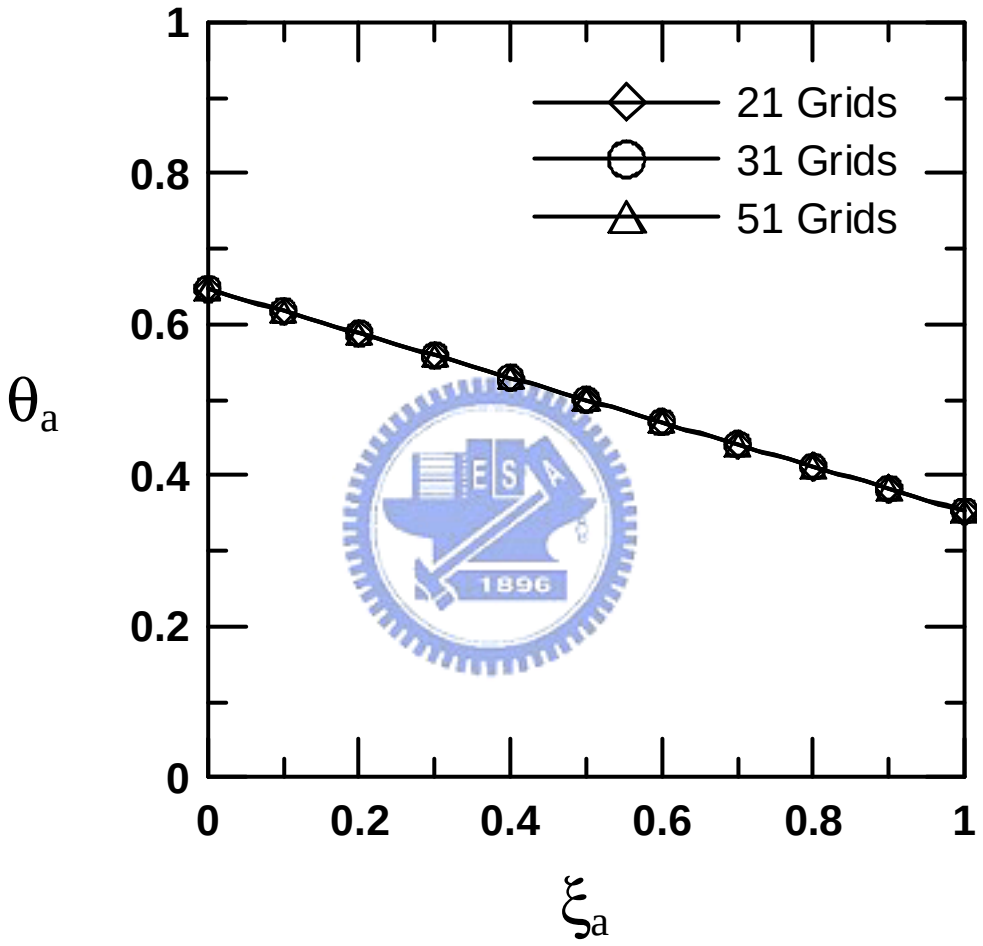

Fig. 2.3 Grid-refinement test for the numerical scheme used to solve EPRT.

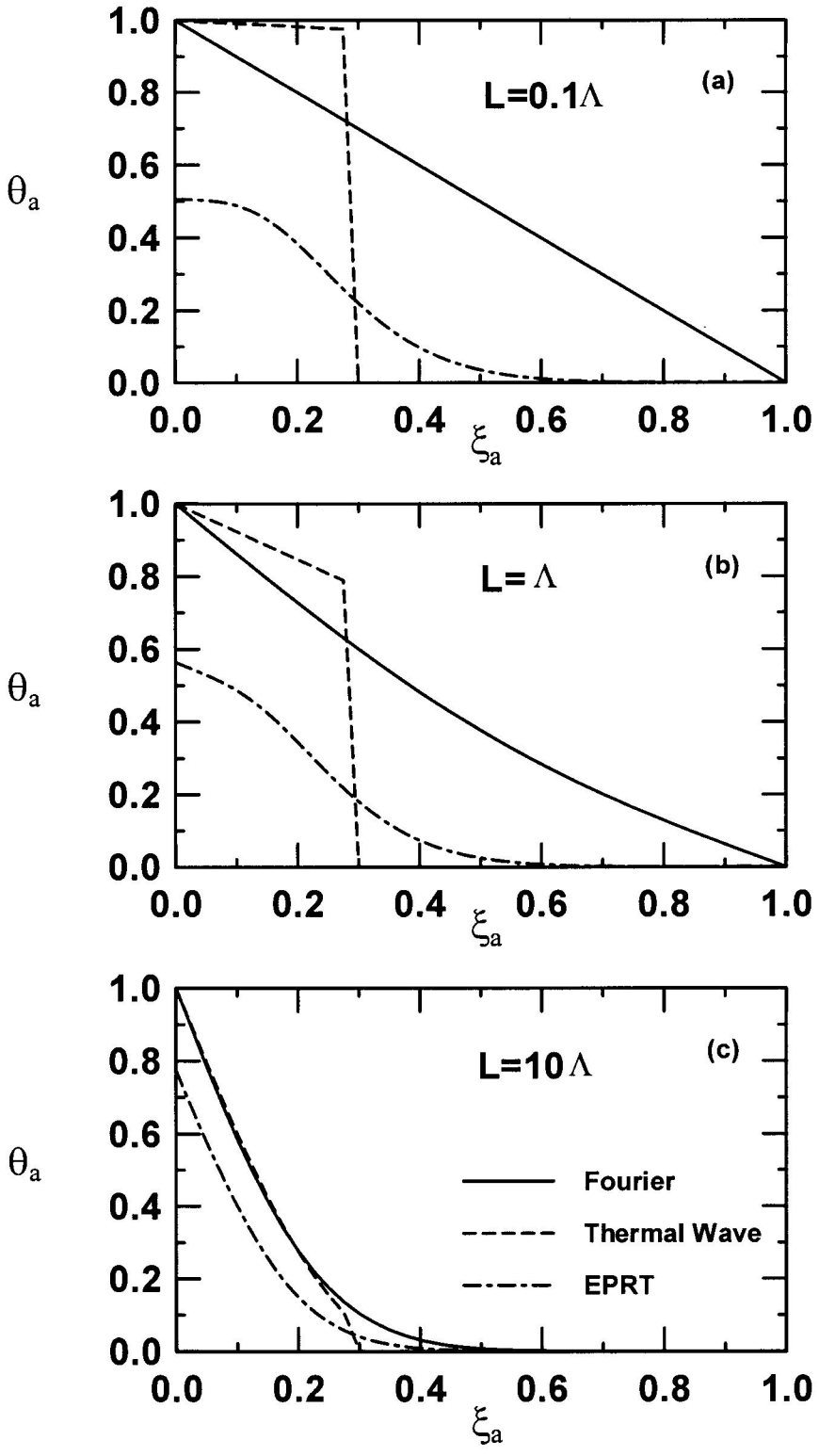

Fig. 2.4 The temperature profiles predicted by Fourier law, thermal wave and EPRT for the films of thickness $L = 0.1$, 1, and $10L$ at dimensionless time $t_a = 0.5$.

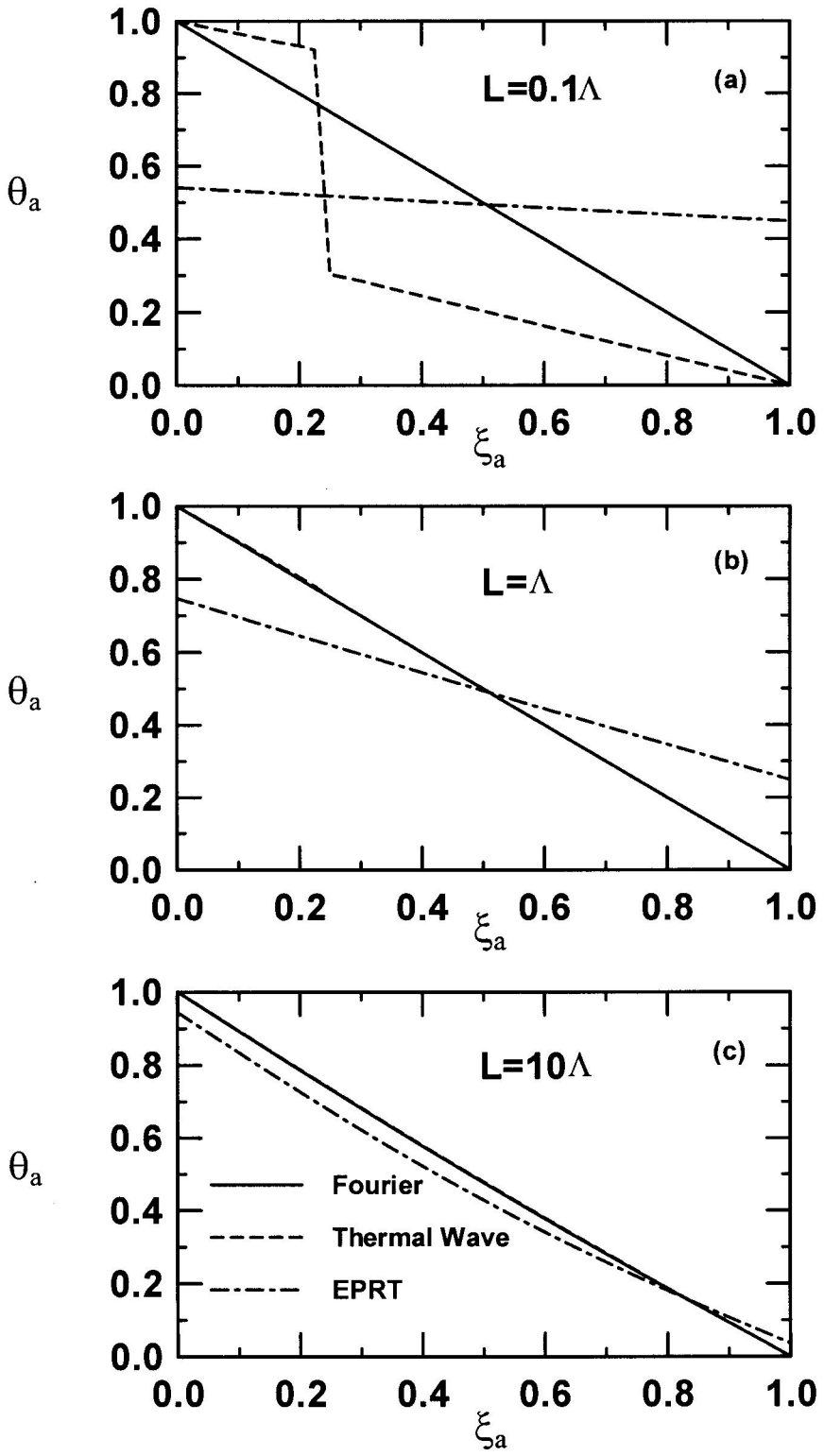

Fig. 2.5 The temperature profiles predicted by Fourier law, thermal wave and EPRT for the films of thickness $L = 0.1$, 1, and $10L$ at dimensionless time $t_a = 10$.

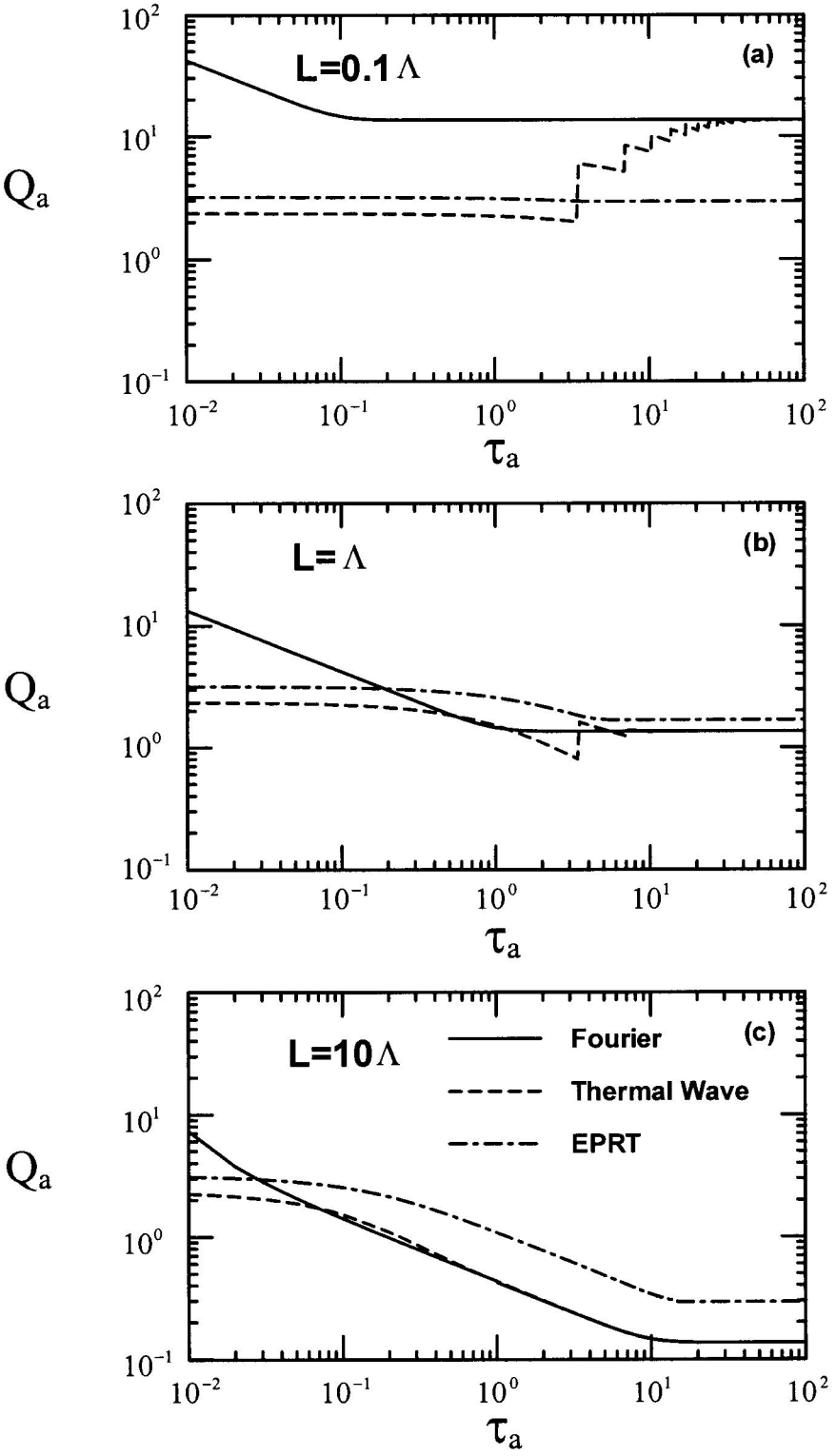

Fig. 2.6 The heat flux history predicted by Fourier law, thermal wave and EPRT at $x_a = 0$ for the films of thickness $L = 0.1$, 1, and $10L$.

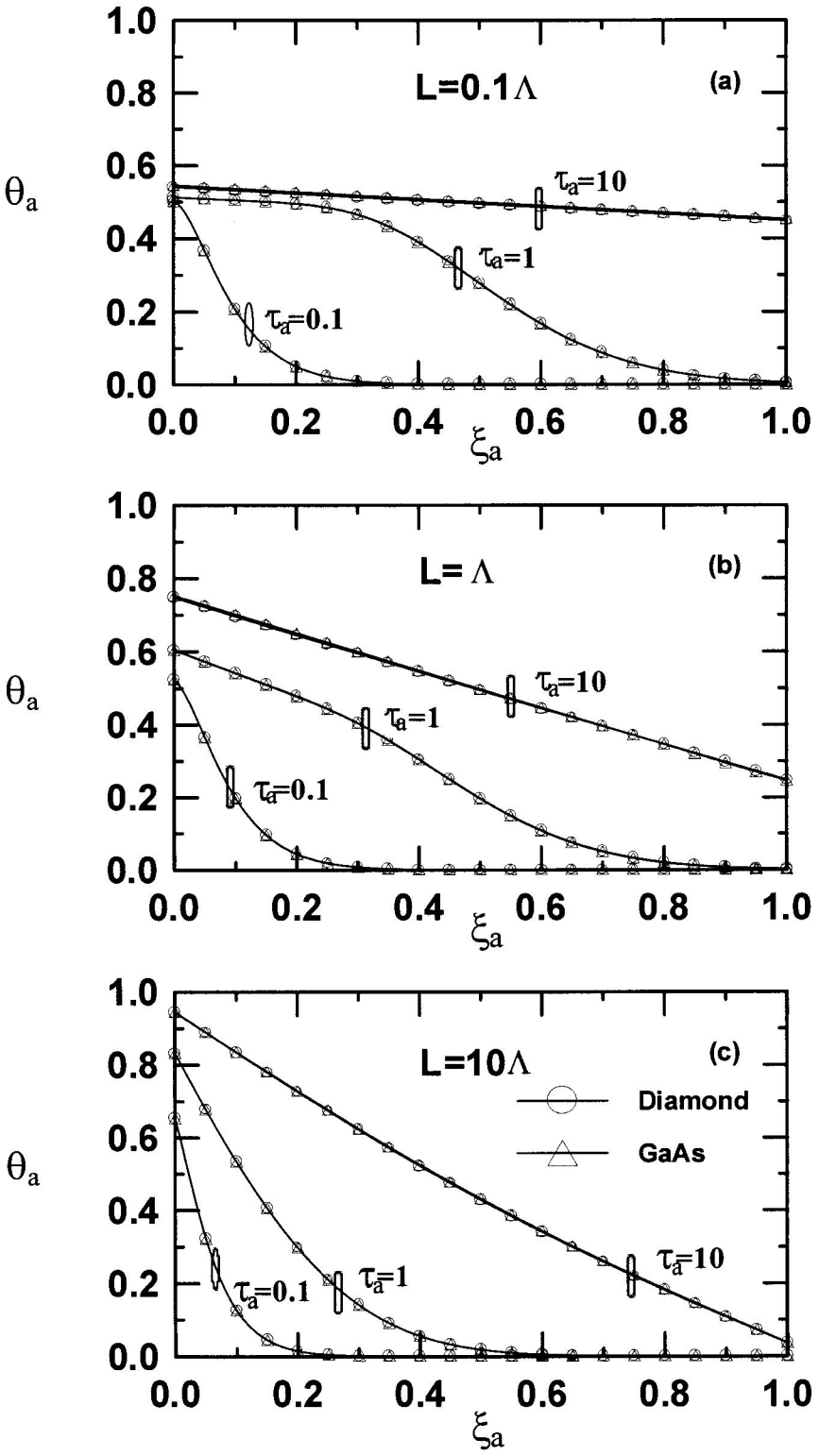

Fig. 2.7 The temperature distributions predicted by EPRT for GaAs and diamond thin films.

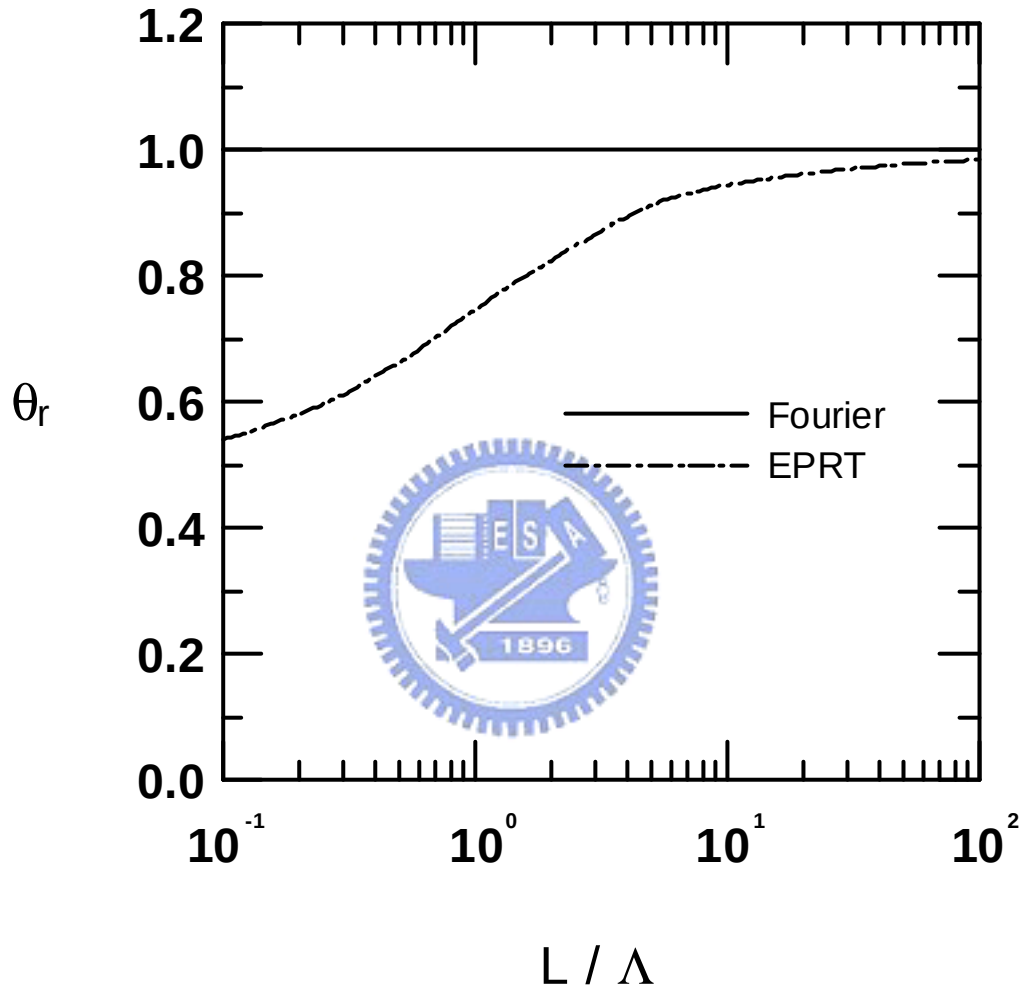

Fig. 2.8 The steady-state boundary temperature predicted by Fourier law and EPRT for different L/L .

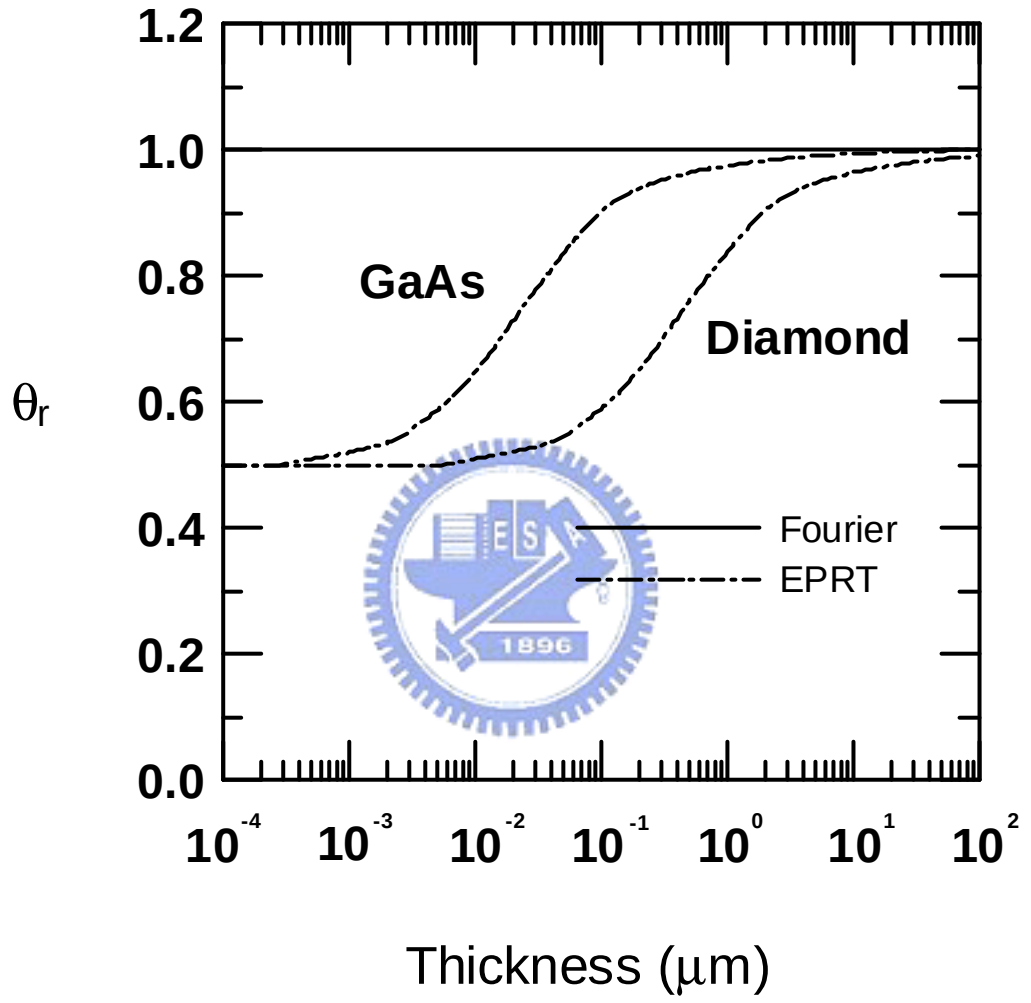

Fig. 2.9 The steady-state boundary temperature of GaAs and diamond thin films predicted by Fourier law and EPRT for different L/L .

3. MICROSCALE HEAT TRANSFER IN MULTILAYER STRUCTURES

Some microscale heat transfer problems are associated with cylindrical geometry. For example, heat transport in silicon and germanium multishell nanowire heterostructures. Lauhon et al. [91] synthesized core-shell nanowires by chemical vapor deposition. Then, they developed a high-performance coaxially gated field-effect transistor of core-shell structures, as illustrated in Fig. 3.1. In this chapter, EPRT and DMM are employed to analyze microscale heat transfer in multilayer structures.

3.1 Analysis

3.1.1 Mathematical Formulation

Phonon heat transfer in dielectric thin films can be modeled by the Boltzmann transport equation [31]. Under the first-order relaxation time approximation, the BTE is reduced to

$$\frac{\partial f_w}{\partial t} + \vec{v} \cdot \nabla f_w = \frac{f_w^0 - f_w}{t_R}, \tag{3-1}$$

where f_w denotes the phonon distribution function as a function of frequency w, f_w^0 represents the equilibrium distribution function, $\vec{v}$ is the group velocity, and t_R denotes the relaxation time. Phonon intensity can be represented as follows

$$I_w = \sum_p v f_w \hbar w D(w), \tag{3-2}$$

where $\hbar$ is the Planck's constant divided by $2p$, D denotes the density of states, and the summation index p is the phonon polarization. Let $\vec{v} = v\vec{e}_v$ and

substituting Eq. (3-2) into Eq. (3-1) yields

$$\frac{1}{v}\frac{\partial I_w}{\partial t}+\vec{e}_v\cdot\nabla I_w=\frac{I_w^0-I_w}{t_R v}. \tag{3-3}$$

The second term on the left-hand-side in the above equation is described in the form [90]

$$\begin{aligned}\vec{e}_v\cdot\nabla I_w &= \frac{dI_w}{ds}=\frac{\partial I_w}{\partial r}\frac{dr}{ds}+\frac{\partial I_w}{\partial z}\frac{dz}{ds}+\frac{\partial I_w}{\partial j}\frac{dj}{ds}\\ &= \sin z\cos j\,\frac{\partial I_w}{\partial r}-\frac{1}{r}\sin z\sin j\,\frac{\partial I_w}{\partial j}\end{aligned}. \tag{3-4}$$

$\frac{\partial I_w}{\partial z}=0$ was employed in the above equation due to axisymmetric assumption. Substituting Eq. (3-4) into Eq. (3-3) and letting $m=\sin z\cos j$, $h=\sin z\sin j$, Eq. (3-3) becomes

$$\frac{1}{v}\frac{\partial I_w}{\partial t}+m\frac{\partial I_w}{\partial r}-\frac{1}{r}h\frac{\partial I_w}{\partial j}=\frac{I_w^0-I_w}{t_R v}. \tag{3-5}$$

The equilibrium phonon intensity I_w^0 can be approximated by assuming equilibrium at every frequency, then

$$I_w^0=\frac{1}{4p}\int_{\Omega=4p} I_w\,d\Omega. \tag{3-6}$$

Substituting Eq. (3-6) into Eq. (3-5) leads to

$$\frac{1}{v}\frac{\partial I_w}{\partial t}+m\frac{\partial I_w}{\partial r}-\frac{1}{r}h\frac{\partial I_w}{\partial j}=\frac{\frac{1}{4p}\int_{\Omega=4p} I_w\,d\Omega-I_w}{t_R v}. \tag{3-7}$$

Equation (3-7) is the equation of phonon radiative transfer (EPRT) for the cylindrical coordinates. Additionally, the heat flux q is

$$q=2p\int_{-1}^{1}\int_{0}^{w_D} mI_w\,dw\,dm, \tag{3-8}$$

where w_D is the Debye cut-off frequency.

This study considers a two-layer concentric cylinder with inner radius r_i and outer radius r_o, as illustrated in Fig. 3.2. The medium temperature initially is T_o. At time $t=0$, the temperature at $r=r_i$ rises to T_i ($T_i > T_o$). Meanwhile, the temperature at $r=r_o$ remains T_o. For convenience, the subsequent analysis assumes the medium to be gray, i.e., frequency independent, while the EPRT can be expressed as

$$\frac{1}{v_k}\frac{\partial I_k}{\partial t} + m\frac{\partial I_k}{\partial r} - \frac{1}{r}h\frac{\partial I_k}{\partial j} = \frac{\frac{1}{4p}\int_{\Omega=4p} I_k d\Omega - I_k}{t_R v_k}, \quad k=1,2. \tag{3-9}$$

The subscript indices $k=1$ and 2 represent layer 1 (inner layer) and layer 2 (outer layer), respectively. The initial conditions of this system can be written as

$$I_k(t=0) = I_k^0(T_o), \quad k=1,2. \tag{3-10}$$

Moreover, the boundary conditions are

$$I_1(r=r_i) = I_1^0(T=T_i), \tag{3-11a}$$

$$I_2(r=r_o) = I_2^0(T=T_o). \tag{3-11b}$$

The energy balance at the interface $(r=r_b)$ between layer 1 and layer 2 is [52]

$$\int_{2p} I_1^-(r_b,-m_1)m_1 dm_1 = R_{12}\int_{2p} I_1^+(r_b,m_1)m_1 dm_1 + a_{21}\int_{2p} I_2^-(r_b,-m_2)m_2 dm_2, \tag{3-12a}$$

$$\int_{2p} I_2^+(r_b,m_2)m_2 dm_2 = R_{21}\int_{2p} I_2^-(r_b,-m_2)m_2 dm_2 + a_{12}\int_{2p} I_1^+(r_b,m_1)m_1 dm_1, \tag{3-12b}$$

where R_{12} and a_{12} represent the energy reflectivity and transmissivity at the interface for phonons from layer 1 to layer 2, and vice versa. The superscripts $+$ and $-$ represent the positive and negative radial directions, respectively. Assuming phonons leaving an interface are isotropically distributed, Eqs. (3-12a) and (3-12b) can be written as

$$I_1^-(r_b,-m_1) = 2R_{12}\int_{2p} I_1^+(r_b,m_1)m_1 dm_1 + 2a_{21}\int_{2p} I_2^-(r_b,-m_2)m_2 dm_2\,, \tag{3-13a}$$

$$I_2^+(r_b,m_2) = 2R_{21}\int_{2p} I_2^-(r_b,-m_2)m_2 dm_2 + 2a_{12}\int_{2p} I_1^+(r_b,m_1)m_1 dm_1\,. \tag{3-13b}$$

Many theories have been developed to describe the interfacial condition between two dissimilar materials, and various a_{ij} have been calculated using different models. Chen [92] derived the energy transmission coefficient for diffuse interface, as follows:

$$a_{ij} = \frac{C_j v_j}{C_i v_i + C_j v_j},\quad i,\ j = 1,\ 2\,, \tag{3-14}$$

where C is the volumetric specific heat and v is the phonon group velocity. The diffuse mismatch model (DMM) is based on the assumption that phonons arriving at the interface totally lose their memory on the side which they come from. Swartz and Pohl [35] stated that the phonon reflectivity from layer 1 to layer 2 equals the phonon transmissivity from layer 2 to layer 1. It can be expressed as

$$a_{ji} = R_{ij},\quad i,\ j = 1,\ 2\,. \tag{3-15}$$

Once the transmissivity is obtained from Eq. (3-14), the reflectivity can be calculated according to the requirement to conserve energy, and thus

$$R_{ij} = 1 - a_{ij},\quad i,\ j = 1,\ 2\,. \tag{3-16}$$

3.1.2 Numerical Method

Since Eq. (3-9) is an integro-differential equation, it is difficult to obtain an exact solution. This study applies a numerical approach to solve this problem. Employing the discrete ordinates method, the integral term is approximated by Gaussian quadrature

$$\int_{\Omega=4p} I d\Omega = \sum_{i=1}^{m} I_i w_i \ , \tag{3-17}$$

where w_i are the weighting factors for the Gaussian quadrature. The governing equation then is transformed to

$$\frac{1}{v_k}\frac{\partial I_{i,k}}{\partial t} + m_i \frac{\partial I_{i,k}}{\partial r} - \frac{1}{r} h_i \frac{\partial I_{i,k}}{\partial j} = \frac{\frac{1}{4p}\sum_{j=1}^{m} I_{j,k} w_j - I_{i,k}}{t_R v_k}, \quad i = 1,2,\cdots,m, \quad k = 1,2 \tag{3-18}$$

Since $m_i = \sin q_i \cos j_i$ and $h_i = \sin q_i \sin j_i$, the above equation can be rewritten as

$$\frac{1}{v_k}\frac{\partial I_{i,k}}{\partial t} + \frac{m_i}{r}\frac{\partial}{\partial r}\left(r I_{i,k}\right) - \frac{1}{r}\frac{\partial}{\partial j}\left(h_i I_{i,k}\right) = \frac{\frac{1}{4p}\sum_{j=1}^{m} I_{j,k} w_j - I_{i,k}}{t_R v_k}. \tag{3-19}$$

The third term on the left-hand-side in Eq. (3-19) can be approximated as [90]

$$\frac{1}{r}\frac{\partial}{\partial j}\left(h_i I_i\right) \cong \frac{1}{r}\frac{A_{i+1/2} I_{i+1/2} - A_{i-1/2} I_{i-1/2}}{4 w_i}, \quad i = 1,2,\cdots,m, \tag{3-20}$$

where coefficient $A_{i+1/2}$ is

$$A_{i+1/2} = A_{i-1/2} + w_i'' m_i, \quad A_{1/2} = A_{m+1/2} = 0, \qquad i = 1,2,\cdots,m. \tag{3-21}$$

Substituting Eq. (3-20) into Eq. (3-19) leads to

$$\frac{1}{v_k}\frac{\partial I_{i,k}}{\partial t} + \frac{m_i}{r}\frac{\partial}{\partial r}\left(r I_{i,k}\right) - \frac{1}{r}\frac{A_{i+1/2} I_{i+1/2,k} - A_{i-1/2} I_{i-1/2,k}}{4 w_i} = \frac{\frac{1}{4p}\sum_{j=1}^{m} I_{j,k} w_j - I_{i,k}}{t_R v_k}, \tag{3-22}$$

where $I_{i+1/2}$ and $I_{i-1/2}$ are expressed as

$$I_{i+1/2} = \frac{I_{i+1} + I_i}{2}, \text{ and } \quad I_{i-1/2} = \frac{I_i + I_{i-1}}{2}. \tag{3-23}$$

Rewriting Eq. (3-22), the governing equations are obtained as

$$\frac{1}{v_k}\frac{\partial I_{i,k}}{\partial t} + m_i \frac{\partial I_{i,k}}{\partial r} + \frac{m_i}{2r} I_{i,k} - \frac{A_{i+1/2} I_{i+1,k} - A_{i-1/2} I_{i-1,k}}{8 r w_i} = \frac{\frac{1}{4p}\sum_{j=1}^{m} I_{j,k} w_j - I_{i,k}}{t_R v_k}. \tag{3-24}$$

In this study, the S_2 scheme, which means $m=2$, is selected to deal with the governing equations. The finite difference method is employed to approximate the differential terms in the governing equations. Backward difference is used in space when $0<m_i<1$ and forward difference is used in space when $-1<m_i<0$. Additionally, forward difference is used in time in both cases. Thus, Eq. (3.24) becomes

$$\frac{1}{v_k}\frac{I_{i,k,j}^{n+1}-I_{i,k,j}^{n}}{Dt}+m_i\frac{I_{i,k,j}^{n}-I_{i,k,j-1}^{n}}{Dr}+\frac{m_i}{2(j-1)Dr}I_{i,k,j}^{n}-\frac{A_{i+1/2}I_{i+1,k,j}^{n}}{8(j-1)Drw_i}$$
$$=\frac{\frac{1}{4p}\sum_{l=1}^{2}I_{l,k,j}^{n}w_l-I_{i,k,j}^{n}}{t_R v_k}, \quad 0<m_i<1, \tag{3-25a}$$

$$\frac{1}{v_k}\frac{I_{i,k,j}^{n+1}-I_{i,k,j}^{n}}{Dt}+m_i\frac{I_{i,k,j+1}^{n}-I_{i,k,j}^{n}}{Dr}+\frac{m_i}{2(j-1)Dr}I_{i,k,j}^{n}-\frac{A_{i+1/2}I_{i+1,k,j}^{n}}{8(j-1)Drw_i}$$
$$=\frac{\frac{1}{4p}\sum_{l=1}^{2}I_{l,k,j}^{n}w_l-I_{i,k,j}^{n}}{t_R v_k}, \quad -1<m_i<0, \tag{3-25b}$$

where n and j represent the time index and the space index in the radial direction, respectively. To solve the simultaneous governing equations, an iterative procedure is performed in this study. The convergence criterion is that the relative error for temperature is less than 10^{-4}.

3.2 Results and Discussion

Grid-refinement and time-step-sensitivity studies have been done to ensure the accuracy of the numerical method and the results are shown in Fig. 3.3. There are 31 grids employed in space and the time step (Dt) is taken as 10 fs. In the following

cases, GaAs/AlAs superlatices [40] and diamond thin film deposited on silicon substrate are selected as examples for demonstration.

Fig. 3.4 shows the transient temperature distributions on GaAs/AlAs superlattices with inner radius $r_i = 10^{-7}$ m under different film thicknesses: (a) $L_1 = L_2 = 5\times10^{-9}$ m, (b) $L_1 = L_2 = 5\times10^{-7}$ m. Due to the ballistic transport of phonons, temperature discontinuities (dropping at high-temperature boundary and jumping at low-temperature boundary) occur at two boundaries. Both temperatures at $r = r_i$ and $r = r_o$ increase with time and approach to the steady state. It is noticed that the dimensionless temperature of layer 2 is zero in the early time ($t < 10^{-10}$ s) for case (b) because it takes time to make phonons thermal equilibrium. Moreover, the tube thickness significantly influences phonon heat transport. Comparing Figs. (3.4a) and (3.4b) reveals that the temperature discontinuities at boundaries decrease with increasing tube thickness. With increasing tube thickness, the temperature profile presents the diffuse-like behavior – that is diffusive transport dominates. Otherwise, ballistic transport dominates, since the tube is thin. Ballistic transport dominates for small length scale which is comparable to phonon mean free path.

The length scale considered here is the micro/nano-meter. In practical engineering applications, steady states are reached within a micro-second. The steady state thus is assumed in the following demonstrating cases. Fig. 3.5 illustrates the effect of tube thickness on the temperature profiles of GaAs/AlAs superlattices at $r_i = 10^{-7}$ m. As mentioned previously, the temperature discontinuities at boundaries decrease with increasing tube thickness. This phenomenon occurs because temperatures drop or jump sharply at boundaries owing to the ballistic transport nature of phonons. However, the temperature discontinuity at the interface results from the dissimilarity between two materials. Notably, the quantity of the temperature

difference divided by the heat flux at the interface is defined as interface thermal resistance (ITR), thus

$$ITR = \frac{DT_{int}}{q}, \tag{3-26}$$

where DT_{int} is the temperature difference at the interface. Numerous models are proposed for describing the interface thermal resistance. This study employs the DMM model. Fig. 3.5 clearly shows that the interface temperature discontinuity increases with decreasing tube thickness. Additionally, the temperature discontinuity also increases at boundaries with decreasing tube thickness. The temperature drop inside each layer is small compared to that at the interface when the layers are very thin. In other words, the thermal resistance at the surfaces, including the boundary and interface, is greater than that inside the materials. Surface properties thus dominate heat transfer in a thin tube.

Fig. 3.6 displays the effect of curvature on the temperature profiles of GaAs/AlAs superlattices at $L_1 = L_2 = 10^{-7}$ m. Notably, the temperature profile approaches that for slab when the inner radius (r_i) is large. In this case, no obvious difference exists between slab and $r_i = 10^{-5}$ m. This phenomenon can be explained by Eq. (3-9). Once the term $\frac{1}{r} h \frac{\partial I_w}{\partial j}$ equals zero, Eq. (3-9) is reduced to the governing equation for a slab. Large r_i makes $\frac{1}{r} h \frac{\partial I_w}{\partial j}$ small compared to other terms in Eq. (3-9), and thus the temperature profiles for large r_i approach those for a slab.

The Fourier law is known to be inadequate for analyzing microscale heat transfer behavior. However, effective thermal conductivity offers an efficient concept for

calculating the heat transfer rate. According to the Fourier law, the effective thermal conductivity k_{eff} is defined as [93]

$$k_{eff} = \frac{Q_T \ln(r_o / r_i)}{2p(T_i - T_o)}, \tag{3-27}$$

where Q_T is the total net radial heat transfer. To show the effect of film thickness on thermal conductivity, the plane-parallel GaAs/AlAs superlattices are chosen for a demonstration. Furthermore, the numerical calculations are compared to the experimental data. Fig. 3.7 reveals that the thermal conductivity of GaAs/AlAs superlattices is smaller than its bulk value. Additionally, the thermal conductivity decreases with decreasing film thickness. The simulation results agree closely with the experimental data. The miniaturization of microelectronic devices reduces the heat transfer ability and causes device failure if the size effect is ignored. The size effect thus must be considered when designing a microelectronic device.

Fig. 3.8 illustrates the effect of curvature on the thermal conductivity of GaAs/AlAs superlattices. Three inner radii: $r_i = 10^{-5}$ m, $r_i = 10^{-6}$ m, and $r_i = 10^{-7}$ m are chosen as examples. The thermal conductivity increases with the increasing curvature. Moreover, this phenomenon is amplified by large tube thickness. However, no obvious difference exists among these three cases when the tube is getting thinner. When the film thickness is small compared to its inner radius, the phonon transport in the ultra-thin tube approaches that in the slab. Consequently, the effect of curvature on thermal conductivity decreases with decreasing tube thickness. Size effect rather than curvature effect thus dominates the heat transfer behavior in an ultra-thin tube.

Because the interface thermal resistance is a significant determinant of heat flow rate of multi-layered structures, interface thermal resistance behavior must be examined closely. Fig. 3.9 shows the effect of curvature on the interface thermal

resistance of GaAs/AlAs superlattices. The figure reveals that no visible discrepancy exists under three different inner radii, indicating that the effect of curvature on the interface thermal resistance of GaAs/AlAs superlattices is insignificant. Additionally, the size effect on the interface thermal resistance is also unimportant. The size and curvature effects on the interface thermal resistance are not significant if the diffuse mismatch model is employed to describe the interface condition.

Since the curvature effect on the interface is insignificant in this study (DMM is employed), a plane-parallel diamond thin film deposited on the silicon substrate is used to illustrate the behavior of the interface thermal resistance. Fig. 3.10 displays the comparison of interface thermal resistance for diamond/silicon with experimental data. The calculated interface thermal resistance is smaller than the experimental value. Since DMM is a simplified model, it can not completely describe the interface condition. The interface roughness, inelastic scattering resulting from the anharmonic interatomic force interaction, and the phonon mode conversion at the interface may cause diffuse scattering at the interface. Additionally, measurement errors may also contribute the discrepancy between the numerically predicted and experimental values. All of them make the calculated interface thermal resistance lower than the experimental value.

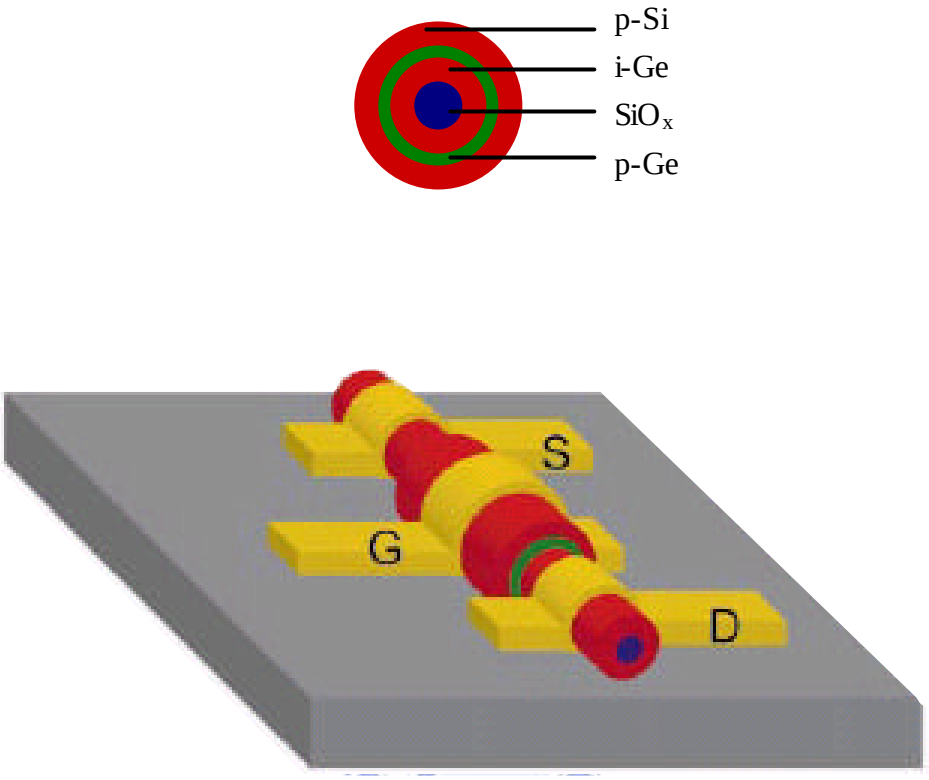

Fig. 3.1 Schematic diagram of coaxially-gated nanowire transistors [91].

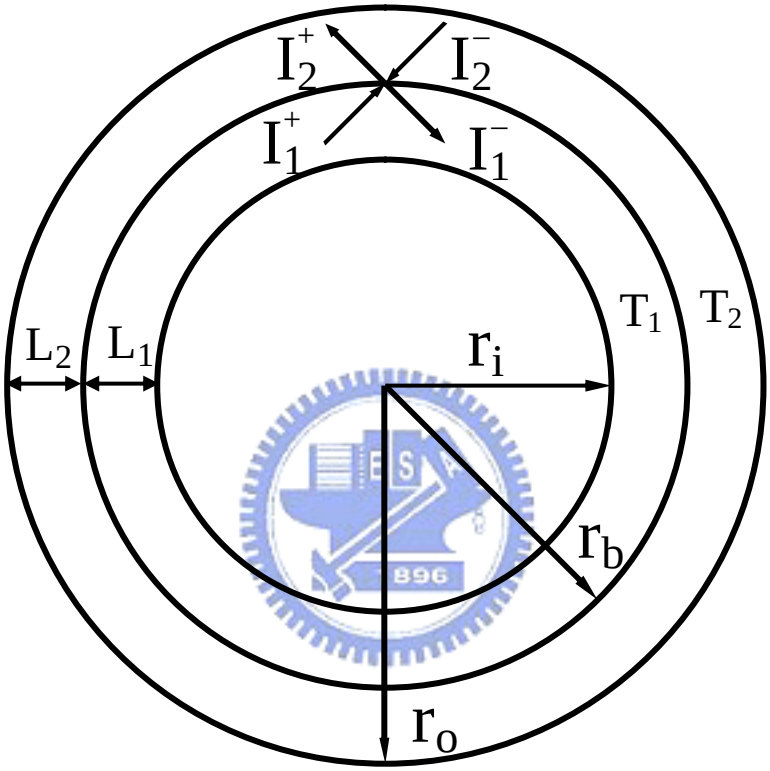

Fig. 3.2 Schematic diagram of the physical system.

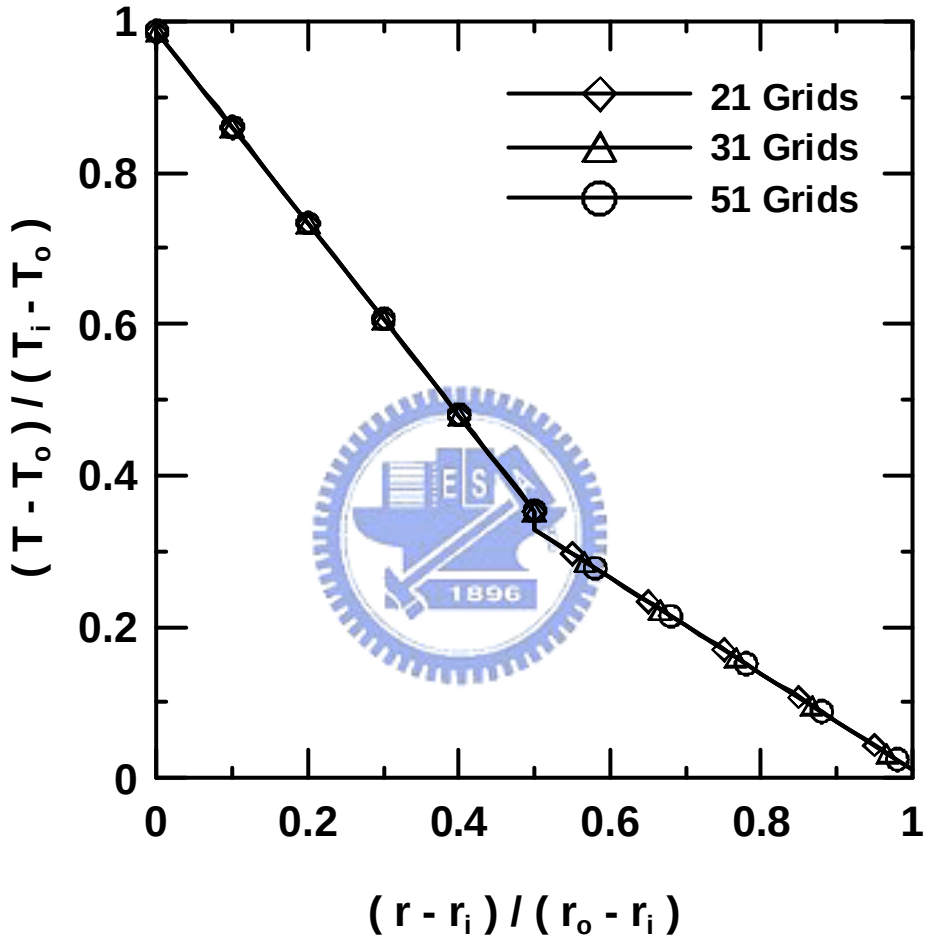

Fig. 3.3 Grid-refinement test for the numerical scheme.

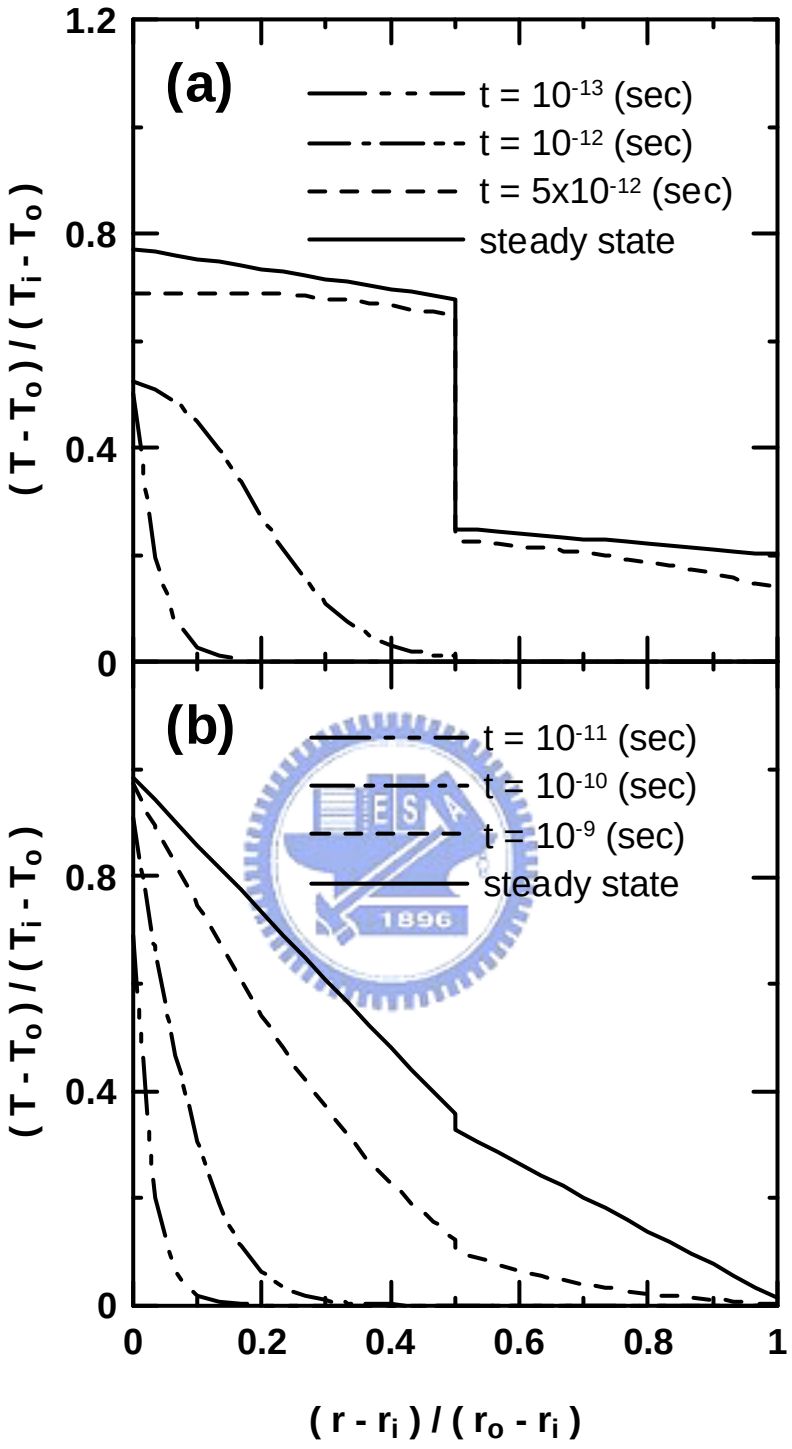

Fig. 3.4 Transient temperature distributions on GaAs/AlAs superlattices with $r_i = 10^{-7}$ m under different film thicknesses: (a) $L_1 = L_2 = 5\times10^{-9}$ m, (b) $L_1 = L_2 = 5\times10^{-7}$ m.

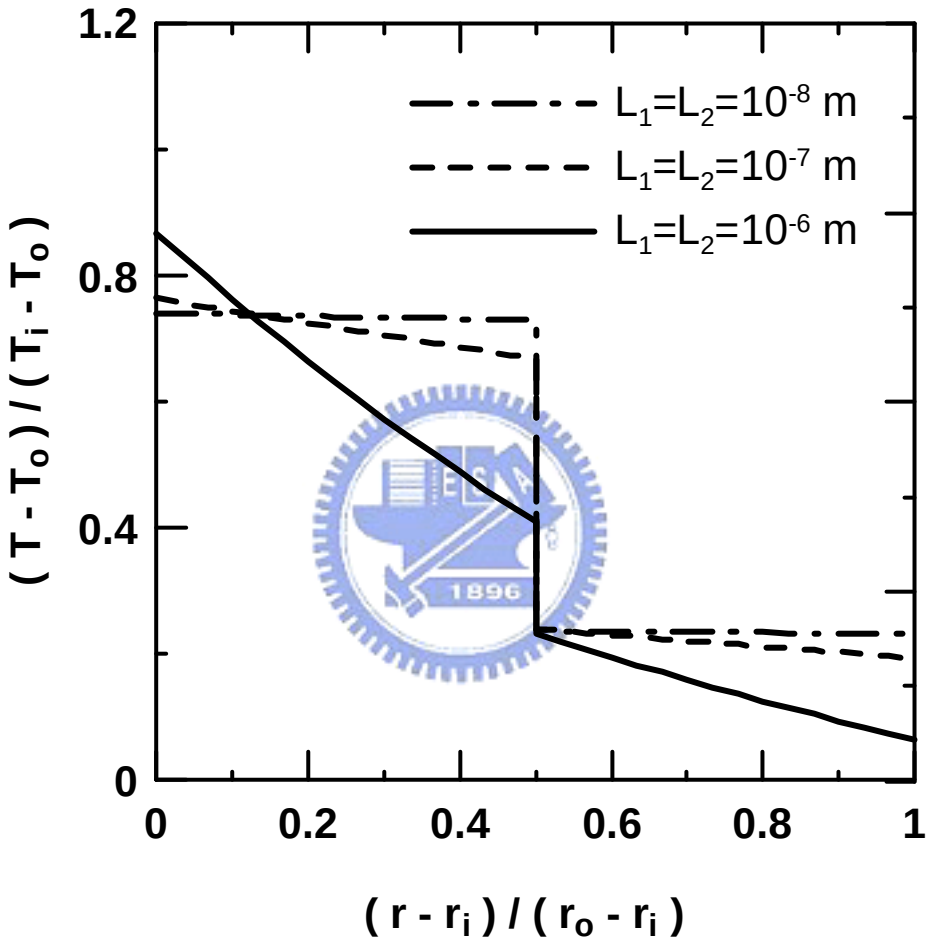

Fig. 3.5 Effect of tube thickness on the temperature profiles of GaAs/AlAs superlattices with $r_i = 10^{-7}$ m.

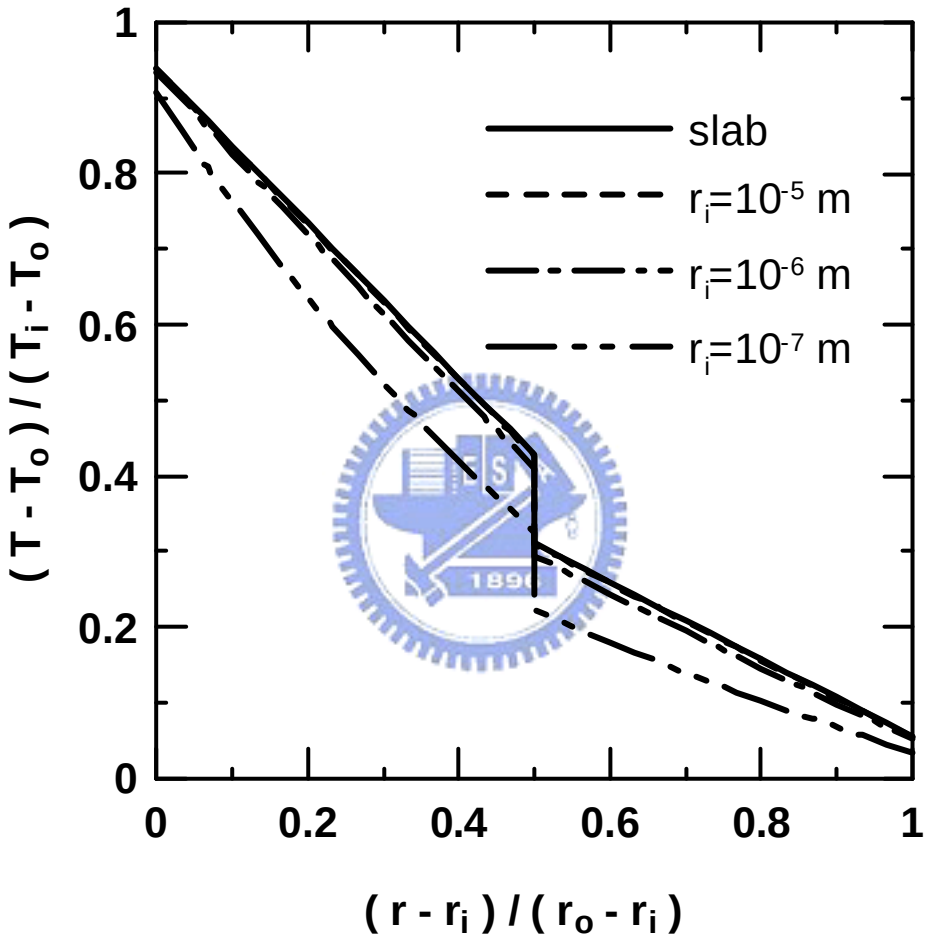

Fig. 3.6 Effect of curvature on the temperature profiles of GaAs/AlAs superlattices with $L_1 = L_2 = 10^{-7}$ m.

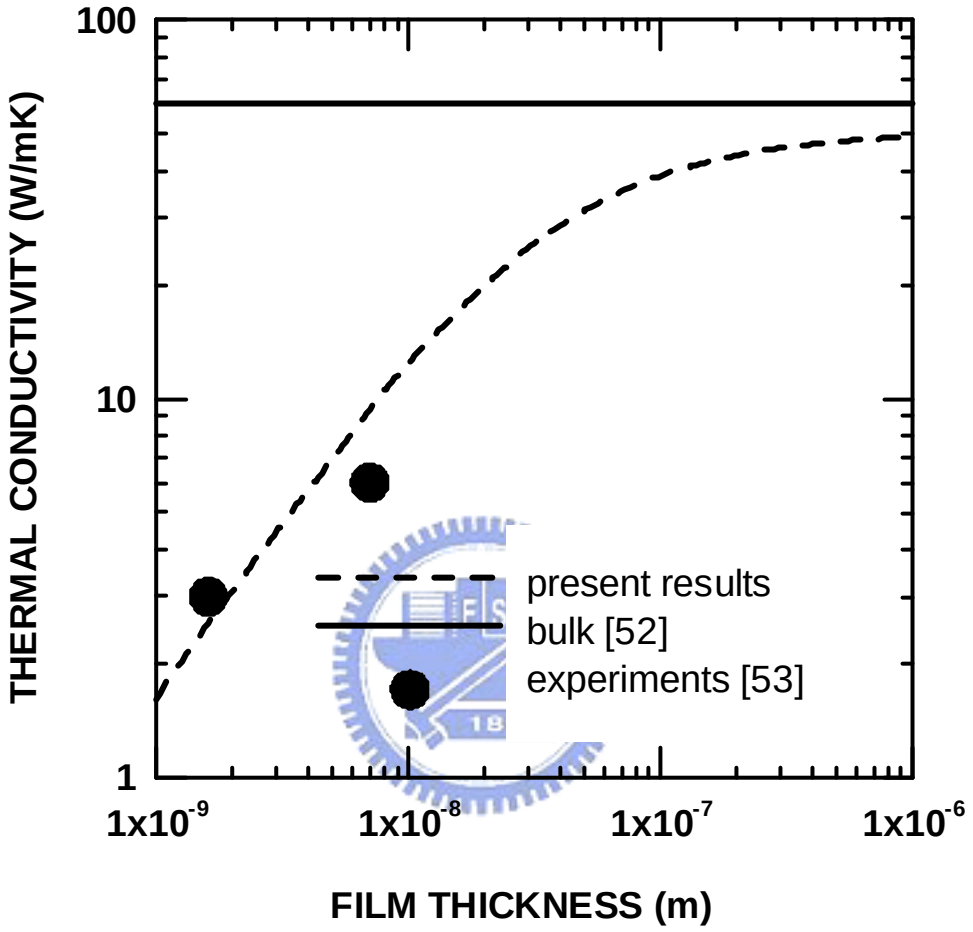

Fig. 3.7 Effect of film thickness on the thermal conductivity of GaAs/AlAs superlattices.

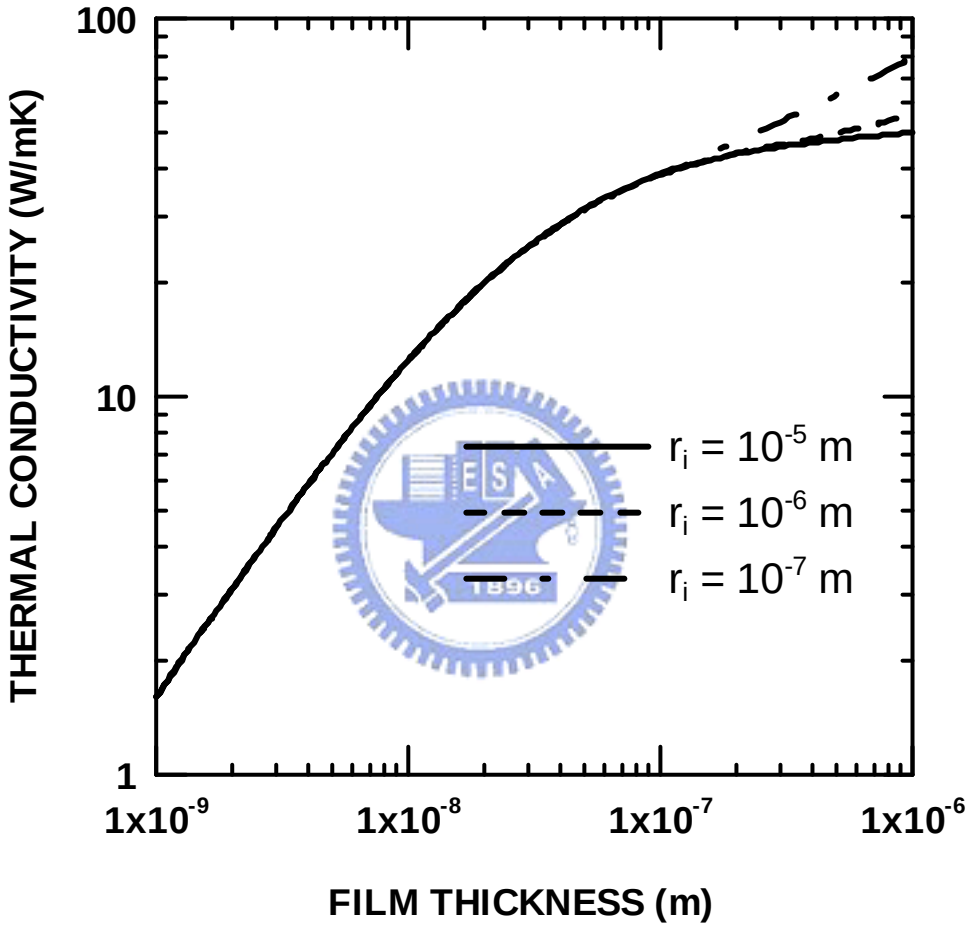

Fig. 3.8 Effect of curvature on the thermal conductivity of GaAs/AlAs superlattices.

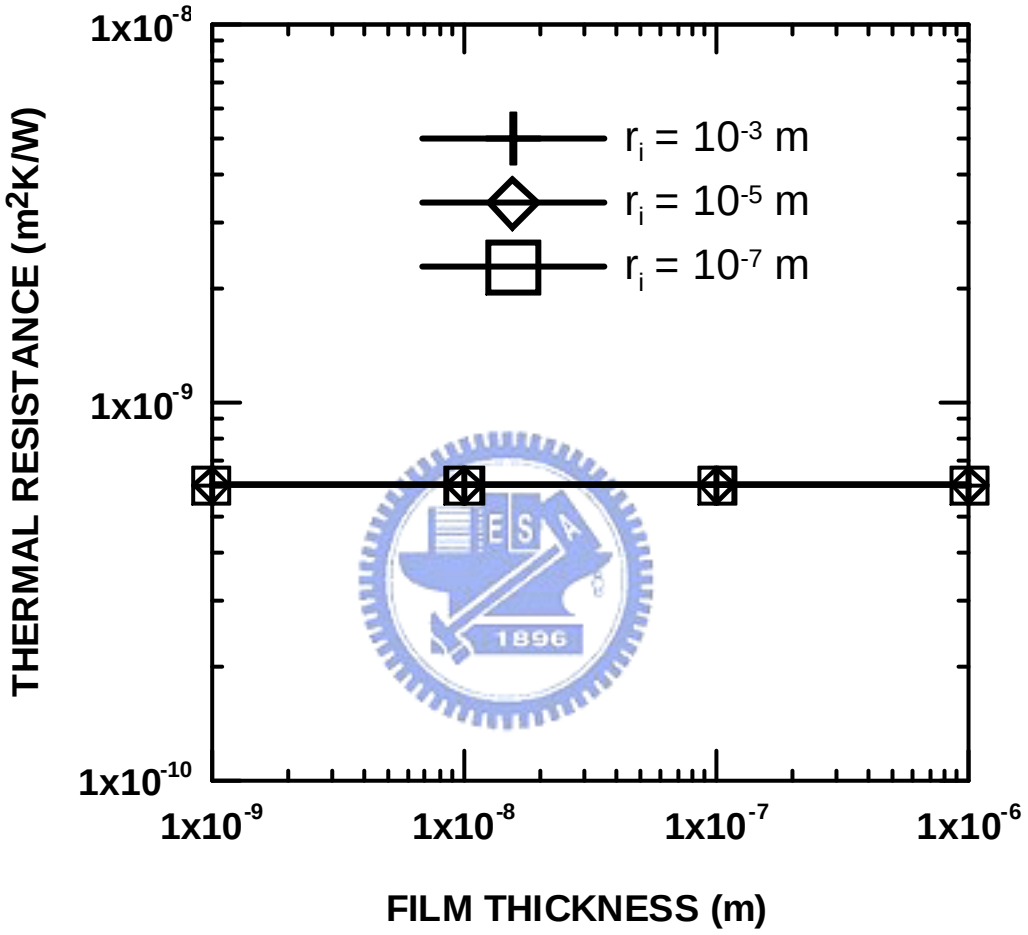

Fig. 3.9 Effect of curvature on the interface thermal resistance of GaAs/AlAs superlattices.

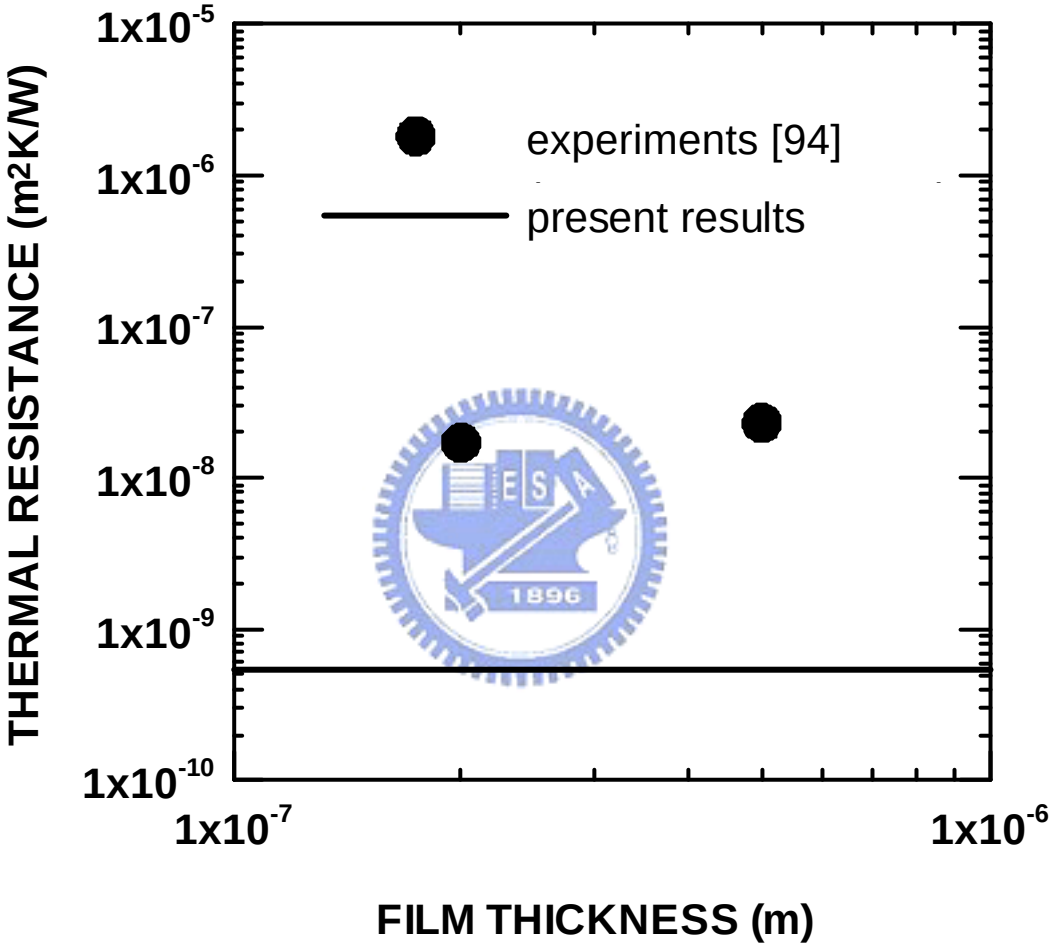

Fig. 3.10 Comparison of interface thermal resistance for diamond/silicon with experimental data.

4. MICROSCALE HEAT TRANSFER IN TWO-DIMENSIONAL MICRO TUBES

There are many applications that require a material with high thermal conductivity, high strength and minimum weight. Hollow diamond micro tubes made by CVD are potential candidates [95]. Thus, it is important to assure the ability of heat dissipation in micro tubes. In this chapter, a two-dimensional EPRT is derived to analyze microscale heat tranfer in micro tubes.

4.1 Analysis

4.1.1 Mathematical Formulation

Phonon heat transfer in dielectric micro tubes can be modeled by the Boltzmann transport equation. The scattering mechanism is difficult to simulate. Majumdar [31] used the first-order relaxation-time approximation to approach the scattering term in BTE. Thus, the Boltzmann equation was reduced to

$$\frac{\partial f_w}{\partial t} + \vec{v} \cdot \nabla f_w = \frac{f_w^0 - f_w}{t_R}, \tag{4-1}$$

where f_w is the phonon distribution function as a function of frequency w, f_w^0 is the equilibrium distribution function, $\vec{v} = v\vec{e}$ is the group velocity, and t_R is the relaxation time. One can define the intensity of phonons as follows

$$I_w = \sum_p \vec{v}_p f_w \hbar w D(w), \tag{4-2}$$

where $\hbar$ is the Plank's constant divided by $2p$, D is the density of states, and the summation index p is the phonon polarization. Multiplying Eq. (4-1) by $v\hbar wD(w)$, the Boltzmann equation can be transformed to

$$\frac{1}{v}\frac{\partial I_w}{\partial t}+\vec{e}_v\cdot\nabla I_w=\frac{I_w^0-I_w}{vt_R}. \tag{4-3}$$

This study considers a two-dimensional hollow cylinder of inner radius r_i, outer radius r_o and height L_a, as illustrated in Fig. 4.1. The second term of the left-hand-side in the Eq. (4-3) is described in the form

$$\vec{e}_v\cdot\nabla I_w=\frac{dI_w}{ds}=\frac{\partial I_w}{\partial r}\frac{dr}{ds}+\frac{\partial I_w}{\partial f}\frac{df}{ds}+\frac{\partial I_w}{\partial z}\frac{dz}{ds}+\frac{\partial I_w}{\partial z}\frac{dz}{ds}, \tag{4-4}$$

where $\frac{dr}{ds}=\sin z\cos f$, $\frac{df}{ds}=-\frac{\sin z\sin f}{r}$, $\frac{dz}{ds}=0$, and $\frac{dz}{ds}=\cos z$. Substituting Eq. (4-4) into Eq. (4-3), and then

$$\frac{1}{v}\frac{\partial I_w}{\partial t}+\frac{m}{r}\left[\frac{\partial(rI_w)}{\partial r}\right]-\frac{1}{r}\left[\frac{\partial(hI_w)}{\partial f}\right]+y\left[\frac{\partial I_w}{\partial z}\right]=\frac{I_w^0-I_w}{vt_R}, \tag{4-5}$$

where $m=\sin z\cos f$, $h=\sin z\sin f$, and $y=\cos z$.

Assume that the equilibrium phonon intensity I_w^0 can be approximated to the average over all solid angle, and thus

$$I_w^0=\frac{1}{4p}\int_{4p} I_w\,d\Omega. \tag{4-6}$$

Substituting Eq. (4-6) into Eq. (4-5) leads to

$$\frac{1}{v}\frac{\partial I_w}{\partial t}+\frac{m}{r}\left[\frac{\partial(rI_w)}{\partial r}\right]-\frac{1}{r}\left[\frac{\partial(hI_w)}{\partial f}\right]+y\left[\frac{\partial I_w}{\partial z}\right]=\frac{\frac{1}{4p}\int_{4p} I_w\,dW-I_w}{vt_R}. \tag{4-7}$$

Eq. (4-7) is the equation of phonon radiative transfer for the cylindrical coordinate.

For convenience in the subsequent analysis, the medium is assumed to be gray, i.e., frequency independent. The steady-state EPRT can be expressed as

$$\frac{m}{r}\left[\frac{\partial(rI)}{\partial r}\right]-\frac{1}{r}\left[\frac{\partial(hI)}{\partial f}\right]+y\left[\frac{\partial I}{\partial z}\right]=\frac{\frac{1}{4p}\int_{4p} I\,dW-I}{vt_R}. \tag{4-8}$$

Consider the temperatures of the top surface ($z = L_a$) and the inner surface ($r = r_i$) are maintained at $T = T_i$. The temperatures of other two surfaces (bottom and outer surfaces) are $T = T_o$, where $T_i > T_o$. The boundary conditions can be expressed as

$$I(r = r_i) = I(z = L_a) = I^0(T_i), \tag{4-9a}$$

$$I(r = r_o) = I(z = 0) = I^0(T_o). \tag{4-9b}$$

4.1.2 Numerical Method

Since Eq. (4-8) is an integro-differential equation, it is difficult to obtain the exact solution. Numerical approach is used to solve it. Employing the discrete ordinates method, the integral term of the right-hand-side in Eq. (4-8) is approximated by Gaussian quadratures

$$\int_{4p} I d\Omega \cong \sum_m w_m I_m , \tag{4-10}$$

where w_m are the weighting factors.

Substituting Eq.(4-10) into Eq. (4-8) leads to

$$\frac{m_m}{r}\left[\frac{\partial(rI_m)}{\partial r}\right] - \frac{1}{r}\left[\frac{\partial(h_m I_m)}{\partial f}\right]_{f=f_m} + y_m\left[\frac{\partial I_m}{\partial z}\right] = \frac{\frac{1}{4p}\sum_m w_m I_m - I_m}{vt_R} . \tag{4-11}$$

The third term of the left-hand-side in Eq. (4-11) is approximated by central difference technique. Then, this term is transformed to

$$\left\{\frac{\partial}{\partial f}(hI)\right\}_{f=f_m} \cong \frac{A_{m+1/2} I_{m+1/2} - A_{m-1/2} I_{m-1/2}}{w_m}, \qquad m = 1,2,....,N . \tag{4-12}$$

Thus, Eq. (4-11) becomes

$$\frac{1}{v}\frac{m_m}{r}\left[\frac{\partial(rI_m)}{\partial r}\right]-\frac{1}{r}\frac{A_{mi+1/2}I_{m+1/2}-A_{m-1/2}I_{m-1/2}}{w_m}+y_m\left[\frac{\partial I_m}{\partial z}\right]=\frac{\frac{1}{4p}\sum_m w_m I_m - I_m}{vt_R},$$

(4-13)

where

$$A_{m+1/2}=w_m m_m + A_{m-1/2},\quad A_{1/2}=A_{N+1/2}=0,\quad m=1,2,....,N_m. \tag{4-14}$$

The S_8 scheme, $N_m=8$, is employed in this study. Forward and backward difference approximations are utilized in negative and positive directions, respectively. The governing equations become

$$m_m\frac{I_{m,i,j}-I_{m,i-1,j}}{Dr}+\frac{m_m}{2(i-1)Dr}I_{m,i,j}-\frac{A_{m+1/2}I_{m+1,i,j}-A_{m-1/2}I_{m-1,i,j}}{2(i-1)Drw_m}$$
$$+y_m\frac{I_{m,i,j}-I_{m,i,j-1}}{Dz}=\frac{\frac{1}{4p}\sum_{m=1}^{8}w_m I_{m,i,j}-I_{m,i,j}}{vt_R},\quad \begin{cases}0<m_m<1\\0<y_m<1\end{cases}, \tag{4-15a}$$

$$m_m\frac{I_{m,i,j}-I_{m,i-1,j}}{Dr}+\frac{m_m}{2(i-1)Dr}I_{m,i,j}-\frac{A_{m+1/2}I_{m+1,i,j}-A_{m-1/2}I_{m-1,i,j}}{2(i-1)Drw_m}$$
$$+y_m\frac{I_{m,i,j+1}-I_{m,i,j}}{Dz}=\frac{\frac{1}{4p}\sum_{m=1}^{8}w_m I_{m,i,j}-I_{m,i,j}}{vt_R},\quad \begin{cases}0<m_m<1\\-1<y_m<0\end{cases}, \tag{4-15b}$$

$$m_m\frac{I_{m,i+1,j}-I_{m,i,j}}{Dr}+\frac{m_m}{2(i-1)Dr}I_{m,i,j}-\frac{A_{m+1/2}I_{m+1,i,j}-A_{m-1/2}I_{m-1,i,j}}{2(i-1)Drw_m}$$
$$+y_m\frac{I_{m,i,j}-I_{m,i,j-1}}{Dz}=\frac{\frac{1}{4p}\sum_{m=1}^{8}w_m I_{m,i,j}-I_{m,i,j}}{vt_R},\quad \begin{cases}-1<m_m<0\\0<y_m<1\end{cases}, \tag{4-15c}$$

$$\mu_m \frac{I_{m,i+1,j} - I_{m,i,j}}{Dr} + \frac{\mu_m}{2(i-1)Dr} I_{m,i,j} - \frac{A_{m+1/2} I_{m+1,i,j} - A_{m-1/2} I_{m-1,i,j}}{2(i-1)Dr w_m} + \eta_m \frac{I_{m,i,j+1} - I_{m,i,j}}{Dz} = \frac{\frac{1}{4p}\sum_{m=1}^{8} w_m I_{m,i,j} - I_{m,i,j}}{v t_R}, \quad \begin{cases} -1 < \mu_m < 0 \\ -1 < \eta_m < 0 \end{cases}, \tag{4-15d}$$

Since the governing system is a set of simultaneous equations, iterative method is used to solve this problem. The convergence criterion is that the relative error for temperature is less than 10^{-4}.

4.2 Results and Discussion

The governing equations deal with the heat conduction in two-dimensional micro tubes. By using the discrete ordinates method, the approximated solutions can be derived. The grid-refinement study, as shown in Fig. 4.2, has been done to ensure the accuracy of the numerical method and the 30×30 grid is employed. In the following cases, diamond is chosen as an example for the demonstration.

Majumdar [31] had obtained microscale heat transfer across diamond thin films by solving the one-dimensional EPRT in the rectangular coordinate. In order to demonstrate the accuracy of the present numerical method, a very long tube with very small curvature is chosen to approach the slab. Fig. 4.3 shows the temperature profiles predicted by the EPRT under different tube thickness with a inner radius $r_i = 1\,mm$ and a tube height $L_a = 10{,}000\,L$. The present results have excellent agreement with the results of Joshi and Majumdar [30].

Fig. 4.4 displays the effect of tube thickness on the radial temperature distributions in the middle plane ($z = 0.5L_a$) with the inner radius $r_i = 10\,mm$ and the tube height $L_a = 10L$. Three different tube thickness, $r_a = 10L$, $r_a = 1L$ and

$r_a = 0.1L$ are utilized to examine the size effects. From Fig. 4.4, it is noticed that the temperature jump and drop at two boundaries are found. The temperature discontinuities at two boundaries decrease as the tube thickness increase. The reason that temperature jump and drop occur at two boundaries is the nonlocal and nonequilibrium ballistic transport nature of phonons. In the limit of no internal scattering, the phonon excited by the hot and the cool walls propagates in the opposite directions without interacting with each other. The lacking of interaction implies that the two groups of phonons will not reach a local equilibrium state with each other. Thus the temperature discontinuity appears. In the case of $r_a = 0.1L$, such thin thickness reduces the probability of internal scattering within the medium; therefore phonons scatter only at boundaries. This is the so-called ballistic heat transport. As the increasing of tube thickness, internal scattering takes place more frequently, and the heat transport is more diffuse-like. The results of Fig. 4.4 are similar to the results of Fig. 4.3. However, owing to the effect of curvature, the temperature distributions are not linear.

Fig. 4.5 shows the effect of tube thickness on the axial temperature distributions at the location $r = 0.5(r_i + r_o)$ with the inner radius $r_i = 10\ mm$ and the tube height $L_a = 10L$. Similar to the Fig. 4.4, the ballistic heat transport dominates while the tube is ultra-thin. Since the tube height is ten times of the phonon mean free path, the heat transport is diffuse-like across the axial direction. In the case of $r_a = 10L$, both axial and radial directions are diffuse transport dominant. In the cases of $r_a = 0.1L$ and $r_a = 1L$, diffuse dominant in the axial direction but ballistic transport in the radial direction. Thus, the axial temperature distributions are different from those of Fig. 4.4.

It is well known that Fourier law is inadequate to analyze microscale heat

conduction. However, the concept of effective thermal conductivity is an effective way to estimate the heat dissipative ability of the materials. The radial and axial effective thermal conductivity are defined as

$$k_{r,eff} = \frac{q_r (r_o - r_i)}{(T_i - T_o)}, \tag{4-16a}$$

$$k_{z,eff} = \frac{q_z L_a}{(T_i - T_o)}, \tag{4-16b}$$

where the heat flux is

$$q_r = \sum_m m_m w_m I_m , \tag{4-17a}$$

$$q_z = \sum_m y_m w_m I_m . \tag{4-17b}$$

Fig. 4.6 and Fig. 4.7 show the size effects on the thermal conductivity under different tube heights in the radial and axial directions, respectively. The thermal conductivity of diamond micro tubes is smaller than its bulk value. The radial thermal conductivity decreases as tube thickness decreases. Similarly, the radial thermal conductivity of a tube with $L_a = 1L$ is small than that of $L_a = 50L$. It can be concluded that the reduction of size, no matter the radial or axial directions, will reduce the thermal conductivity of the material. From Fig. 4.6, it is noticed that the radial thermal conductivity approaches to the bulk value when the tube is getting thick. Fig. 4.7 have similar trend as Fig. 4.6. However, the axial thermal conductivity varies very small as the tube thickness decreases. The tube height is more important than the tube thickness in calculating the axial thermal conductivity. The axial thermal conductivity does not approach the bulk value if the tube is short. The small tube height restricts the axial thermal conductivity growing although the tube is thick enough.

Fig. 4.8 and Fig. 4.9 depict the effect of curvature on the radial and axial thermal conductivities at different tube heights. The radial and axial thermal conductivities do

not vary with different curvature. The effect of tube curvature is not significant on the effective thermal conductivity.

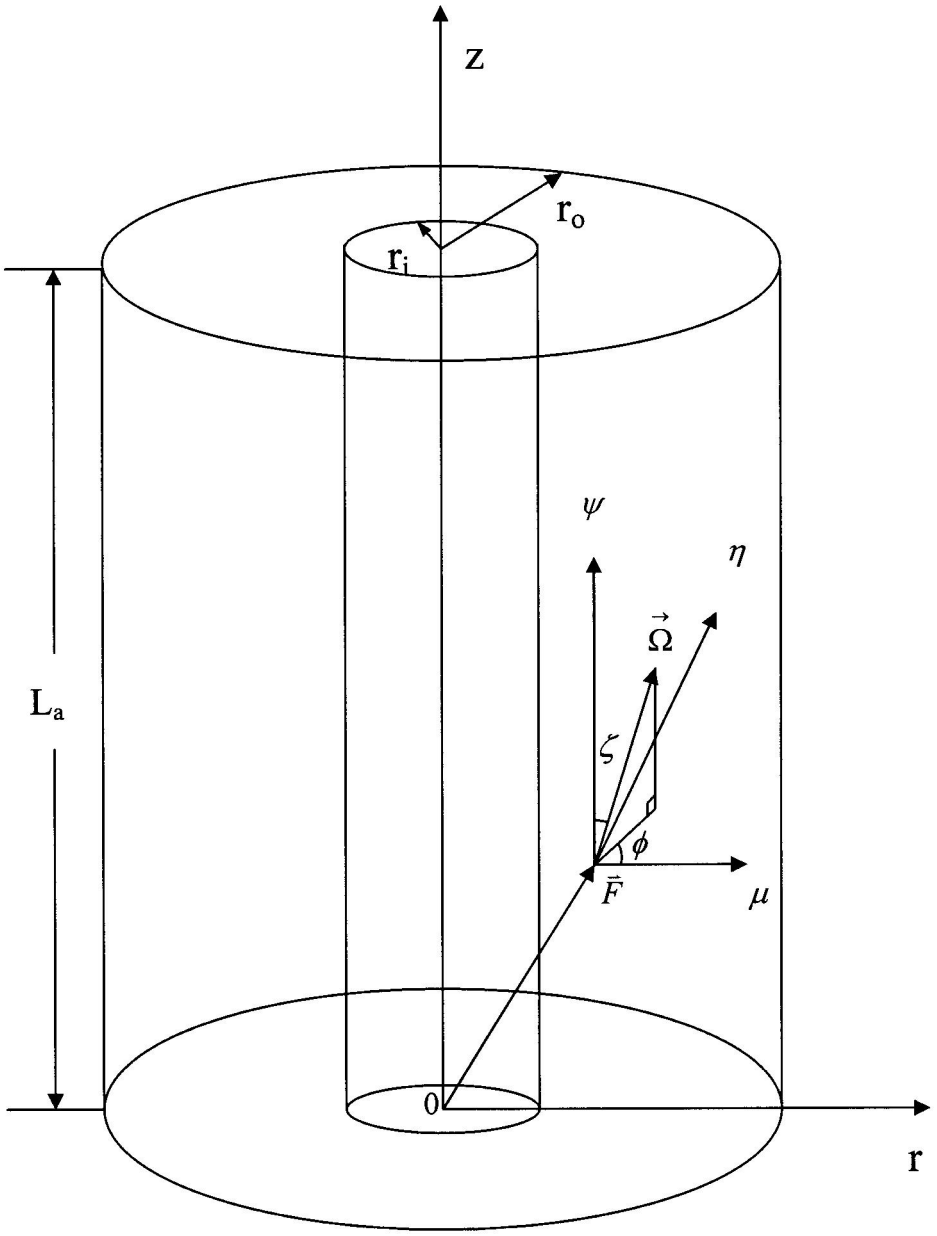

Fig. 4.1 Schematic diagram of the physical system.

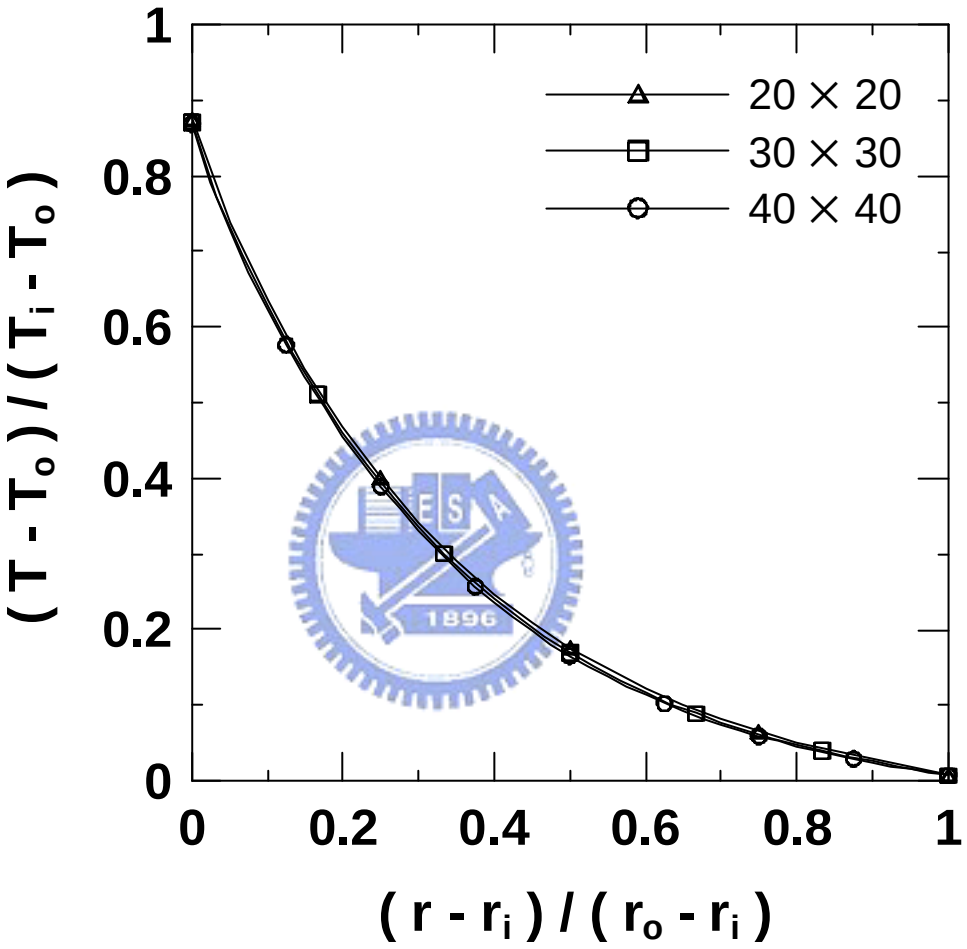

Fig. 4.2 Grid-refinement test for the numerical scheme.

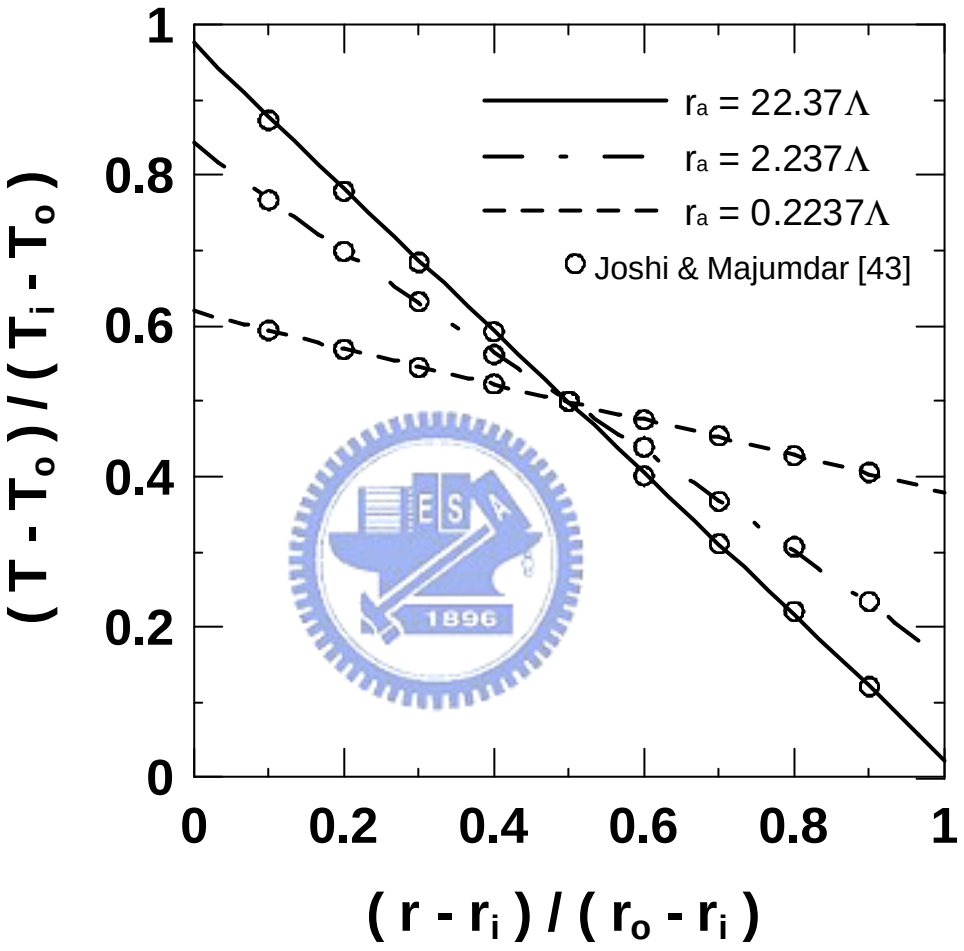

Fig. 4.3 Temperature profiles of diamond tube under different tube thickness at the inner radius $r_i = 1\,mm$ and the tube height $L_a = 10000L$.

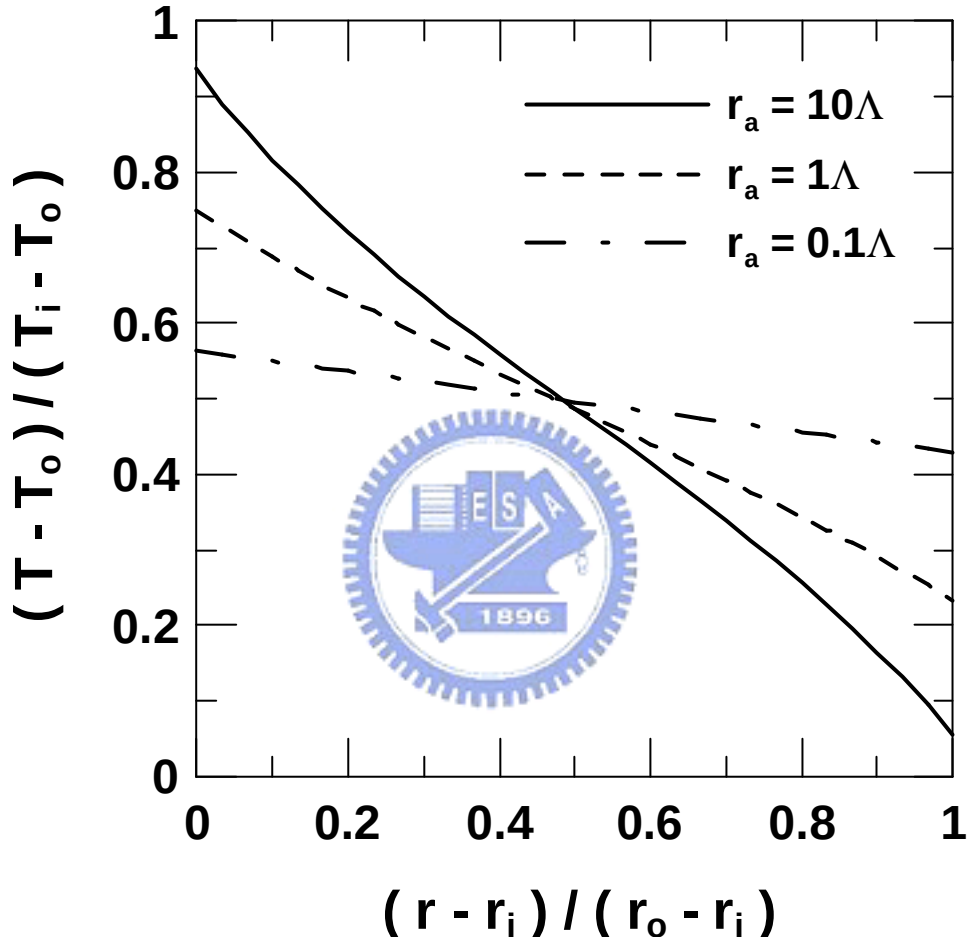

Fig. 4.4 The effect of tube thickness on the radial temperature distributions of diamond tube in the middle plane ($z = 0.5L_a$) with the inner radius $r_i = 10\ mm$ and the tube height $L_a = 10L$.

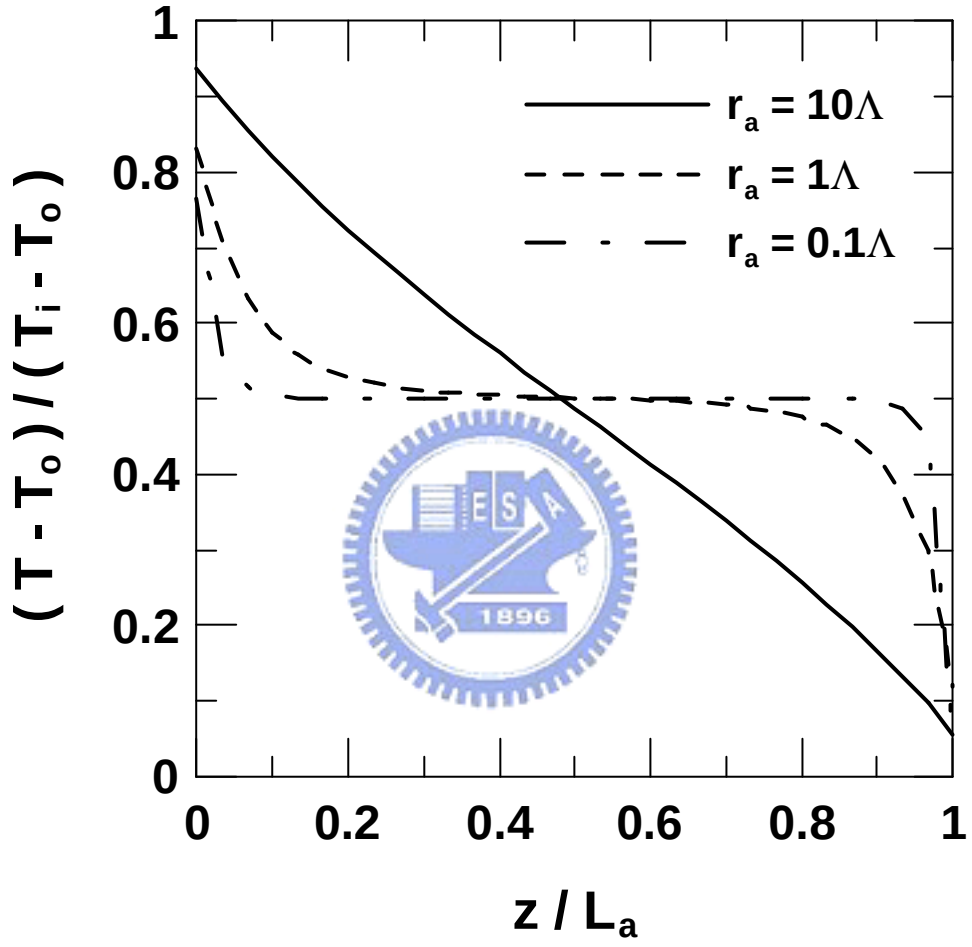

Fig. 4.5 The effect of tube thickness on the axial temperature distributions of diamond tube at the location $r = 0.5(r_i + r_o)$ with the inner radius $r_i = 10\ mm$ and the tube height $L_a = 10L$.

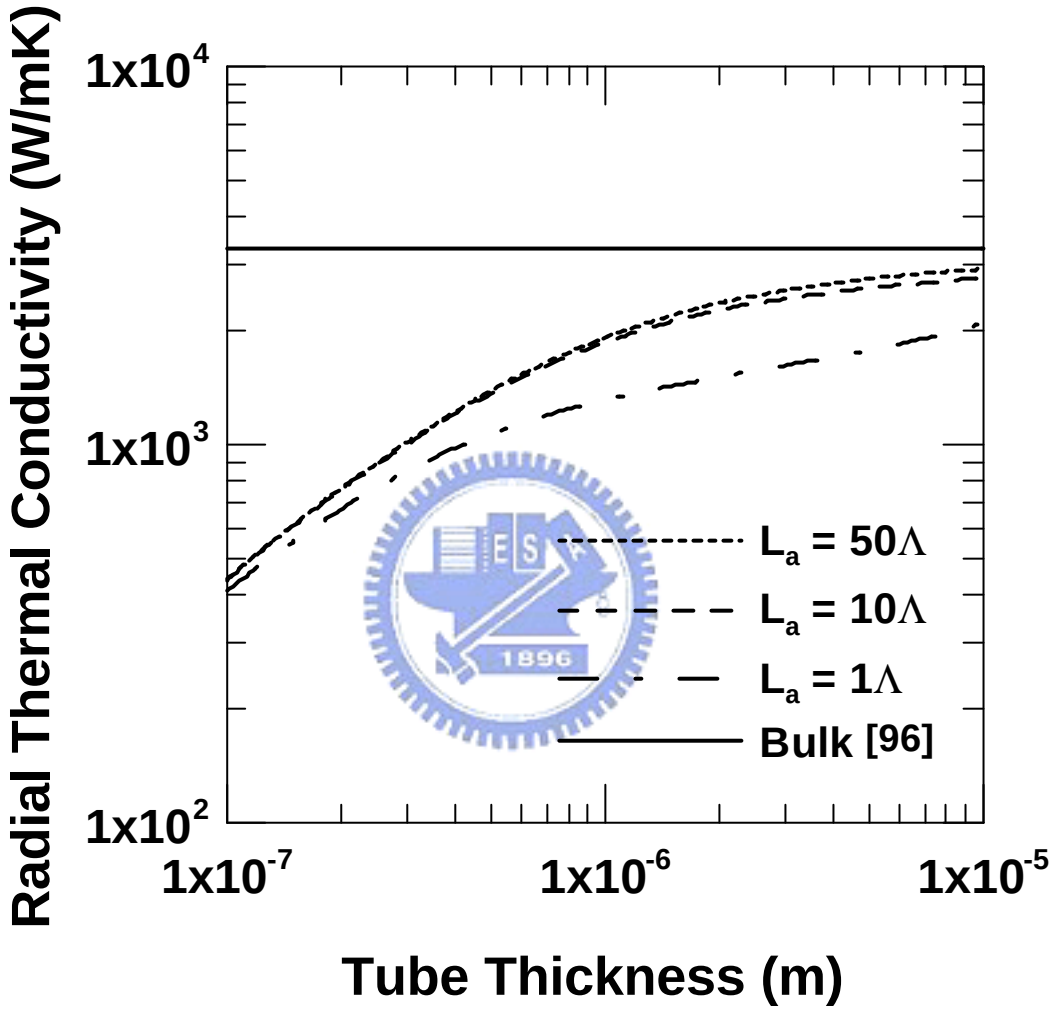

Fig. 4.6 Size effects on the radial thermal conductivity of diamond tube under different tube heights.

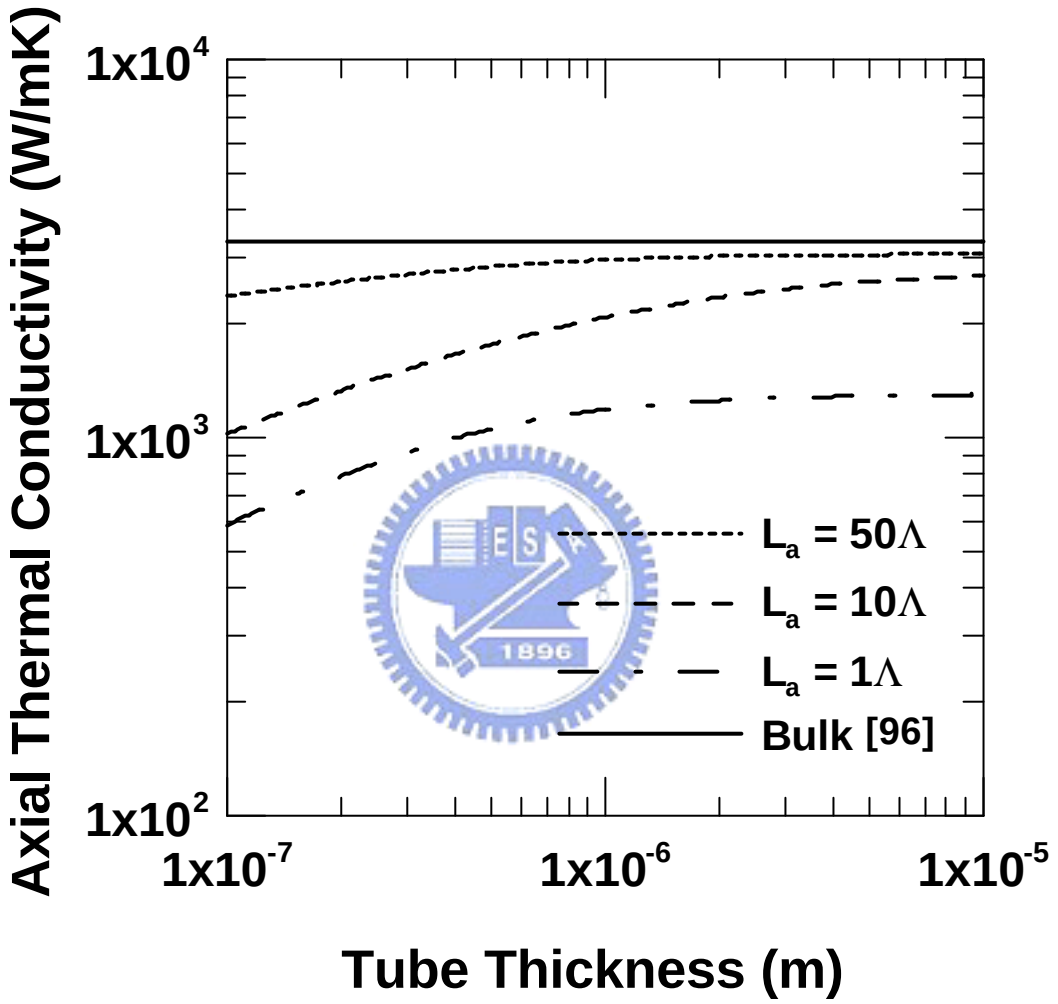

Fig. 4.7 Size effects on the axial thermal conductivity of diamond tube under different tube heights.

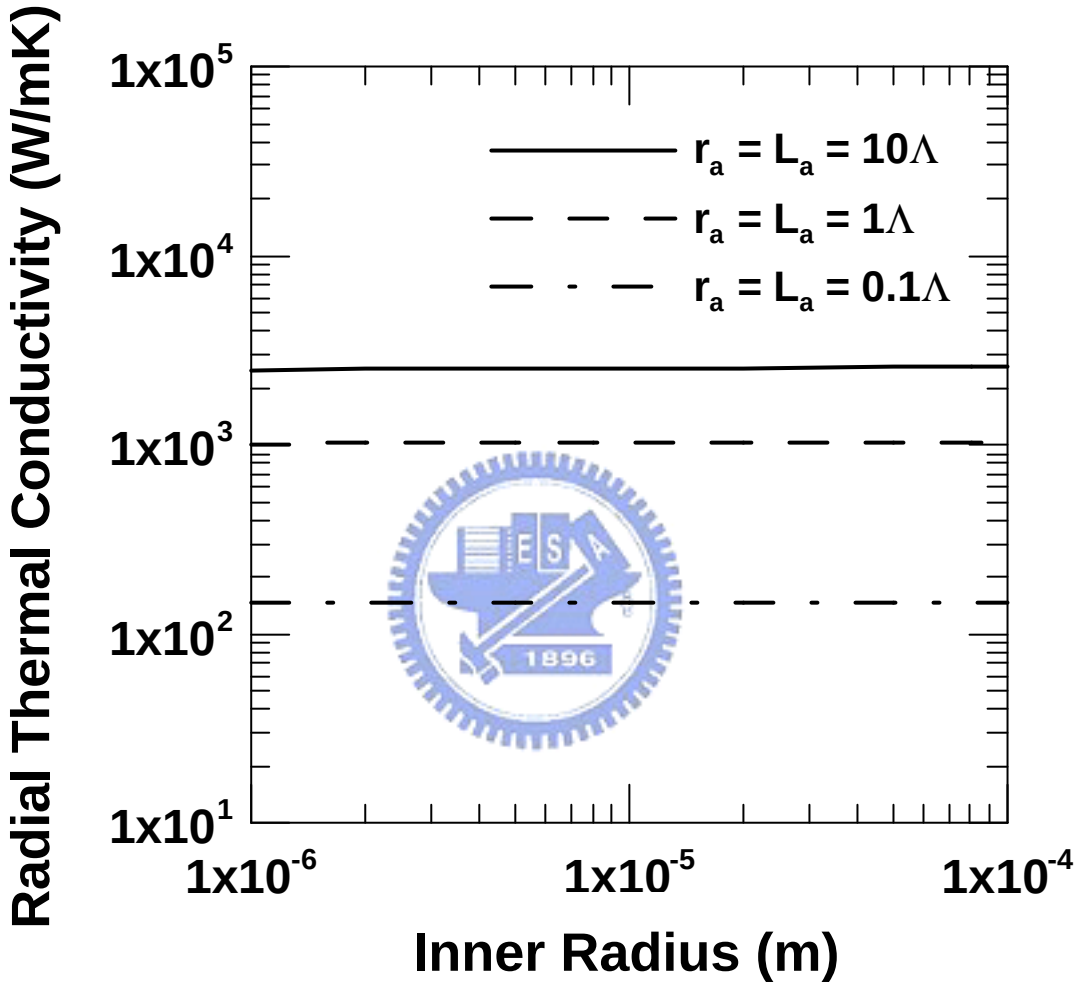

Fig. 4.8 The effect of curvature on the radial thermal conductivity of diamond tube for different tube heights.

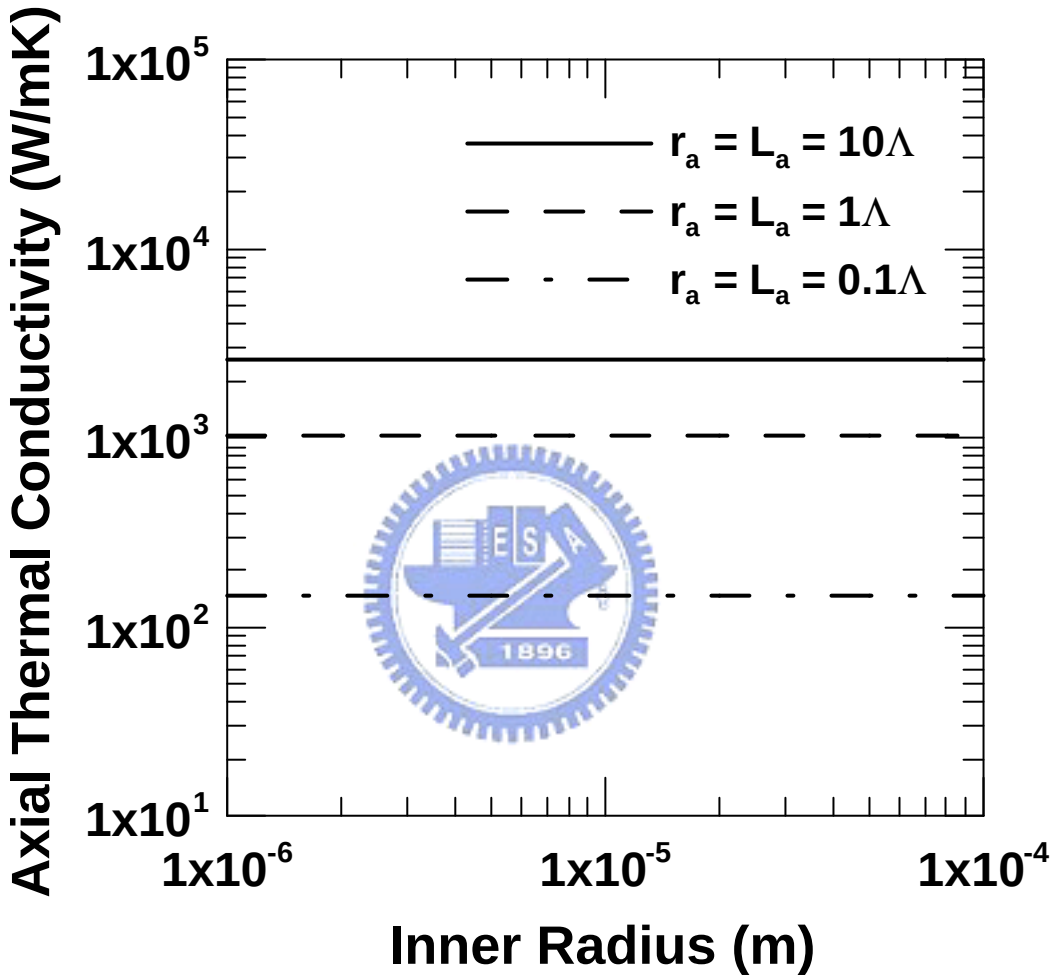

Fig. 4.9 The effect of curvature on the axial thermal conductivity of diamond tube for different tube heights.

5. SIZE EFFECTS ON THE PERFORMANCE OF THERMOELECTRIC MICRO COOLERS

By utilizing the Peltier effect, heat will be absorbed on the cold side and rejected to the heat sink when an electric current is passed through a thermoelectric material, thus providing a refrigeration capability. Conversely, an imposed temperature gradient will result in a voltage so a power generator is created. This aspect is widely utilized in deep space applications. A radioactive material is used as the heat source in the radioactive thermoelectric generators to provide the electricity [88]. The advantages of thermoelectric devices include compactness, quietness, localized heating or cooling and environmentally friendly. Applications of thermoelectric refrigeration include cooling of CCDs (charged coupled devices), laser diodes, infrared detectors, computer processor chips and biological specimens [88]. Low-dimensional thermoelectric materials, such as nanodots (0D), nanowires (1D) and thin films (2D) are of great potential due to the dramatic reduction in thermal conductivity. In this chapter, EPRT and DMM are utilized to calculate the thermal conductivity of thin film superlattices, nano wire superlattices and nano tube superlattices. Size effects on the performance of thermoelectric micro coolers will be examined in detail.

5.1 Thin Film Supperlattices

A thermoelectric micro cooler that is consisted of thin film superlattices is under consideration. The transmission electron microscopy image of thin film superlattices is shown in Fig. 5.1 and the schematic diagram is illustrated in Fig. 5.2. The thickness of layer 1 is L_1, the thickness of layer 2 is L_2, and the total thickness is L. The

temperature of bottom surface ($x=0$) is T_H. Meanwhile, the temperature of top surface ($x=L$) is maintained at T_C.

Utilizing EPRT to analyze heat transfer in thin film superlattices and the governing equations can be expressed as

$$m\frac{\partial I_k}{\partial x}=\frac{\frac{1}{2}\int_{-1}^{1} I_k dm - I_k}{t_{R,k}v_k},\quad k=1,2, \tag{5-1}$$

where the subscript indices $k=1$ and 2 represent layer 1 and layer 2, respectively. The boundary conditions are

$$I_1(x=0)=I_1^0(T=T_H), \tag{5-2a}$$

$$I_2(x=L)=I_2^0(T=T_C), \tag{5-2b}$$

where the superscript 0 means that phonons are in the state of thermal equilibrium. The conservation of energy is used to describe the interface conditions.

$$\int_{2p} I_1^- m_1 dm_1 = R_{12}\int_{2p} I_1^+ m_1 dm_1 + a_{21}\int_{2p} I_2^- m_2 dm_2, \tag{5-3a}$$

$$\int_{2p} I_2^+ m_2 dm_2 = R_{21}\int_{2p} I_2^- m_2 dm_2 + a_{12}\int_{2p} I_1^+ m_1 dm_1, \tag{5-3b}$$

$$\int_{2p} I_1^+ m_1 dm_1 = R_{12}\int_{2p} I_1^- m_1 dm_1 + a_{21}\int_{2p} I_2^+ m_2 dm_2, \tag{5-3c}$$

$$\int_{2p} I_2^- m_2 dm_2 = R_{21}\int_{2p} I_2^+ m_2 dm_2 + a_{12}\int_{2p} I_1^- m_1 dm_1, \tag{5-3d}$$

where a_{ij} and R_{ij} represent the transmissivity and the reflectivity, respectively.

Since the governing equations and interface conditions are integro-differential equations, the discrete ordinate method is employed to solve the governing system. The S_2 scheme is selected to deal with the governing system in this study. To conduct a numerical simulation, the finite difference method is utilized to approximate the differential terms in the governing system. Forward and backward

differences are used in the negative and positive x-direction, respectively. The governing system is then turned into a set of simultaneous algebraic equations. Thus, an iterative procedure is performed in this study and the convergence criterion is that the relative error for temperature is less than 10^{-4}.

5.2 Nano Tube Supperlattices and Nano Wire Superlattices

This study considers a two-dimensional hollow cylinder of inner radius R_i, outer radius R_o and height L, as illustrated in Fig. 5.3. The tube is consisted of periodically permuted layer 1 and layer 2. The thickness of layer 1 and the thickness of layer 2 are L_1 and L_2, respectively. For convenience in the subsequent analysis, the medium is assumed to be gray. The EPRT can be expressed as

$$\frac{m}{r}\left[\frac{\partial(rI_j)}{\partial r}\right]-\frac{1}{r}\left[\frac{\partial(hI_j)}{\partial f}\right]+y\left[\frac{\partial I_j}{\partial z}\right]=\frac{\frac{1}{4p}\int_{4p} I_j\,d\Omega - I_j}{v_j t_{R,j}},\quad j=1,2, \tag{5-4}$$

where the subscript indices $j=1$ and 2 represent layer 1 and layer 2, respectively. Consider the temperatures of the top surface ($z=L$) and the inner surface ($r=R_i$) are maintained at $T=T_i$. The temperatures of other two surfaces (bottom and outer surfaces) are $T=T_o$, where $T_i>T_o$. The boundary conditions can be expressed as

$$I_j(r=R_i)=I_j^0(T_i),\quad j=1,2, \tag{5-5a}$$

$$I_j(r=R_o)=I_j^0(T_o),\quad j=1,2, \tag{5-5b}$$

$$I_1(z=0)=I_1^0(T_o), \tag{5-5c}$$

$$I_2(z=L)=I_2^0(T_i). \tag{5-5d}$$

The interface conditions are the same with Eqs. (5-3a), (5-3b), (5-3c) and (5-3d).

Nano wires and nano wire superlattices, as shown in Fig. 5.4, are potential

materials for engineering applications, especially in thermoelectrics. The formulation of microscale heat transfer in nano wire superlattices is similar to that in nano tube superlattices. In this study, a nano wire superlattice of radius R and length L is under consideration. The schematic diagram is illustrated in Fig. 5.5. The thickness of layer 1 is L_1 and the thickness of layer 2 is L_2. The governing equations of microscale heat transfer in the nano wire superlattice are the same with those in the nano tube superlattice. Moreover, the boundary conditions in top, bottom and outer surface are also identical with those in the nano tube superlattice. The only difference between the nano wire superlattice and the nano tube superlattice is that the nano wire superlattice is solid not hollow. To specify the boundary condition in the z-axis, the axisymmetric assumption was made and it can be expressed as

$$I_j(r, z, m, x) = I_j(r, z, -m, x), \quad j = 1, 2, \tag{5.6}$$

where the subscript indices $j = 1$ and 2 represent layer 1 and layer 2, respectively.

Similar to the strategy of solving microscale heat transfer in thin film superlattices, the S_2 scheme is selected to deal with the microscale heat transfer in nano wire superlattices and nano tube superlattices. Backward and forward difference approximations are utilized in positive and negative directions, respectively. The numerical method is the same as used in chapter 4. To solve the simultaneous governing equations, an iterative procedure is performed in this study and that the relative error for temperature is less than 10^{-4} is the convergence criterion.

5.3 Results and Discussion

The comparison between numerical calculations and experiments was made in Fig. 5.6. GaAs/AlAs, Si/Ge and Bi_2Te_3/Sb_2Te_3 superlattices are chosen as examples and the results are shown in Figs. 5.6(a), 5.6(b) and 5.6(c), respectively. From Fig.

5.6(a), it can be seen that the present results match Chen's study [52] and agree with the experimental data measured by Capinski and Maris [53]. Similarly, Fig. 5.6(b) tells that the numerical calculations of Si/Ge are in agreement with Chen's study [52]. In addition, Fig. 5.6(b) reveals that the numerical calculations match the experiments conducted by Lee et al. [73] when the period thickness is less than 7 nm. However, the measured thermal conductivity of Si/Ge is lower than the numerical simulations by about one order of magnitude when the period thickness is greater than 13 nm. Lee et al. argued that the relatively poor crystal quality of long-period superlattices should be responsible for such low thermal conductivity. The comparison between numerical simulations and experiments for Bi_2Te_3/Sb_2Te_3 superlattices, the well-known thermoelectric material, was made in Fig. 5.6(c). The discrepancy between the numerical calculations and experiments is less than 10% when the period thickness is less than 5 nm. Although the discrepancy is higher for larger period thickness case, the numerical calculations and experiments have the same order of magnitude. It can be concluded that EPRT with DMM is adequate to describe the microscale heat transfer behavior in practical engineering applications.

Up to date, Bi_2Te_3/Sb_2Te_3 is the most efficiency thermoelectric material for room-temperature applications [97]. Thus, it is selected to demonstrate the following numerical calculations.

Fig.5.7 shows the effect of thin film superlattices thickness on the thermal conductivity. Three different periods are selected to demonstrate the size effect on the thermal conductivity. It can be seen that the thermal conductivity of Bi_2Te_3/Sb_2Te_3 thin film superlattices decreases with decreasing film thickness. On the other hand, the thermal conductivity approaches its bulk value as superlattices getting thick.

In practical engineering applications, how to produce a product as compact as

possible is a very important issue. For a restricted space, it is desired to design a miniaturized thermoelectric cooler with high performance. As mentioned before, reducing the thermal conductivity is a good way to increase the performance of a thermoelectric cooler. Fig. 5.8 illustrates how the number of periods affects the thermal conductivity for a fixed total film thickness, L. It is noticed that the thermal conductivity decreases with increasing number of periods. For a fixed total film thickness, increasing number of periods means decreasing layer thickness of each layer and increasing number of interfaces. As discussed in chapter 3, the thermal conductivity decreases as the film thickness decreases. Thus, to decrease the thermal conductivity of thin film superlattices for a restricted space, it is recommended to increase the number of periods. However, for $L = 10$ nm, the thermal conductivity of Bi_2Te_3/Sb_2Te_3 thin film superlattices approaches a constant value as number of periods increase. In this case, the layer thickness is small compared to the phonon mean free path, which is about 5 Å Although increasing number of periods will decrease the thermal conductivity of Bi_2Te_3/Sb_2Te_3 thin film superlattices for a fixed total film thickness, it has no further significant influence when the layer thickness is small compared to the phonon mean free path of materials.

Fig. 5.9 shows the effect of thin film superlattices thickness on the figure of merit, ZT. It is obvious that the figure of merit increases as film thickness decreases. From the definition of the figure of merit, $ZT = \frac{S^2 \sigma_e T}{k}$, it is easy to find out that the figure of merit increases as the thermal conductivity decreases. Since the thermal conductivity decreases as film thickness decreases, the figure of merit increases with decreasing film thickness. The reduction of film thickness is helpful in improving the performance of the thin film superlattices thermoelectric cooler. The size of the thin film superlattices has a significant influence on the figure of merit when the film

thickness is comparable to the phonon mean free path of materials. However, this effect is not obvious when the film thickness is getting large. Fig. 5.9 reveals that the figure of merit approaches a constant value as film thickness increases.

Fig. 5.10 illustrates the influence of the number of periods on the figure of merit. For a fixed film thickness, increasing the number of periods results in increasing ZT. It indicates that increasing the number of periods for a fixed film thickness will improve the performance of a thin film superlattices thermoelectric cooler.

From the above discussion, it can be concluded that size effects have significant influence on the performance of thermoelectric micro coolers. Thin film superlattices are two-dimensional thermoelectric materials since the size of one of their dimensions is small compared to the others. The thermal conductivity in the direction which size is small compared to the others is reduced owing to size effects. Thus, reducing dimensionality further can be considered as an approach for decreasing the thermal conductivity of thermoelectric materials and then increasing their performance. Nano wire superlattices, which are one-dimensional materials, are considered as potential thermoelectric materials.

In practical engineering applications, the axial thermal conductivity of nano wire and nano tube superlattices is a very important parameter for designing thermoelectric coolers. In the following discussion, it will only discuss the axial thermal conductivity of nano wires and nano tubes.

Fig. 5.11 displays the effect of number of periods on the thermal conductivity of nano tube superlattices. Each layer of the superlattices has the same thickness and it is 1 nm. The inner radius and outer radius of the nano tube superlattices are 10 and 11 nm, respectively. The effect of number of periods on the thermal conductivity of nano tube superlattices is not obvious. Increasing number of periods does not decrease the

thermal conductivity of nano tube superlattices. The most important parameter relative to thermal conductivity is the layer thickness. Once the thickness of every individual layer is determined, the thermal conductivity of nano tube superlattices will not vary with increasing number of periods. It is convenient for numerical simulations. We just need to calculate the one-period nano tube superlattices case and it is timesaving.

Fig. 5.12 depicts the effect of tube thickness on the thermal conductivity of nano tube superlattices. The layer thickness of the tube, $L_1 = L_2$, is 1 nm and its inner radius is 10 nm. Here the tube thickness is defined as $R_o - R_i$. From Fig. 5.12, it is noticed that the thermal conductivity decreases as the tube thickness decreases. This is very interesting that not only reducing the size in axial direction but also reducing the size in radial direction will reduce the axial thermal conductivity. On the other hand, the thermal conductivity does not increase with increasing tube thickness when the tube thickness is greater than 50 nm. Since the layer thickness is 1 nm, which is less than the phonon mean free path, phonon transport is confined due to size effects in the axial direction. The axial thermal conductivity of the tube approaches a constant value, 0.35 W/mK, and it is less than the bulk value, 0.6 W/mK.

Fig. 5.13 shows the effect of layer thickness on the thermal conductivity of nano tube superlattices. The inner and outer radius of the tube is 1 and 101 nm, respectively. The axial thermal conductivity decreases as the layer thickness decreases. The results of numerical simulations again demonstrate the influence of size effects on the thermal conductivity. Reducing layer thickness of nano tube superlattices is an effective way to decrease the axial thermal conductivity.

Fig. 5.14 illustrates the curvature effect on the thermal conductivity of nano tube superlattices. Three values of tube thickness, 1 nm, 10 nm and 100 nm, are selected to

show how does the curvature affect the axial thermal conductivity of nano tube superlattices. The layer thickness is 1 nm in all the three cases. The thermal conductivity increases with decreasing inner radius. It indicates that increasing curvature results in increasing axial thermal conductivity. However, this phenomenon is not obvious. The thermal conductivity of a tube with 1 nm inner radius is merely 1.6 % greater than that of a tube with 1000 nm inner radius for 1nm tube thickness. Similarly, for 10 nm and 100 nm tube thickness, the discrepancy is 0.03% and 0.3%, respectively. Curvature just slightly affects the axial thermal conductivity. Moreover, the curvature effect is less important when the tube thickness is getting large.

Fig. 5.15 reveals the size effect on the thermal conductivity of nano wire superlattices. The axial thermal conductivity decreases as the radius decreases. Additionally, reducing the layer thickness further reduces the axial thermal conductivity. To enhance the performance of nano wire superlattices thermoelectric micro coolers, it is necessary to decrease the axial thermal conductivity. Reducing the radius and layer thickness of the nano wire superlattices will be helpful to design a high performance thermoelectric device.

Fig. 5.16 displays the comparison of thermal conductivities of thin film, nano wire and nano tube superlattices. The radius of the nano wire is 101 nm. The outer and inner radius of the nano tube is 101 nm and 100 nm, respectively. All the three cases show the same behavior that decreasing the layer thickness will reduce the thermal conductivity. Furthermore, it is easy to observe that $k_{nano-tube} > k_{nano-wire} > k_{thin-film}$ when they have the same layer thickness. The restriction of boundary should be responsible for reducing thermal conductivity. Low dimensionality enhances the boundary scattering, so nano tubes and nano wires have lower thermal conductivities. Thus, nano tube and nano wire superlattices are

potential thermoelectric materials.

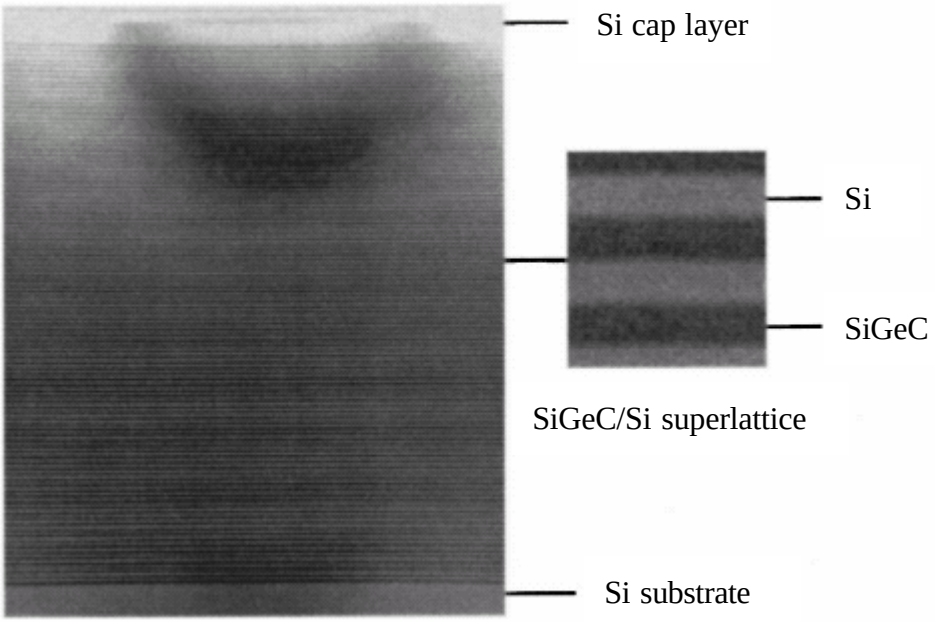

Fig. 5.1 Cross sectional transmission electron microscopy image of the MBE grown SiGeC/Si superlattice cooler sample [98].

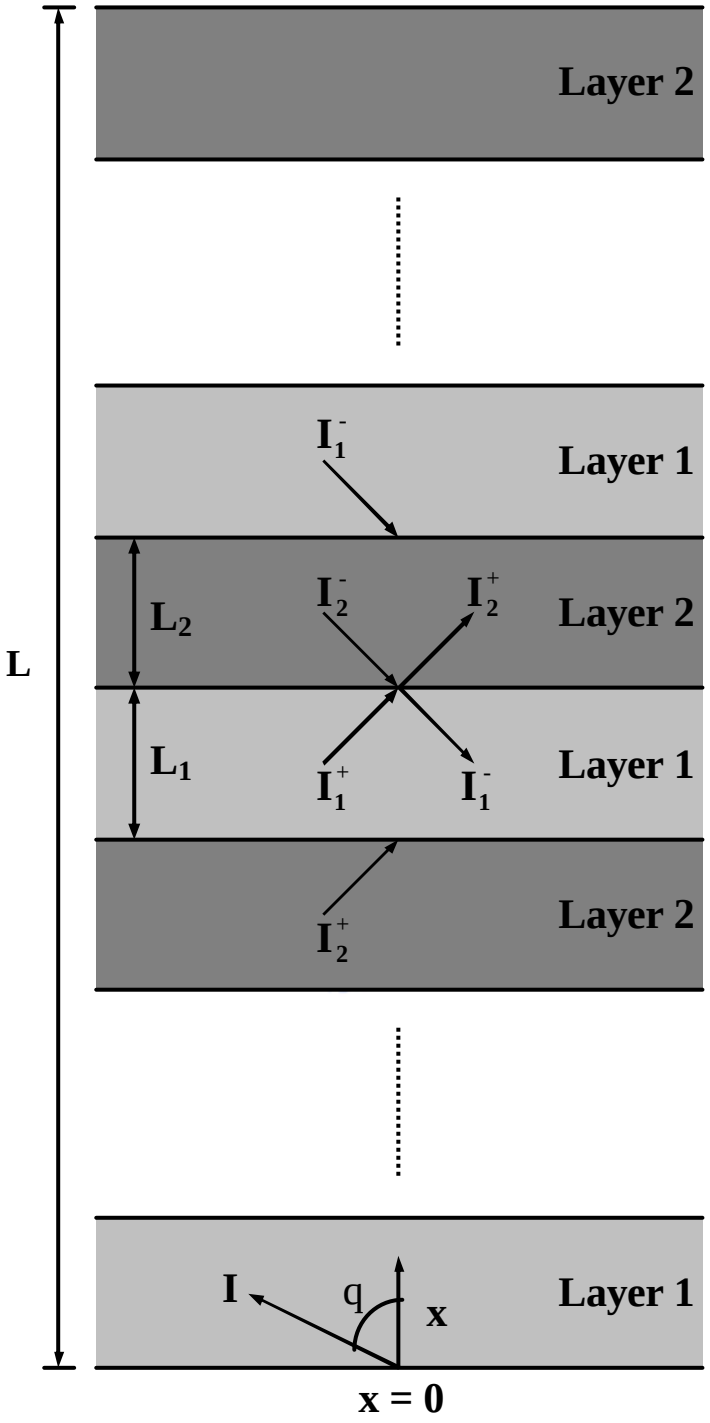

Fig. 5.2 Schematic diagram of thin film superlattices.

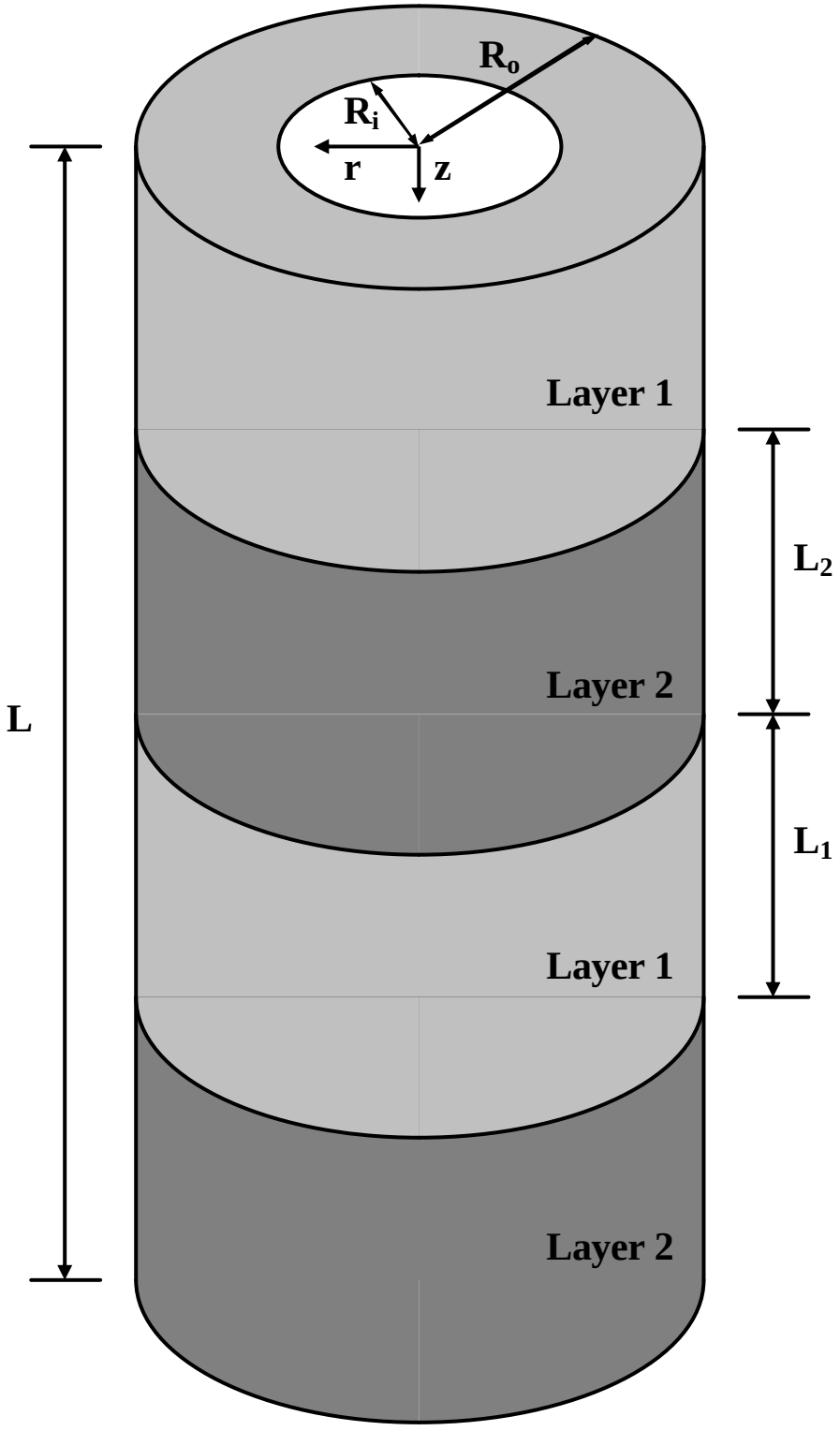

Fig. 5.3 Schematic diagram of nano tube superlattices.

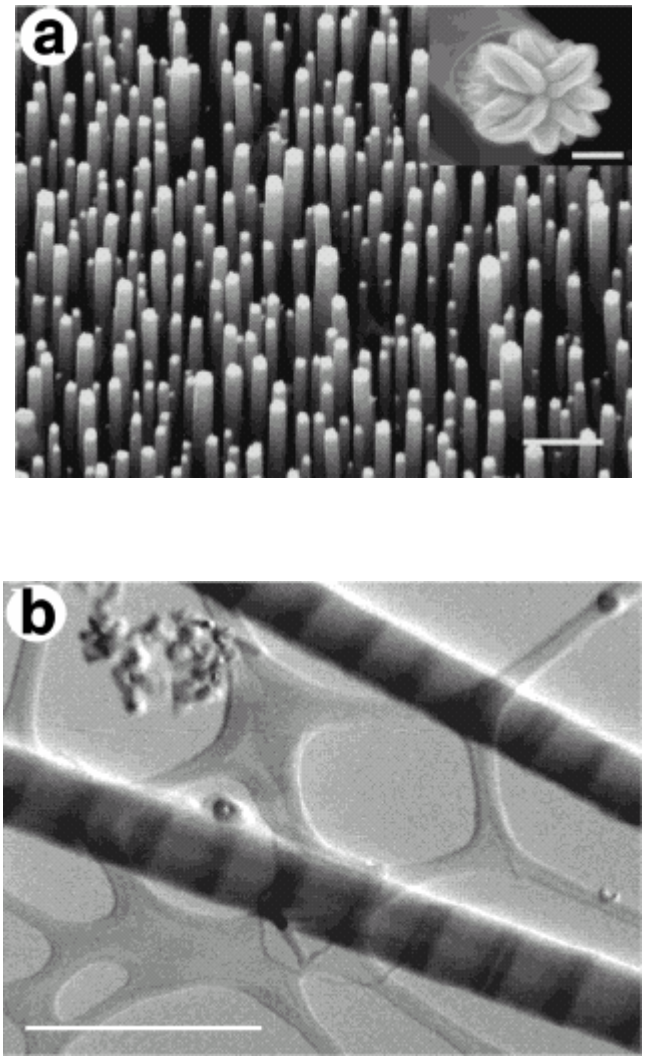

Fig. 5.4 SEM image of the heterostructured nanowire array on Si(111) substrate. The scale bar is 1 μm. The inset shows the tip of one nanowire. The scale bar is 100 nm. (b)STEM image of two nanowires in bright field mode. The scale bar is 500 nm. [99]

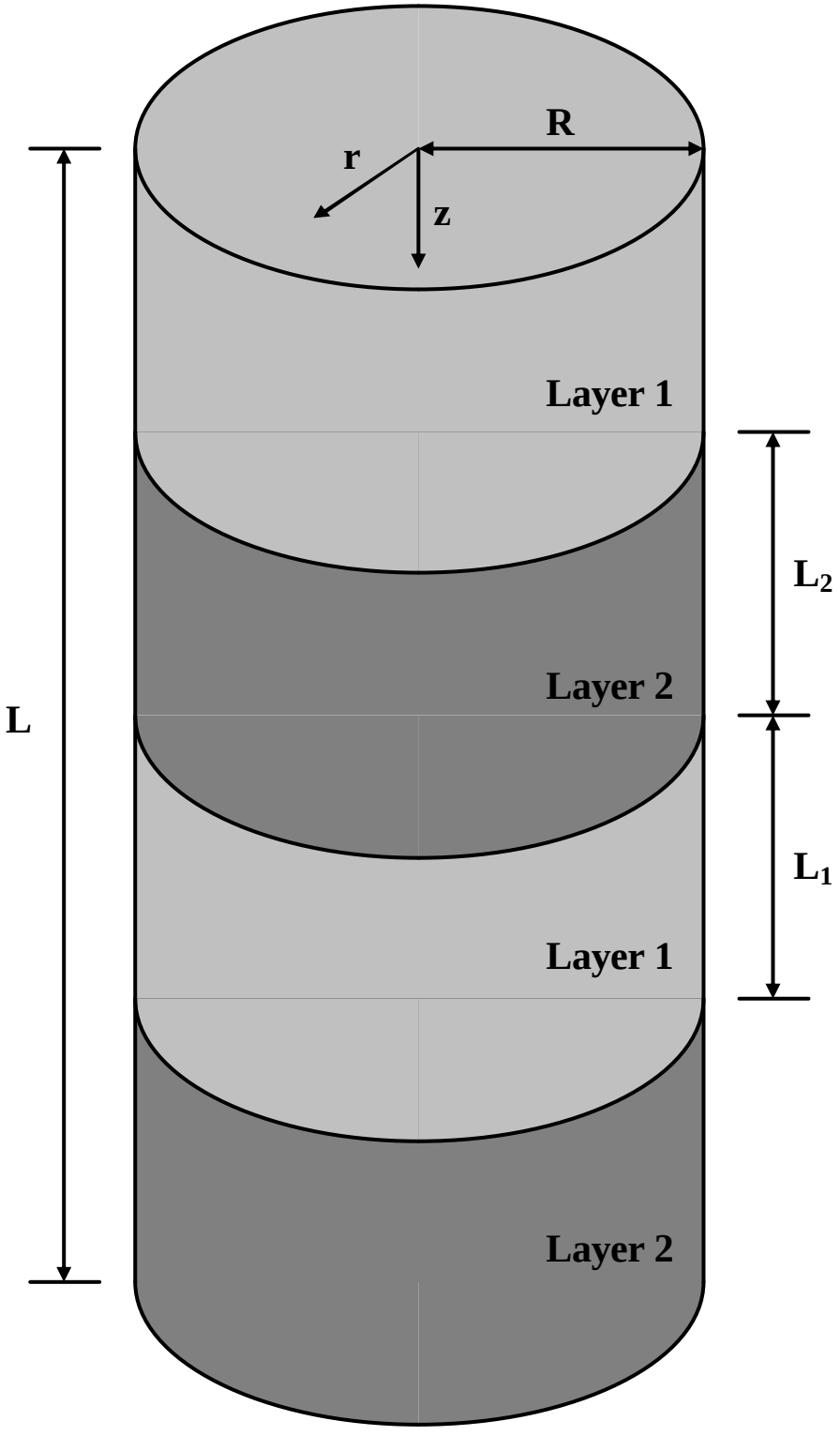

Fig. 5.5 Schematic diagram of nano wire superlattices.

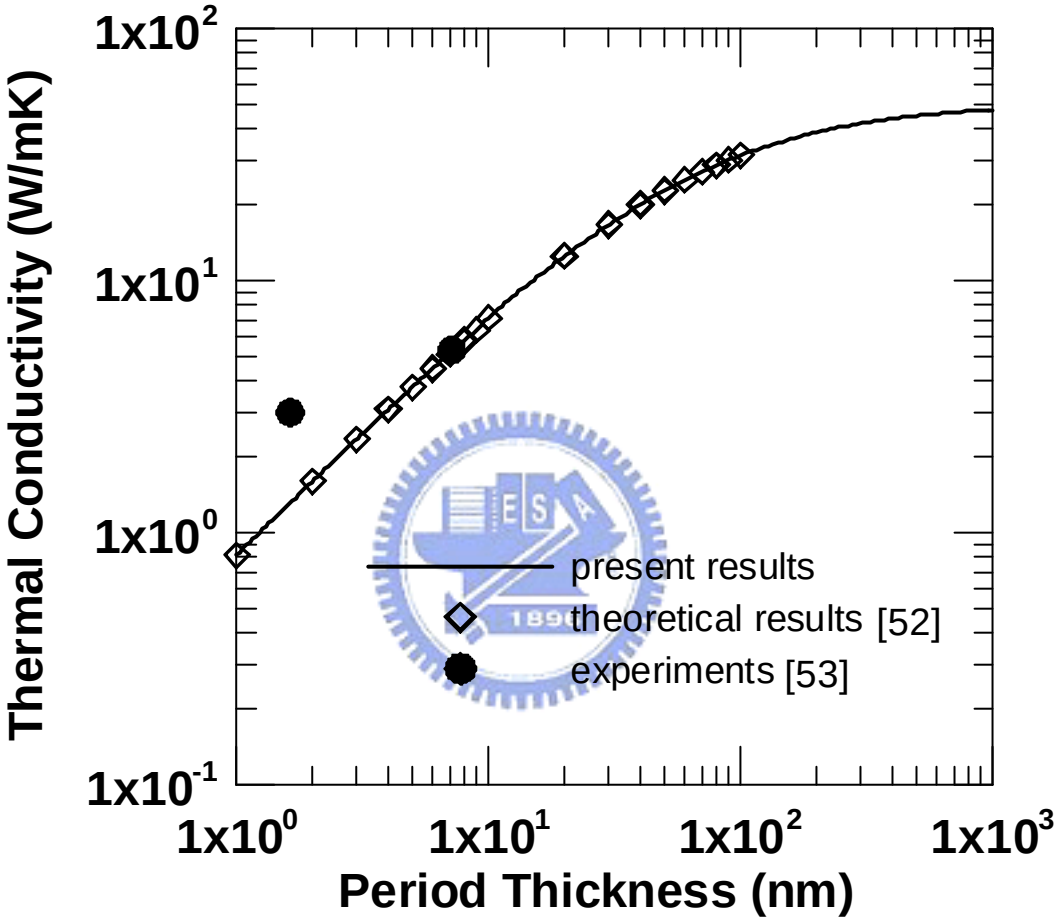

Fig. 5.6 (a) Comparison of numerical calculations and experiments for GaAs/AlAs superlattices.

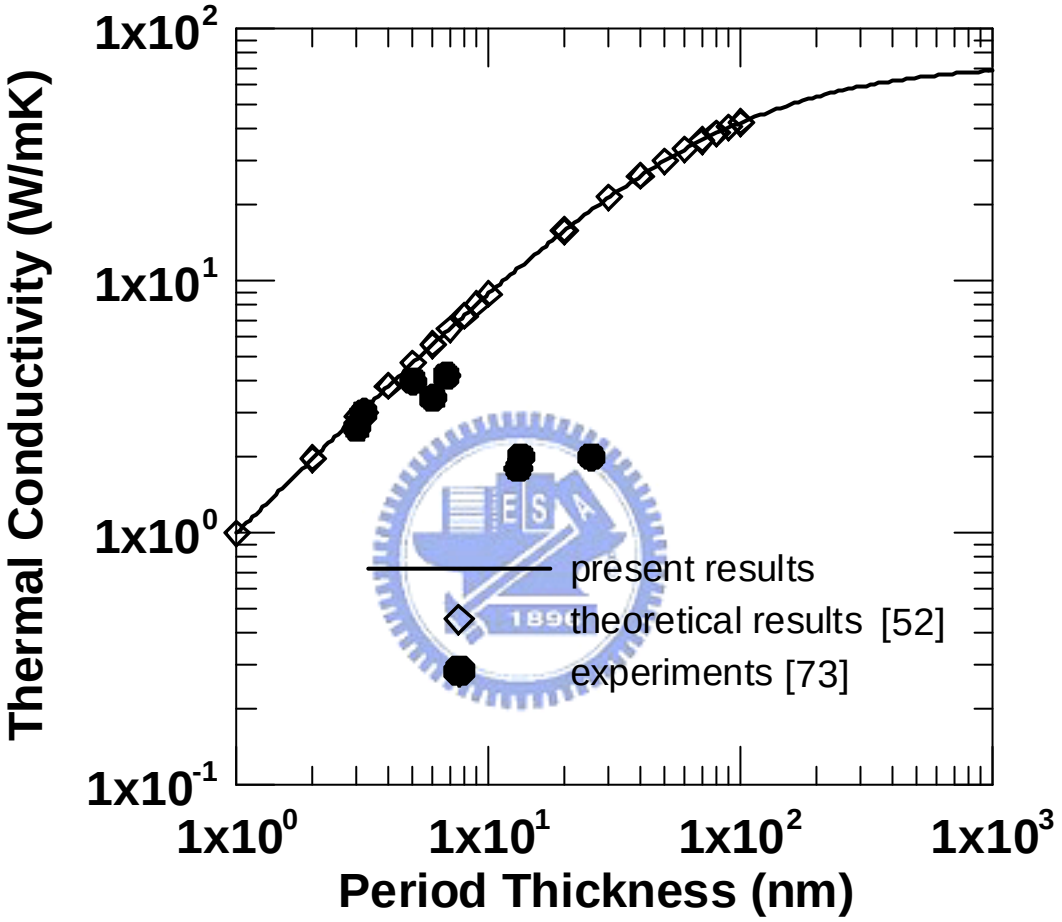

Fig. 5.6 (b) Comparison of numerical calculations and experiments for Si/Ge superlattices.

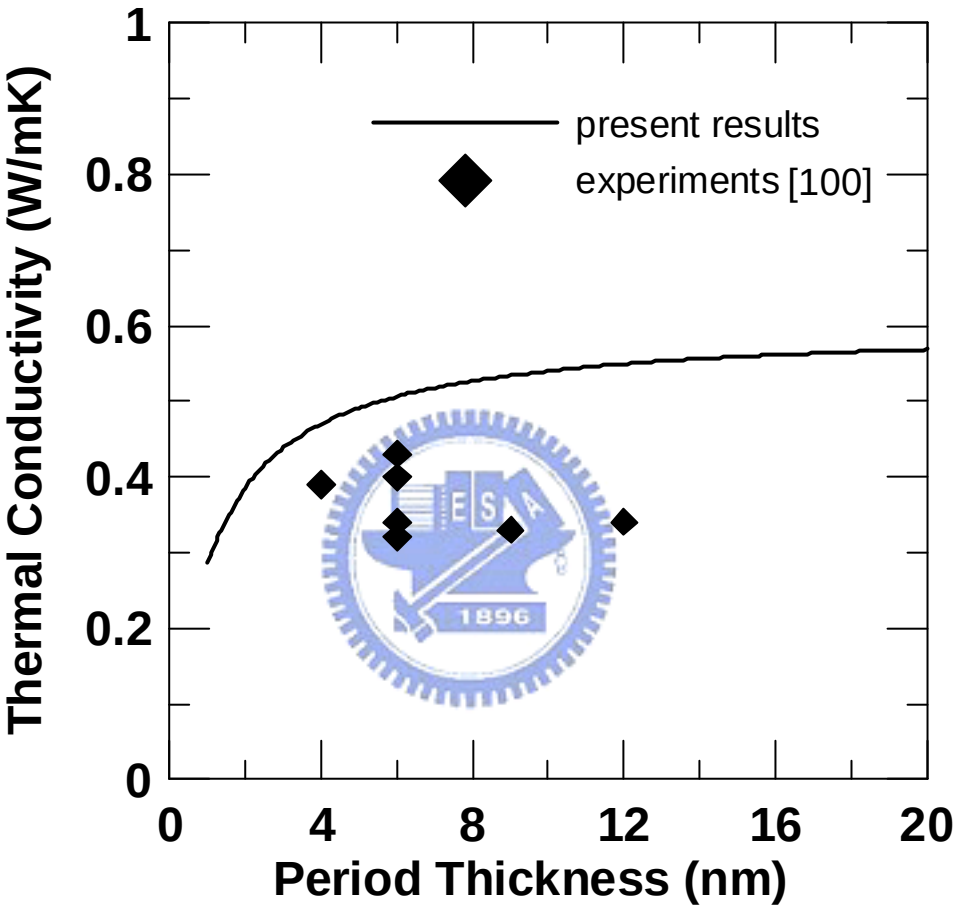

Fig. 5.6 (c) Comparison of numerical calculations and experiments for Bi_2Te_3/Sb_2Te_3 superlattices.

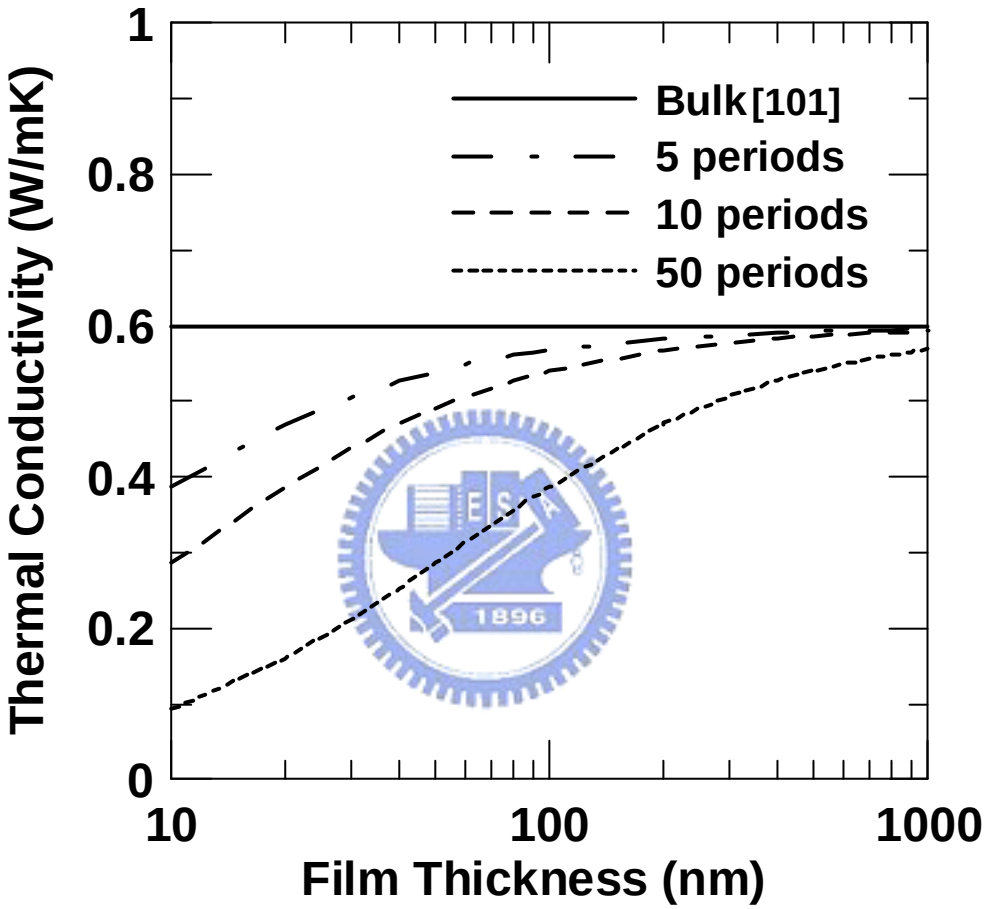

Fig. 5.7 The effect of film thickness on the thermal conductivity of Bi_2Te_3/Sb_2Te_3 thin film superlattices.

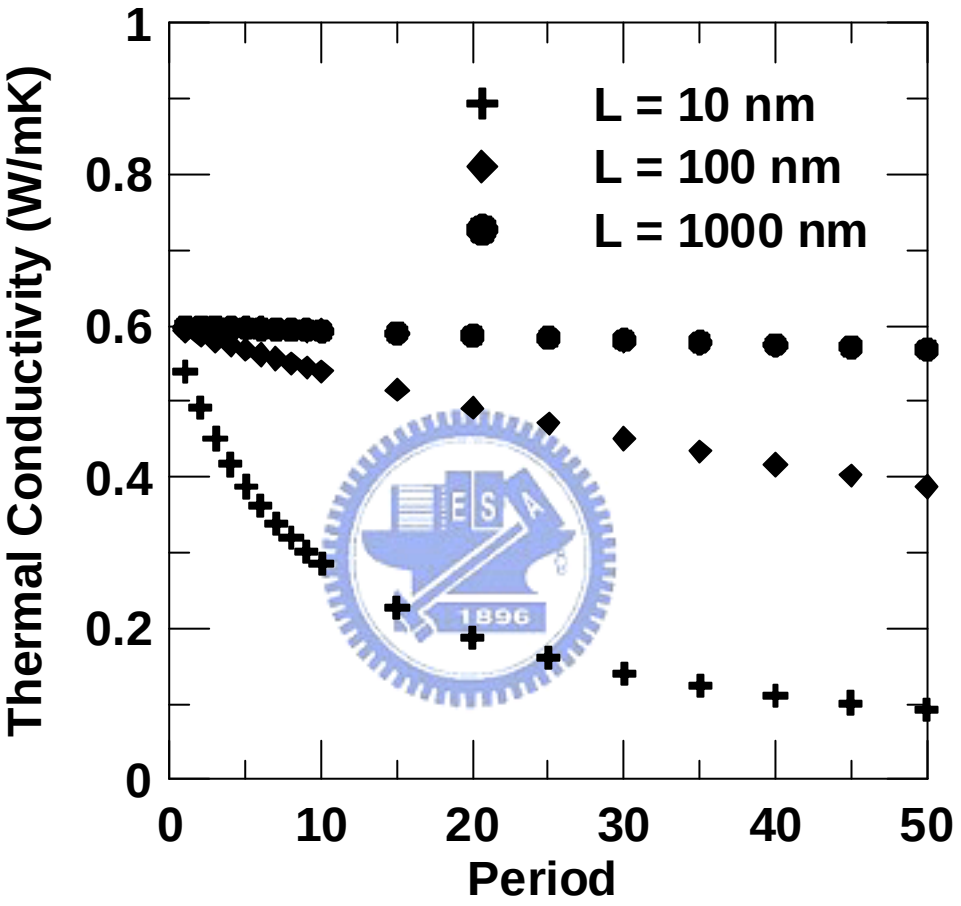

Fig. 5.8 The effect of the number of periods on the thermal conductivity of Bi_2Te_3/Sb_2Te_3 thin film superlattices for a fixed total film thickness: (a) $L = 10$ nm, (b) $L = 100$ nm and (c) $L = 1000$ nm.

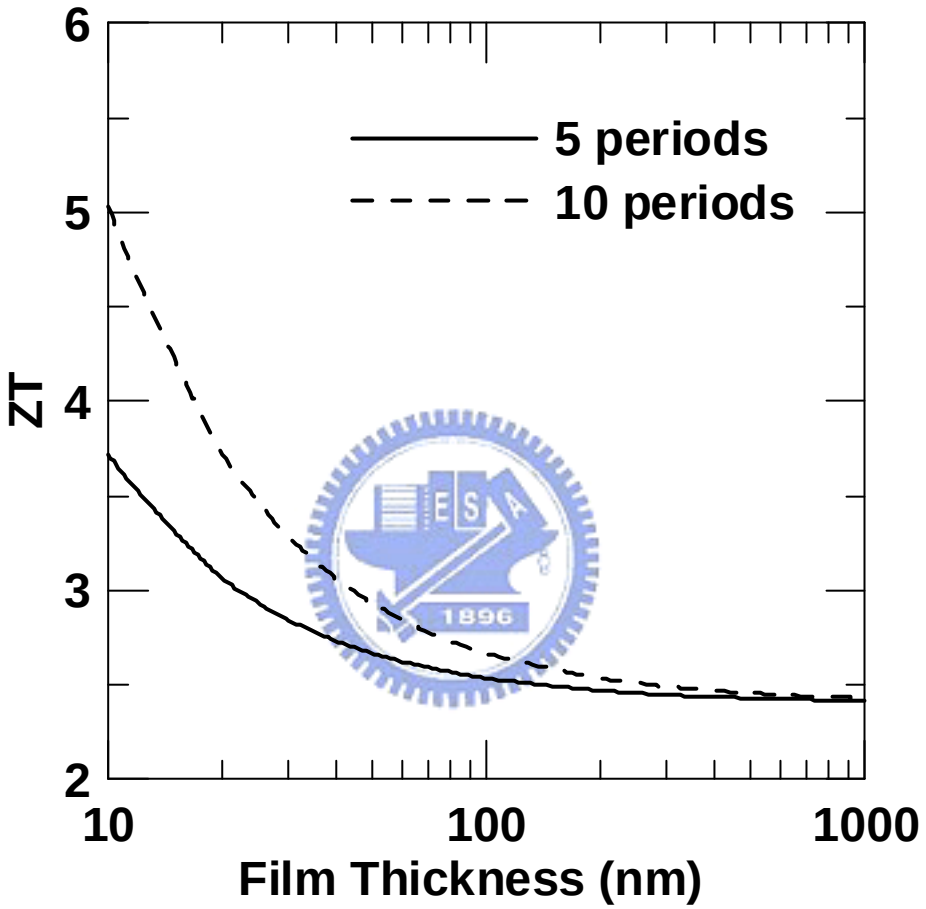

Fig. 5.9 The effect of film thickness on the figure of merit of Bi_2Te_3/Sb_2Te_3 thin film superlattices.

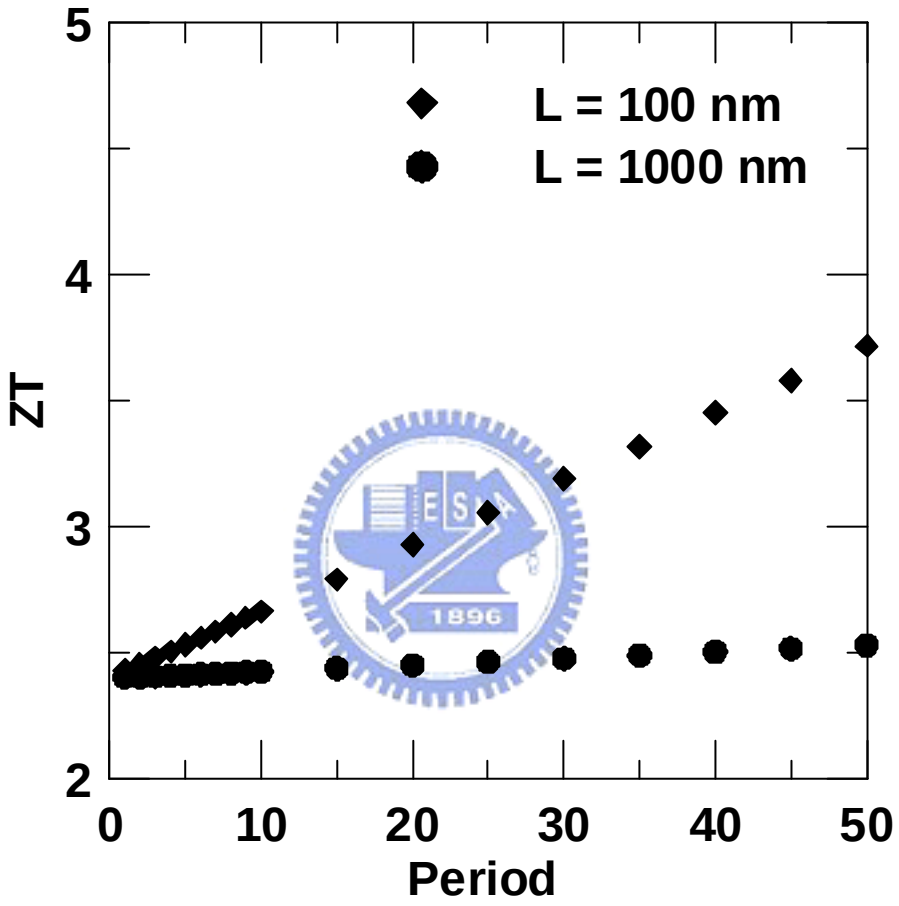

Fig. 5.10 The effect of the number of periods on the figure of merit of Bi_2Te_3/Sb_2Te_3 thin film superlattices for a fixed total film thickness: (a) $L = 100\,\text{nm}$ and (b) $L = 1000\,\text{nm}$.

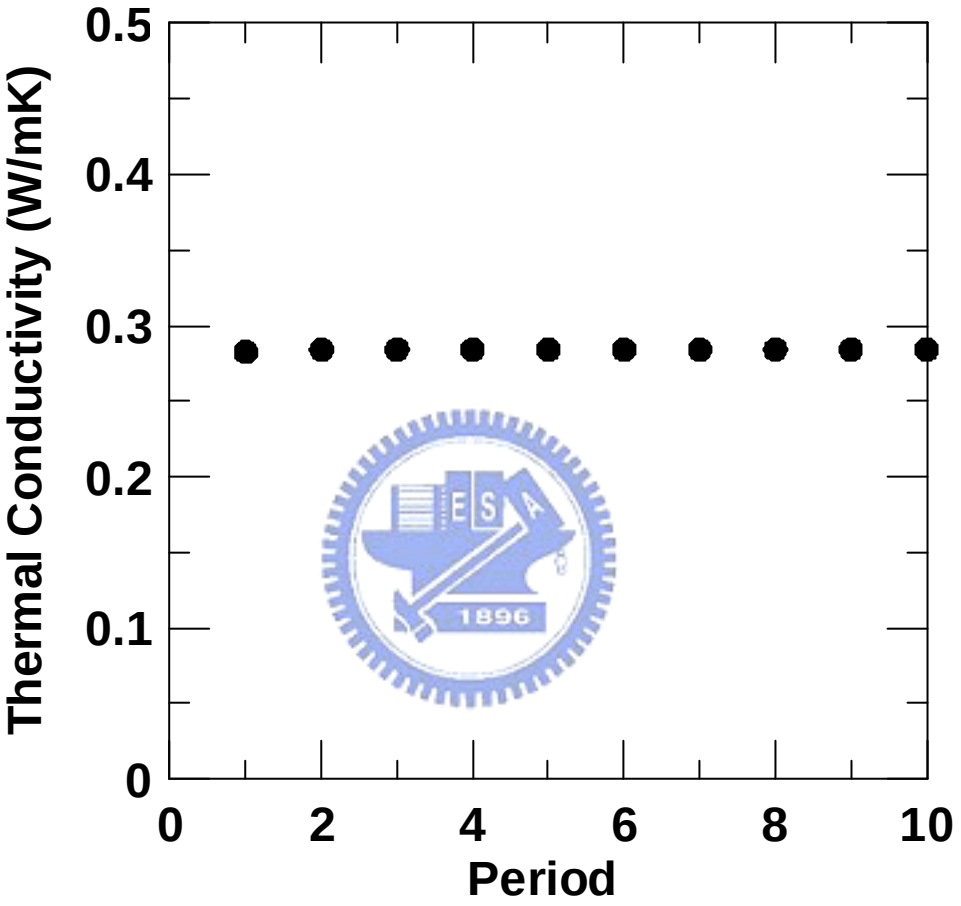

Fig. 5.11 The effect of number of periods on the thermal conductivity of Bi_2Te_3/Sb_2Te_3 nano tube superlattices.

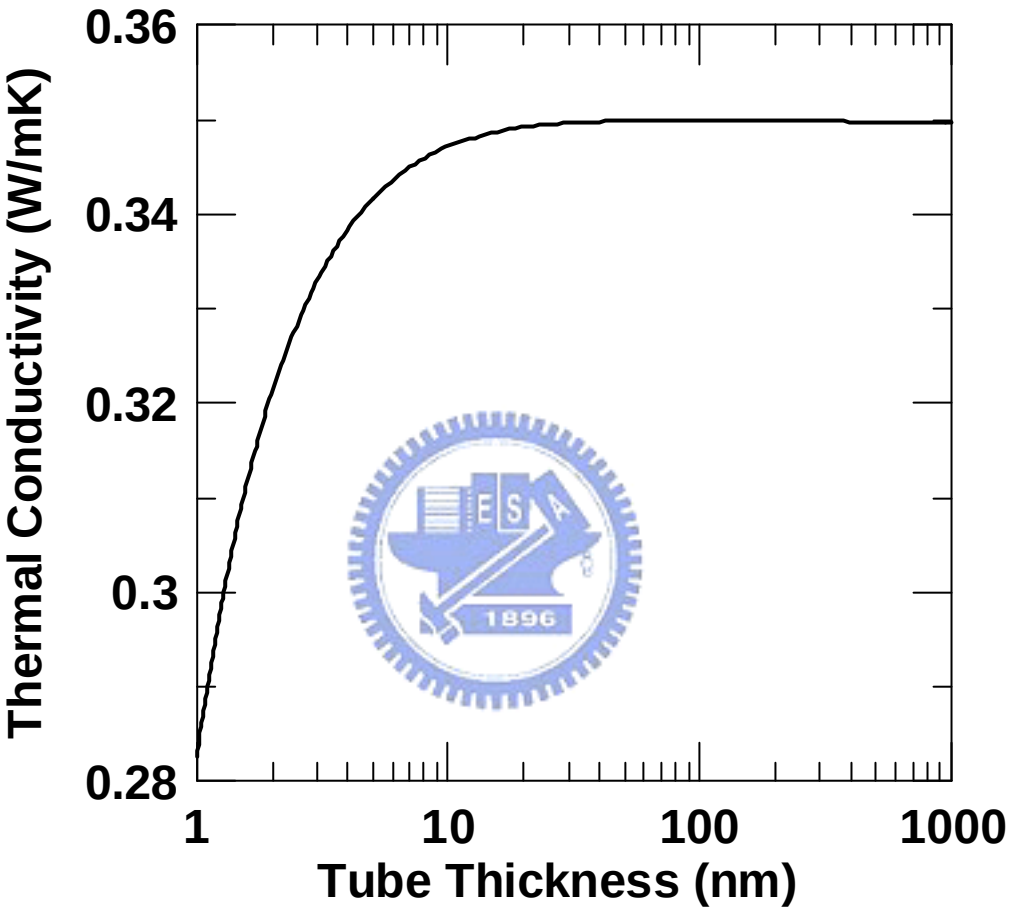

Fig. 5.12 The effect of tube thickness on the thermal conductivity of Bi_2Te_3/Sb_2Te_3 nano tube superlattices.

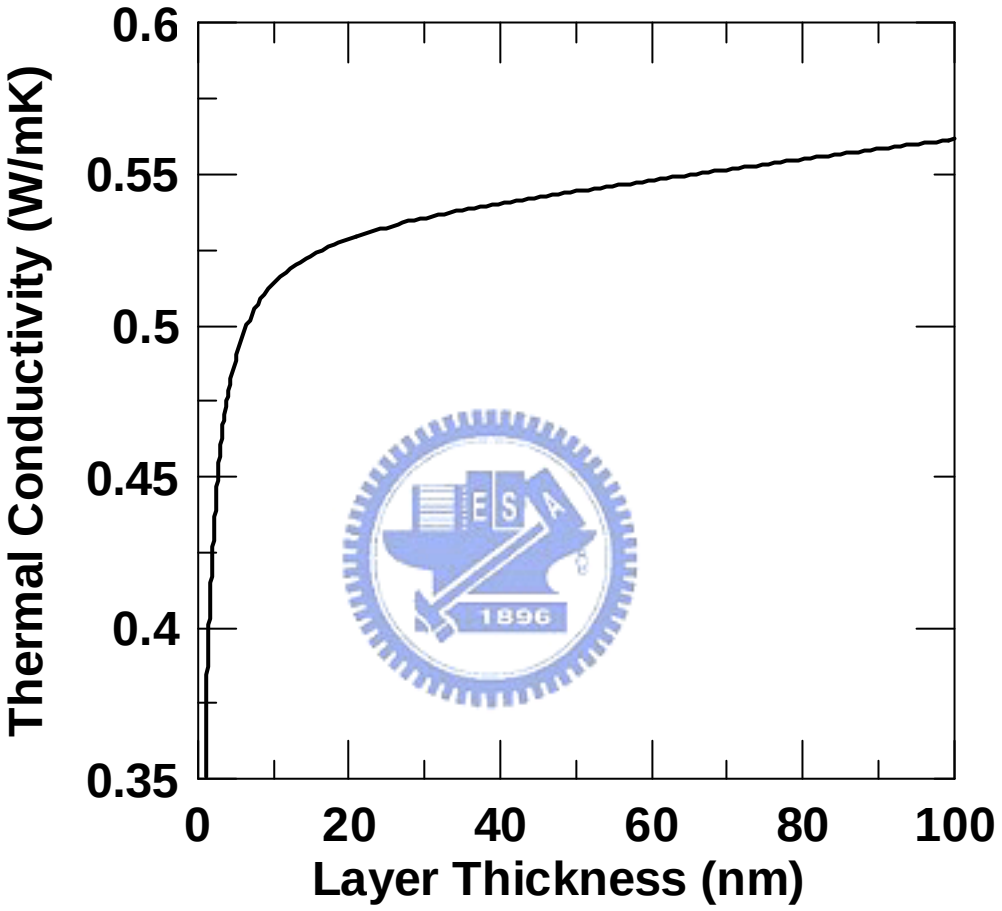

Fig. 5.13 The effect of layer thickness on the thermal conductivity of Bi_2Te_3/Sb_2Te_3 nano tube superlattices.

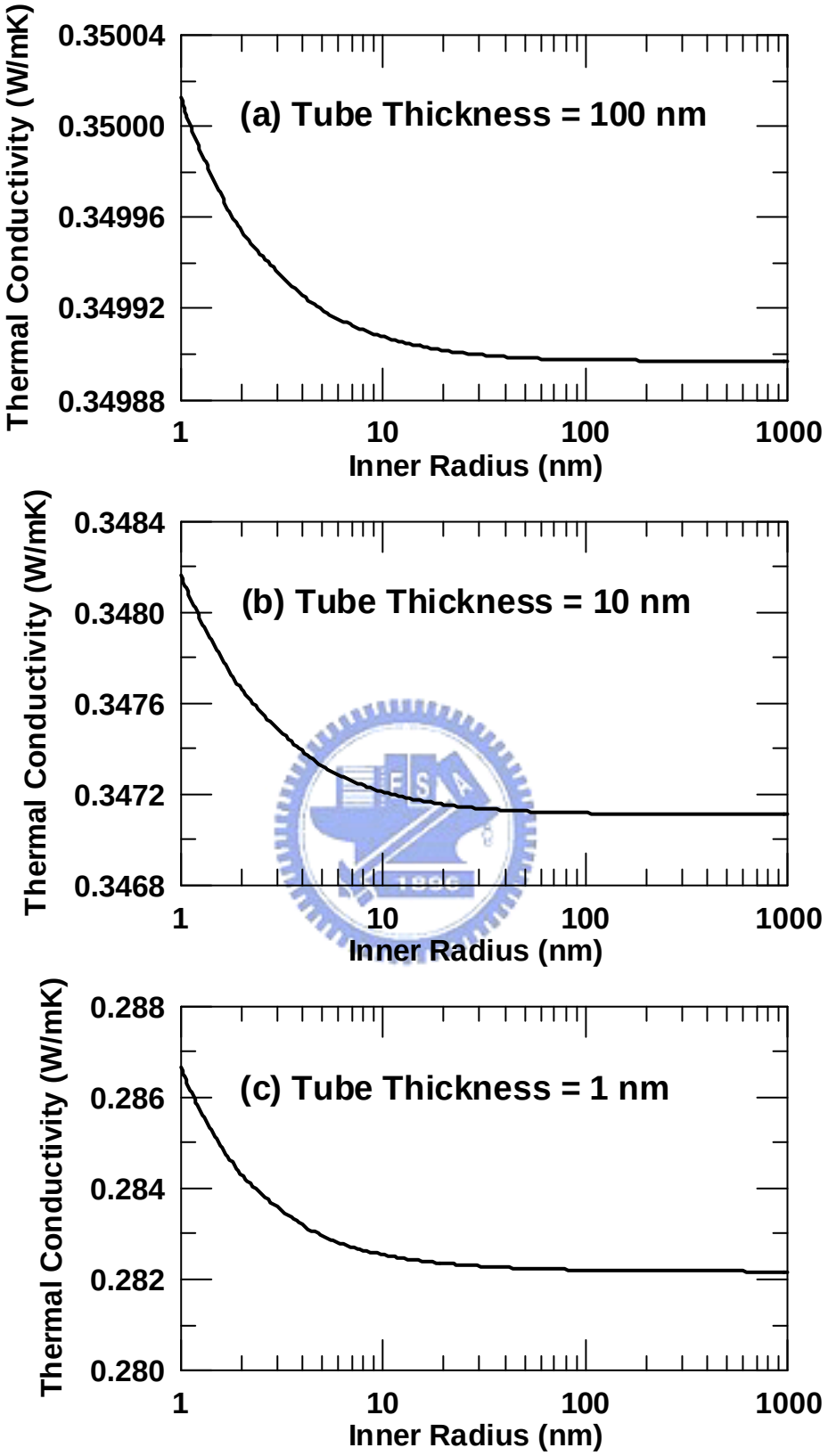

Fig. 5.14 The curvature effect on the thermal conductivity of Bi_2Te_3/Sb_2Te_3 nano tube superlattices.

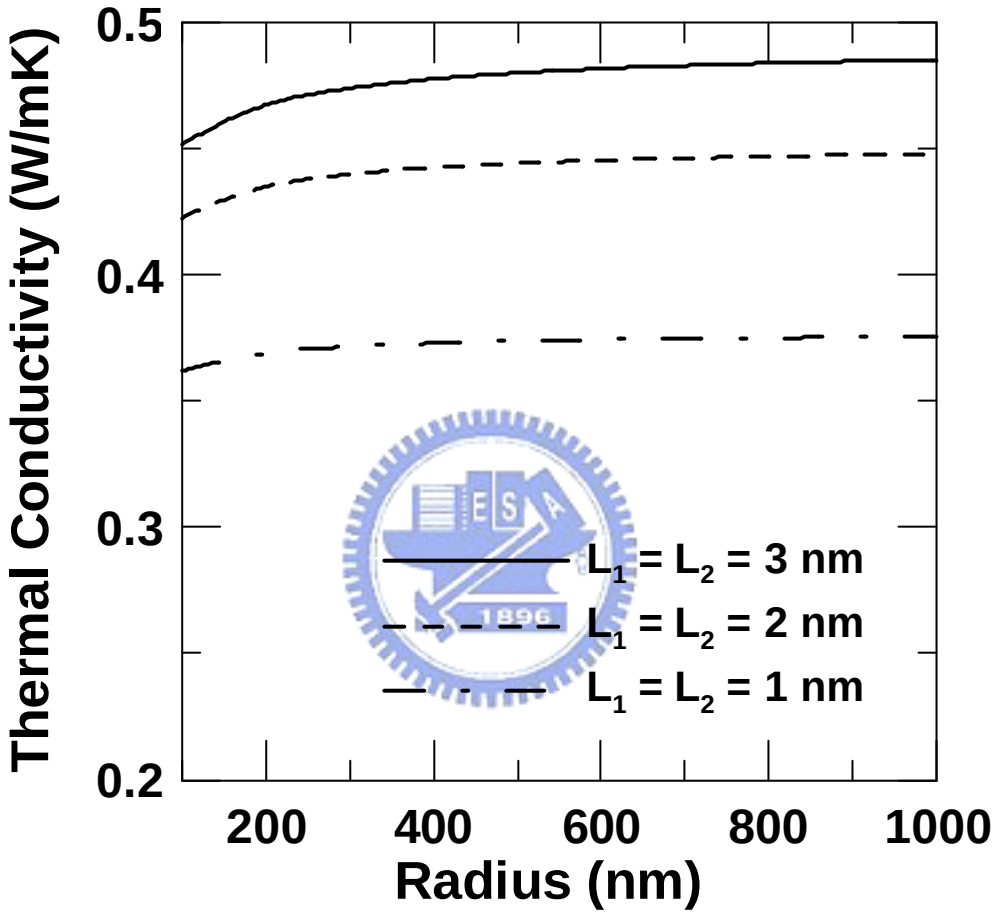

Fig. 5.15 The size effect on the thermal conductivity of Bi_2Te_3/Sb_2Te_3 nano wire superlattices.

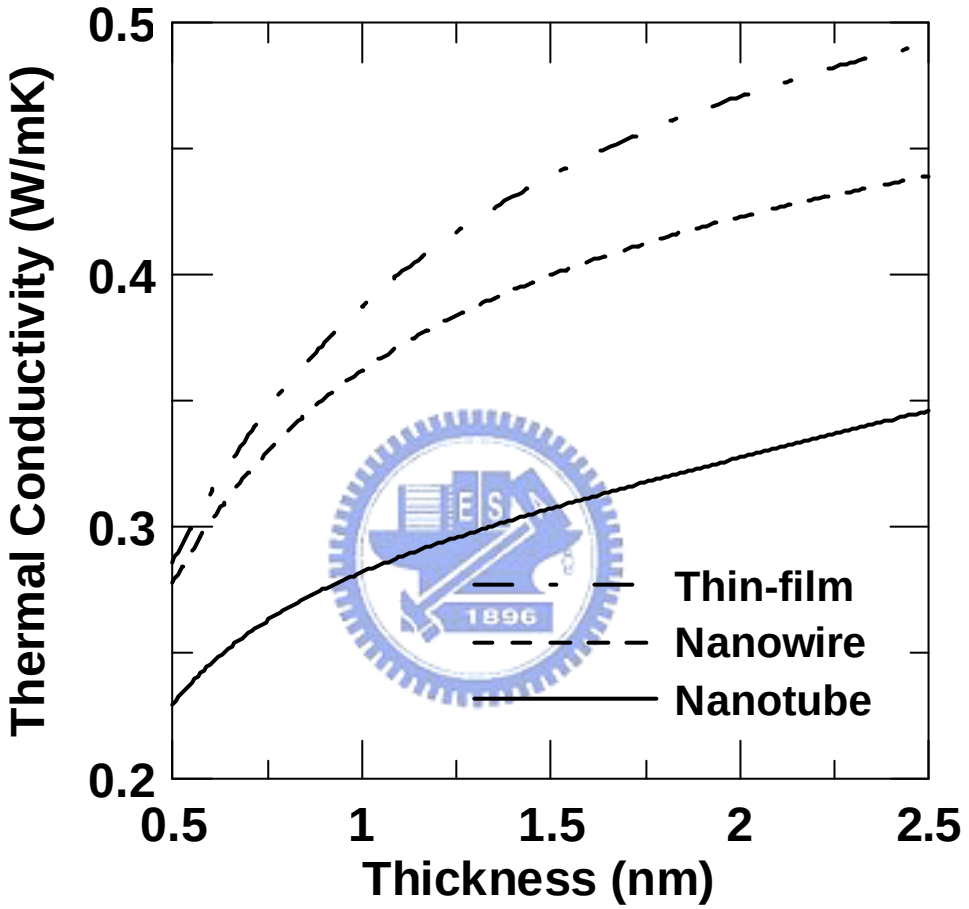

Fig. 5.16 The comparison of thermal conductivities of Bi_2Te_3/Sb_2Te_3 thin film, nano wire and nano tube superlattices.

6. INVERSE DETERMINATION OF SURFACE TEMPERATURE IN THIN-FILM/SUBSTRATE SYSTEMS

Thin-film/substrate systems are widely used in superconducting bolometers, microelectronics systems, and electro-optic devices. In such systems it is often necessary to know surface temperatures and temperature distributions within the media. These temperature profiles can be calculated if material thermal properties, initial and boundary conditions are given. However, in some circumstances, boundary conditions are difficult to determine. For example, if the surface of the thin-film is suffering laser heating, it is unsuitable for attaching a sensor on the surface. Hence, temperature detectors are placed inside the substrate. Use of the inverse methods allows determination of thermal properties and estimation of temperature distributions and unknown boundary conditions by means of internal or external measurements [102].

6.1 Analysis

6.1.1 Mathematical Formulation

Direct Problem Formulation

Consider one-dimensional conductive heat transfer in a two-layer medium as illustrated in Fig. 6.1. The temperature of the medium is initially T_0. At time $t = 0$, the temperature at $x = 0$ has risen to T_L while the temperature at $x = L_f$ is still T_0. All thermal properties in this study are assumed to be temperature-independent. For convenience in the subsequent analysis, nondimensional variables are defined as follows:

$$q_j = \frac{T_j}{T_L},\ t = \frac{a_1 t}{L_f^2},\ x = \frac{x}{L_f},\ x_1 = \frac{L_{f1}}{L_f},\ x_r = \frac{L_r}{L_f},\ \overline{Q}_j = \frac{L_f q_j}{k_j T_L}, \tag{6-1}$$

where a is the thermal diffusivity and k is the thermal conductivity. The subscript j represents layer j, where $j = 1$ or 2. The governing equations for this problem are

$$\frac{\partial q_j}{\partial t} = \frac{a_j}{a_1}\frac{\partial^2 q_j}{\partial x^2}. \tag{6-2}$$

The initial conditions are

$$q_j(0,x) = q_0. \tag{6-3}$$

The boundary conditions are

$$q_1(t,0) = 1, \tag{6-4a}$$

$$q_2(t,1) = q_0. \tag{6-4b}$$

At the interface, the radiation-boundary-condition model is employed, thus the heat flux continuity is

$$\frac{\partial}{\partial x}q_1(t,x_1) = \frac{k_2}{k_1}\frac{\partial}{\partial x}q_2(t,x_1) = -\frac{LT_L^3}{k_1}k\left[q_1^4(t,x_1) - q_2^4(t,x_1)\right], \tag{6-5}$$

where k is a function of the material properties of the two media in contact. Higher k represents less interface thermal resistance.

Inverse Problem Formulation

The inverse heat conduction problem is to estimate the temperature histories over the whole domain from internal temperature measurements. In this study, instead of using measured temperatures, the input data for the inverse heat conduction problem are predicted from the solution of a direct problem for a given set of boundary conditions.

The set of equations for the IHCP are Eq. (6-2) and Eq. (6-5) along with:

$$q_1(t,0) = ? \tag{6-6}$$

$$q_2(t,x_r) = Y_1(t) \tag{6-7a}$$

$$q_2(t,1) = Y_2(t) \tag{6-7b}$$

The medium is divided into a direct and an inverse region. The problem in the direct region, $x_r < x < 1$, is a boundary-value problem with boundary conditions given by the temperature measurements Y_1 and Y_2. Y_1 and Y_2 representing the temperature history of the first sensor located at $x = x_r$ and the second sensor located at $x = 1$, respectively. In this study, Y_1 and Y_2 were simulated by the solution of the direct heat-transfer problem. After the temperature distributions in the direct region were obtained, the temperature distributions in the inverse region were determined by the space-marching method.

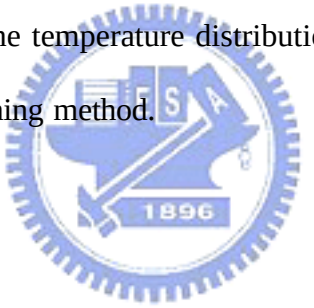

6.1.2 Numerical Method

The inverse estimation is not always numerically stable, which means small inaccuracies in the measured interior temperatures may cause large oscillations in the calculated surface conditions. Thus, many special methods have been proposed to improve the stability of numerical calculation results. The space-marching method is easy to use, accurate and stable [77]. Therefore, it was adopted to deal with the engineering problem in this manuscript. The calculations start on the boundary between direct and inverse regions and then are continued for the subsequent grids within the inverse region. The space-marching technique proposed by Raynaud and Bransier [84] uses the finite-difference method to approximate the governing equations. Central-difference approximations in space and time lead to

$$\frac{q_{i,j}^{n+1}-q_{i,j}^{n-1}}{2Dt}=\frac{a_j}{a_1}\frac{\overline{Q}_{i-1/2,j}^{n}-\overline{Q}_{i+1/2,j}^{n}}{Dx}, \tag{6-8}$$

where the subscripts $j=1$ or 2 represent Layer 1 or Layer 2, respectively. In addition, the dimensionless heat flux values $\overline{Q}_{i-1/2,j}^{n}$ and $\overline{Q}_{i+1/2,j}^{n}$ are approximated as follows:

$$\overline{Q}_{i-1/2,j}^{n}=-\frac{q_{i,j}^{n}-q_{i-1,j}^{n}}{Dx}, \tag{6-9a}$$

$$\overline{Q}_{i+1/2,j}^{n}=\frac{1}{2}\left(\overline{Q}_{i+1/2,j}^{n+1}+\overline{Q}_{i+1/2,j}^{n-1}\right)=-\frac{1}{2}\left[\frac{q_{i+1,j}^{n+1}-q_{i,j}^{n+1}}{Dx}+\frac{q_{i+1,j}^{n-1}-q_{i,j}^{n-1}}{Dx}\right]. \tag{6-9b}$$

It can be seen that the dimensionless heat flux $\overline{Q}_{i+1/2,j}^{n}$ is the average of central-difference at times $n+1$ and $n-1$. This will decrease the sensitivity to measurement errors and stabilize the inverse method. Substituting Eqs. (6-9a) and (6-9b) into Eq. (6-8) results in

$$q_{i-1,j}^{n}=q_{i,j}^{n}+\frac{a_1}{a_j}\frac{(\Delta x)^2}{2\Delta t}\left(q_{i,j}^{n+1}-q_{i,j}^{n-1}\right)-\frac{1}{2}\left(q_{i+1,j}^{n+1}-q_{i,j}^{n+1}+q_{i+1,j}^{n-1}-q_{i,j}^{n-1}\right). \tag{6-10}$$

The temperatures at times $n+1$ and $n-1$ are called future and past temperatures. If the temperature at time $n=N$ is desired to be calculated, the measurements should be known up to $I+N$ time steps. Here I is the number of the space grids in the inverse region. Eq. (6-10) cannot be used to calculate the temperature field at the final time step since it includes future temperatures. Thus, an explicit scheme that does not include future temperatures, proposed by D' Souza [103], is used to calculate the temperature distribution at the final time step. Backward-difference in time and central-difference in space lead to

$$\frac{q_{i,j}^{m}-q_{i,j}^{m-1}}{Dt}=\frac{a_j}{a_1}\frac{q_{i+1,j}^{m}-2q_{i,j}^{m}+q_{i-1,j}^{m}}{(Dx)^2}. \tag{6-11}$$

Rearranging the above equation yields

$$q_{i-1,j}^{m} = 2q_{i,j}^{m} - q_{i+1,j}^{m} + \frac{a_1}{a_j}\frac{(\Delta x)^2}{\Delta t}\left(q_{i,j}^{m} - q_{i,j}^{m-1}\right). \tag{6-12}$$

Thus, at each time step toward the unknown boundary, Eq. (6-10) is used for times $n=1$ to $m-1$, while Eq. (6-12) is used for $n=m$. The space-time grid for numerical calculations is shown in Fig. 6.2.

6.2 Results and Discussion

Grid-refinement and time-step-sensitivity studies have been done to ensure the accuracy of the numerical method. In general, the accuracy of a numerical method increases as the time step decreases. However, in the inverse method sensitivity to measurement errors increases due to the smallness of the time steps. Thus, a trade-off between accuracy and stability exists. In the following cases, the time step $\Delta t = 0.01$, the grid size $\Delta x = 0.01$, the thermal diffusivity ratio $a_2/a_1 = 0.1$, and the thermal conductivity ratio $k_2/k_1 = 0.1$ are employed.

Fig. 6.3 shows the exact and estimated temperature profiles for $k = 5\times10^{-4}$ over the time sequence. It can be seen that the absolute value of the slope in Layer 2 is greater than that in Layer 1 near the interface. Because k_2 is smaller than k_1 and $\frac{\partial}{\partial x}q_1(t,x_1) = \frac{k_2}{k_1}\frac{\partial}{\partial x}q_2(t,x_1)$, it is easy to determine that $\frac{\partial}{\partial x}q_2(t,x_1)$ is greater than $\frac{\partial}{\partial x}q_1(t,x_1)$. Moreover, owing to the existence of interface thermal resistance there is an abrupt temperature jump at the interface ($x = 0.5$). In this case, the first sensor is located at $x_r = 0.75$ and the second sensor is located at $x = 1$. Thus, $0.75 < x < 1$ is the direct region and $0 < x < 0.75$ is the inverse region. It can be

seen that inverse estimation predicts well in the region $0.5 < x < 0.75$. The maximum relative error is about 0.7%. However, a difference between exact and estimated values appears as the calculation marches through the interface. This phenomenon is obvious for the first few time steps. For example, the estimated values did not match the exact values very well at $t = 0.2$ (the relative error is about 1%), but they did at $t = 0.5$ and $t = 0.8$ (the relative errors are less than 0.1%). The temperature of the left surface (unknown in the inverse problem) suddenly rose from T_0 to T_L in the direct problem. Such an abrupt temperature jump could not be predicted accurately using a numerical method. Thus, estimation accuracy is not good for the first few time steps.

Three values of k were chosen to illustrate the effect of interface thermal resistance on the inverse solution: $k = 5\times10^{-5}$, $k = 1\times10^{-4}$, and $k \to \infty$ (without interface thermal resistance). Fig. 6.4(a) depicts the exact and estimated temperature distributions within the medium at $t = 0.3$, with the first sensor located at $x_r = 0.75$. It can be seen that the differences between exact and estimated values decrease as k increases. In other words, the accuracy of the inverse estimation increases as the interface thermal resistance decreases. Furthermore, it is interesting to note that the differences between the exact and estimated values trend toward diminution as the calculation marches through the interface to the left surface ($x = 0$). For example, the difference between the exact and estimated temperatures at $x = 0.4$, $x = 0.3$, and $x = 0.2$ are 0.005216, 0.004617, and 0.003221, respectively, for $k = 5\times10^{-5}$. The discrepancy between the estimated and exact temperatures seems to recover as the estimated solution moves to the surface. In order to investigate this phenomenon, another case was selected to be tested. The results of the case with $k_2/k_1 = 10$ were

plotted in Fig. 6.4(b). From Fig. 6.4(b), the results show that the discrepancy between the estimated and exact temperatures was slightly diverged as the estimated solution moves to the surface. However, all of these cases show that the error of inverse estimation of surface temperature is less than 1.3%.

Fig. 6.5 presents the exact and estimated surface temperature histories for $k = 5\times10^{-5}$, $k = 1\times10^{-3}$, and $k \to \infty$, with $x_r = 0.75$. The inverse estimation solution is not good for the first few time steps, as mentioned above, however, after about 10 time steps ($t = 0.1$), the estimated values approach to the exact values as time elapses. In other words, the relative error decreases when the time increases. The maximum relative error is about 1% at $t = 0.1$. Furthermore, the accuracy of the inverse method slightly increases as the interface thermal resistance decreases. However, in this case, the error is so small that it is generally not significant.

Fig. 6.6 shows the exact and estimated histories of the temperature difference (Δq) at the interface for $k = 1\times10^{-4}$, $k = 5\times10^{-4}$, and $k = 1\times10^{-3}$, with $x_r = 0.75$. As time elapses, the temperature difference at the interface initially increases until reaching maximum then decreases to a fixed value. Thus, the steady state is reached. The small value of k represents high interface thermal resistance that prevents heat from propagating from one material to the other, so the temperature difference at the interface decreases as k increases. Furthermore, the moment that the maximum temperature difference appears tends to shift toward short time as k decreases. Inverse estimation predicts this phenomenon accurately after a few time steps.

Fig. 6.7 illustrates the exact and estimated temperature distributions for various sensor locations, with $k = 1\times10^{-4}$. At $t = 0.2$, the accuracy of the inverse estimation with $x_r = 0.60$ is better than that of the other two cases. The small value of x_r

means that the sensor was located near the unknown boundary. Thus, the best inverse solution is obtained with the sensor closest to the unknown boundary. However, this phenomenon is not significant as time elapses. At $t = 0.6$, $x_r = 0.60$, $x_r = 0.75$, and $x_r = 0.90$ predict almost the same temperature distribution and they match the exact value reasonably well. The relative errors are less than 0.1% for these three cases at $t = 0.6$.

The maximum inverse estimation error occurs at the interface for our demonstrated case. Thus, the inverse estimation error at the interface must be thoroughly examined. E_{int} is the absolute value of the relative error at the interface. It is chosen as an index of the inverse estimation error. Fig. 6.8 shows the inverse estimation error at the interface for $k = 5\times10^{-5}$, $k = 1\times10^{-4}$, $k = 5\times10^{-4}$, and $k \to \infty$ with $x_r = 0.75$. For the first few time steps such as $t < 0.1$, E_{int} varies sharply with time. As mentioned before, an abrupt temperature jump could not be predicted accurately using a numerical method so that the estimation accuracy is not good for the first few time steps. Furthermore, the existence of interface thermal resistance will make the estimation less accurate. Therefore, E_{int} is affected by both k and t. There is no general trend for E_{int} when t is less than 0.1. However, the results show that E_{int} decreases as k increases after $t = 0.1$, i.e. less interface thermal resistance results in more accurate prediction. Besides, the figure demonstrates again that the inverse estimation error decreases as time elapses.

In order to examine the influence of sensor locations on the inverse estimation error at the interface, three different sensor location, $x_r = 0.60$, $x_r = 0.75$, and $x_r = 0.90$ were designated as sample cases. Fig. 6.9 depicts inverse estimation error at the interface for various sensor locations with $k \to \infty$. It is obvious that E_{int}

decreases as x_r increases. Thus, the inverse estimation predicts more accurately while the sensor is close to the unknown boundary.

The discussion above shows that the inverse method provides a good estimation with exact input data. However, in practical engineering applications, measurement errors are unavoidable. Thus, the effect of measurement errors on the inverse method must be taken into account. The temperature data for the measurement locations were calculated from direct problems to simulate measurements. The simulated temperature measurements used in the inverse problems are considered to include measurement errors. In this study, random errors were added to the exact temperatures. The measured temperature $T_{measured}$ can be expressed as

$$T_{measured} = T_{exact} + vT_{exact}, \qquad v < |s|, \tag{6-13}$$

where T_{exact} is the exact temperature, v is the random error, and s is the bound of v.

Fig. 6.10 depicts the exact and estimated surface temperature histories for various sensor locations, with $k = 1\times10^{-3}$, when measurement errors are taken into account. It can be seen that large measurement errors make the estimation less accurate. Furthermore, the inaccuracy is amplified by large x_r values. For the cases with exact input data (without measurement errors), sensor locations merely slightly affect the accuracy of the inverse estimation. However, the effect will be amplified if measurement errors are taken into account. Thus, for practical engineering problems in which measurement errors are unavoidable, sensors must be located as close to unknown boundaries as possible. Fig. 6.11 shows an estimated surface temperature history with (a) $k = 1\times10^{-4}$ and (b) $k \to \infty$. Comparing Figs. 6.11(a) and 6.11(b), it is clear that the differences between exact and estimated values are amplified when

thermal resistance exists at the interface.

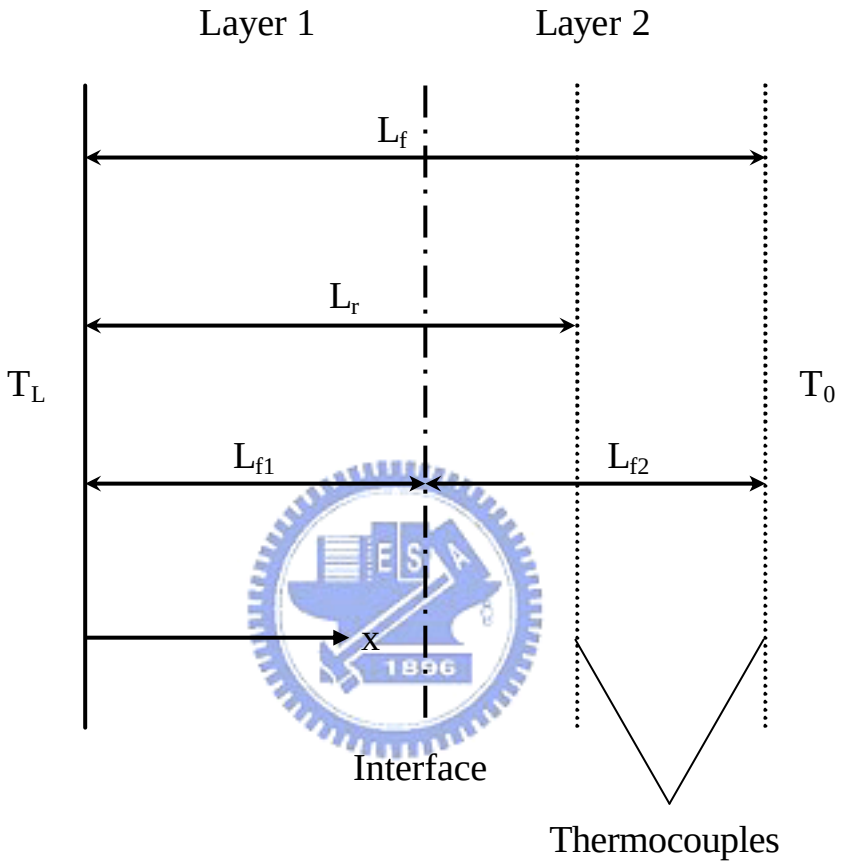

Fig. 6.1 Schematic diagram of a two-layer medium

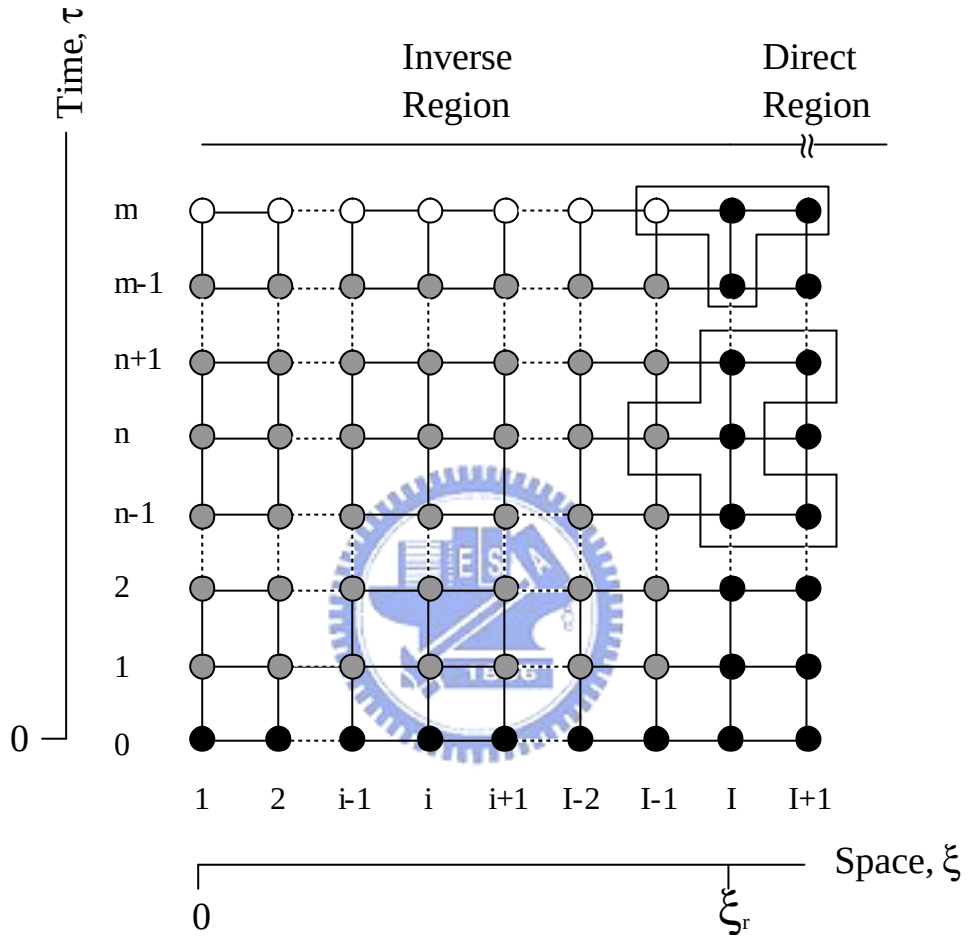

Fig. 6.2 Space-time grid for numerical calculations [104]; ◍: temperatures estimated by Raynaud and Bransier method [84], ○: temperatures estimated by D'Souza method [103], ●: known temperatures

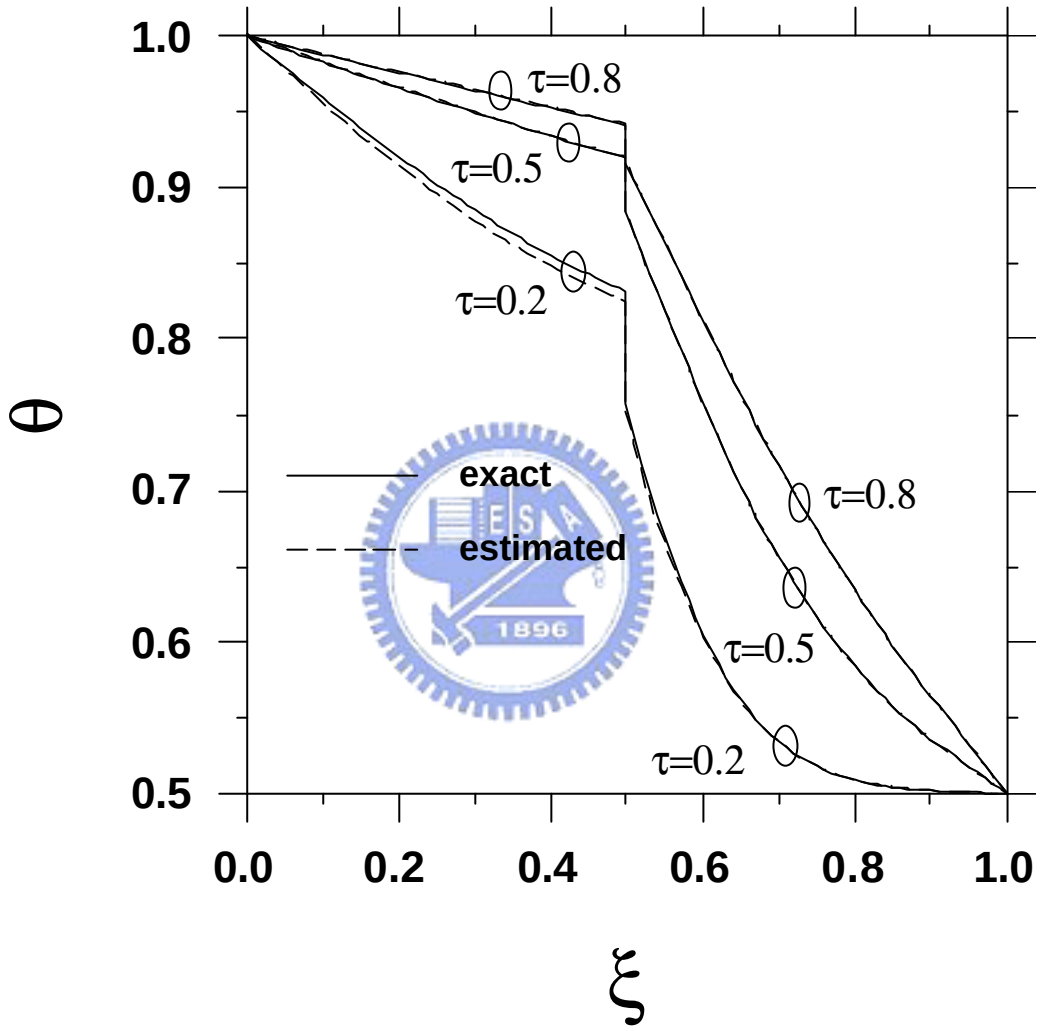

Fig. 6.3 Exact and estimated temperature distributions with $k = 5\times10^{-4}$ over the time sequence.

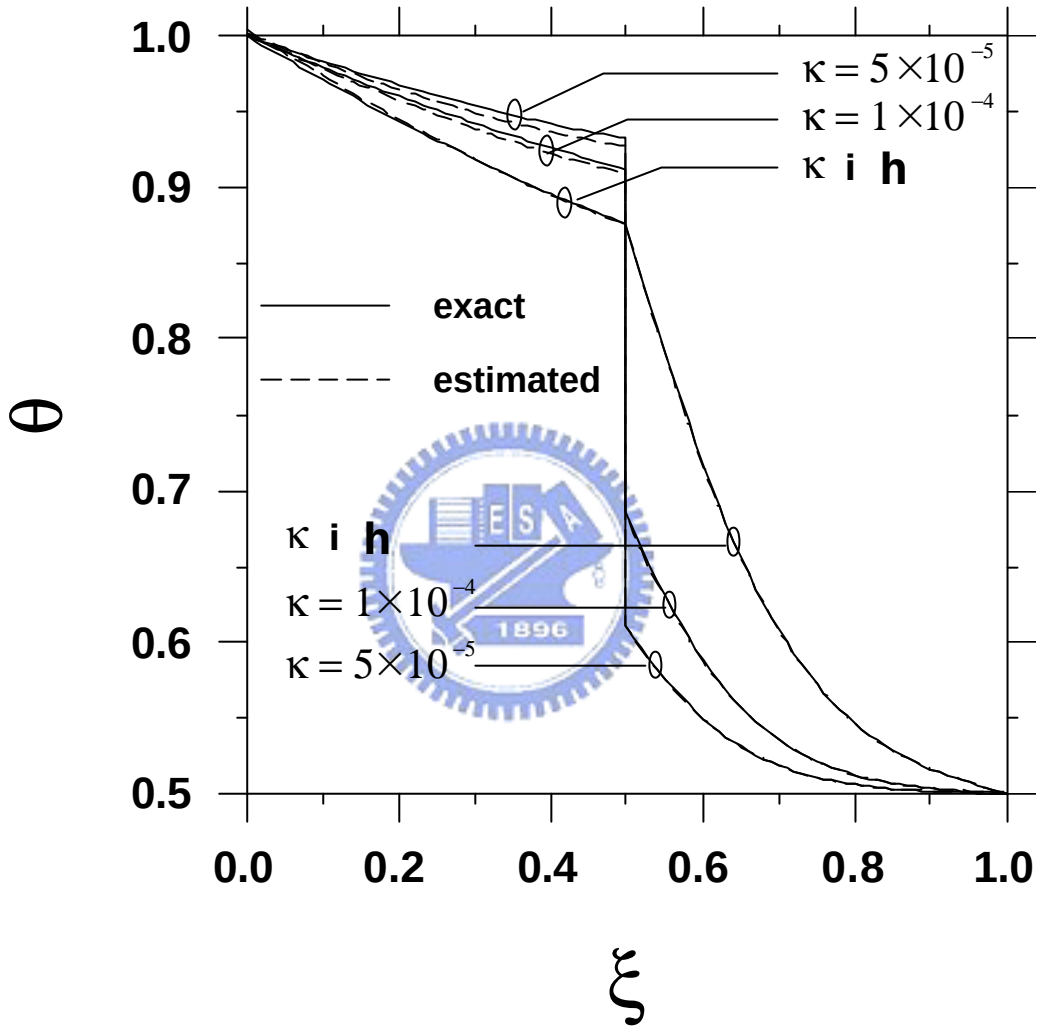

Fig. 6.4(a) Exact and estimated temperature distributions at $t = 0.3$ for various interface conditions with $k_2/k_1 = 0.1$.

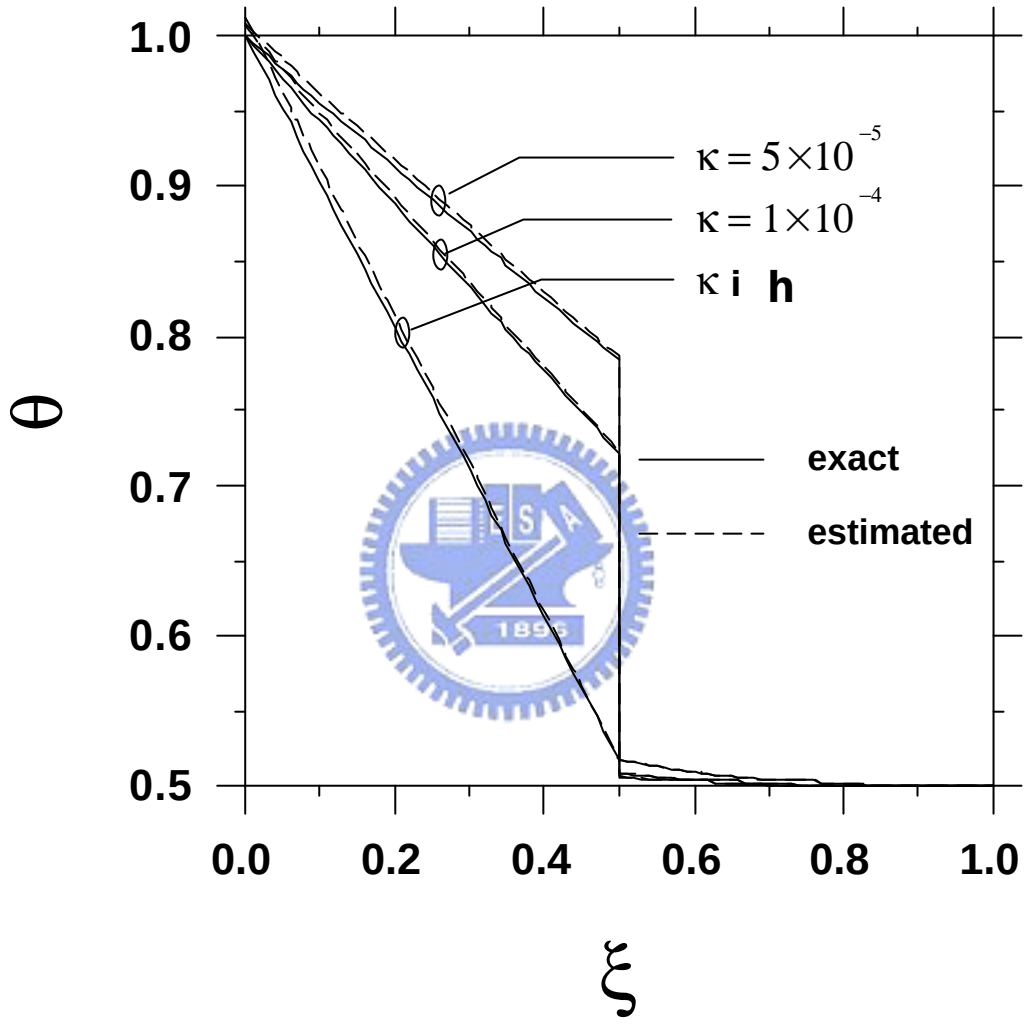

Fig. 6.4(b) Exact and estimated temperature distributions at $t = 0.3$ for various interface conditions with $k_2/k_1 = 10$.

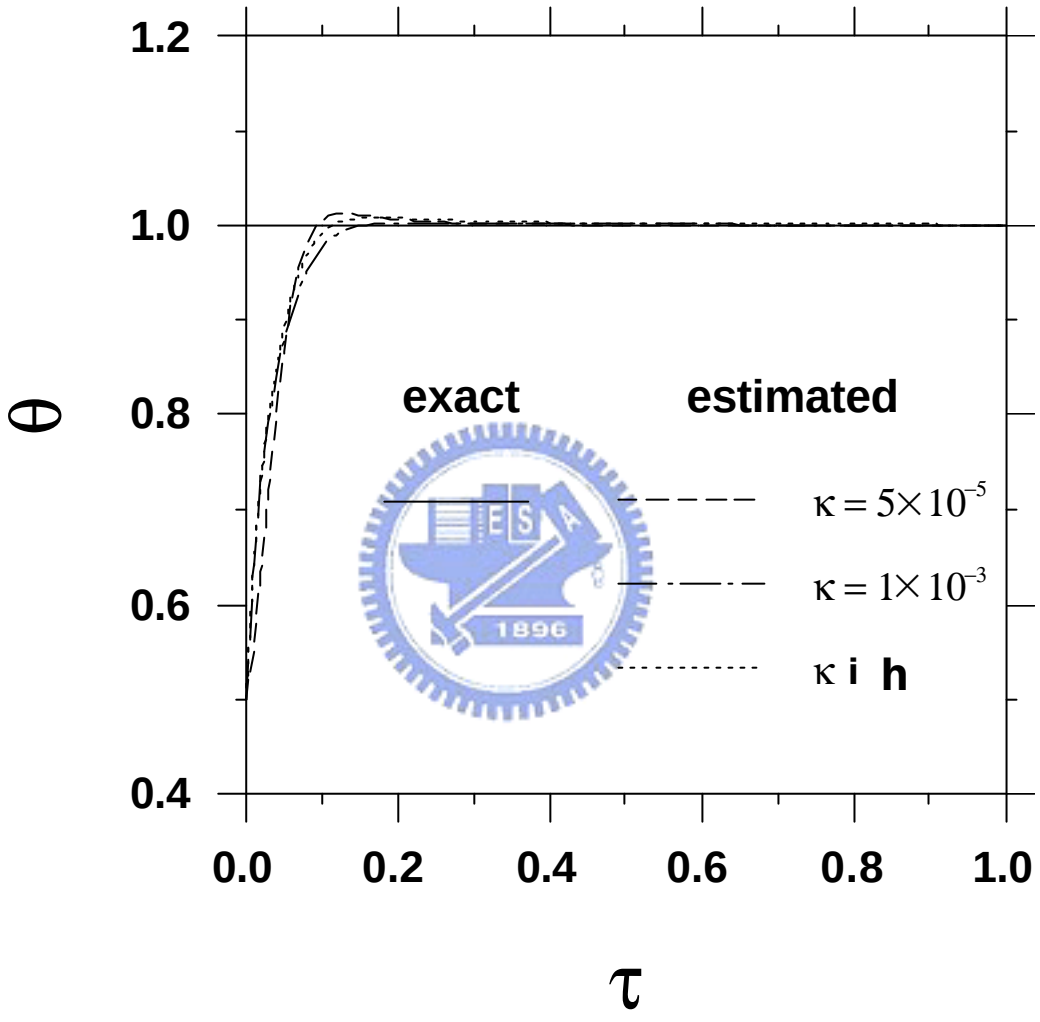

Fig. 6.5 Exact and estimated surface temperature histories for various interface conditions.

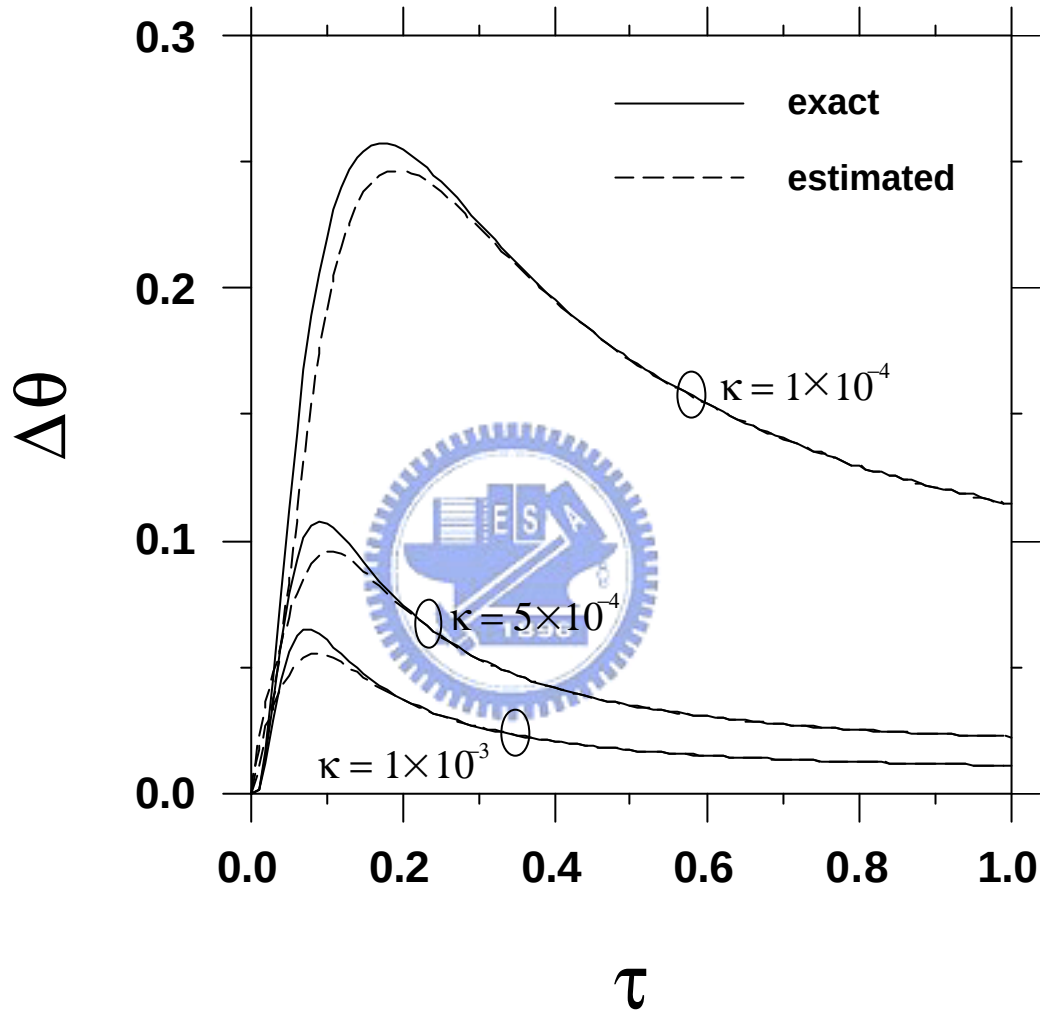

Fig. 6.6 Exact and estimated temperature-difference (Δq) histories at the interface for $k = 1\times10^{-4}$, $k = 5\times10^{-4}$, and $k = 1\times10^{-3}$ with $x_r = 0.75$.

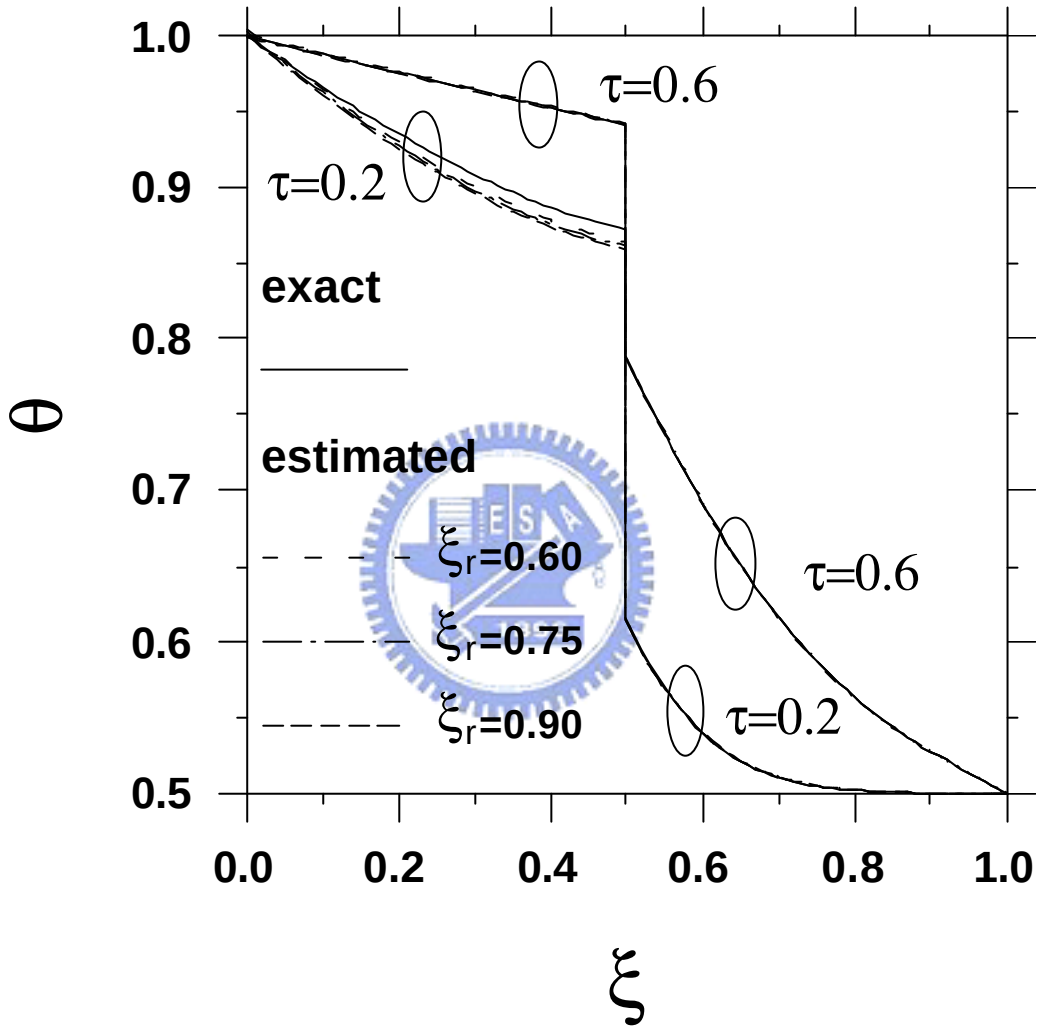

Fig. 6.7 Exact and estimated temperature distributions for various sensor locations with $k = 1\times10^{-4}$.

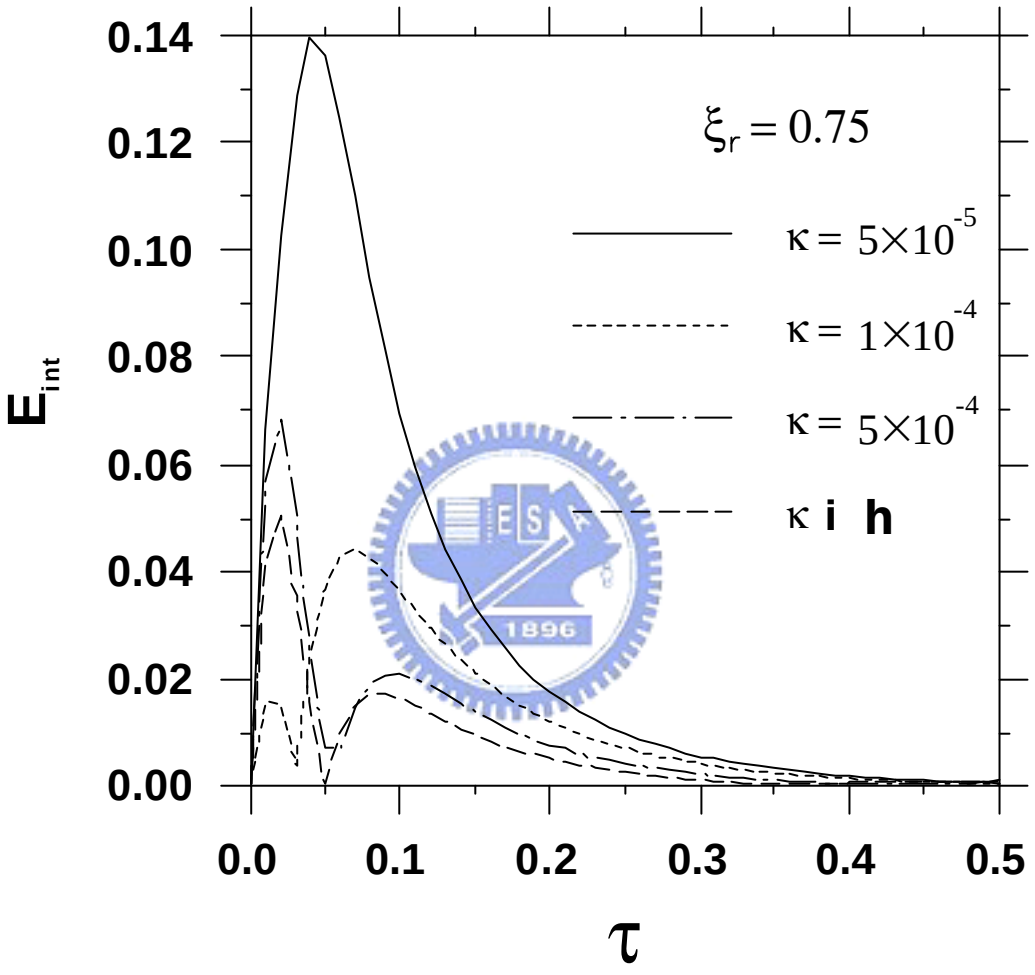

Fig. 6.8 Inverse estimation error at the interface for $k = 5\times10^{-5}$, $k = 1\times10^{-4}$, $k = 5\times10^{-4}$, and $k \to \infty$ with $x_r = 0.75$.

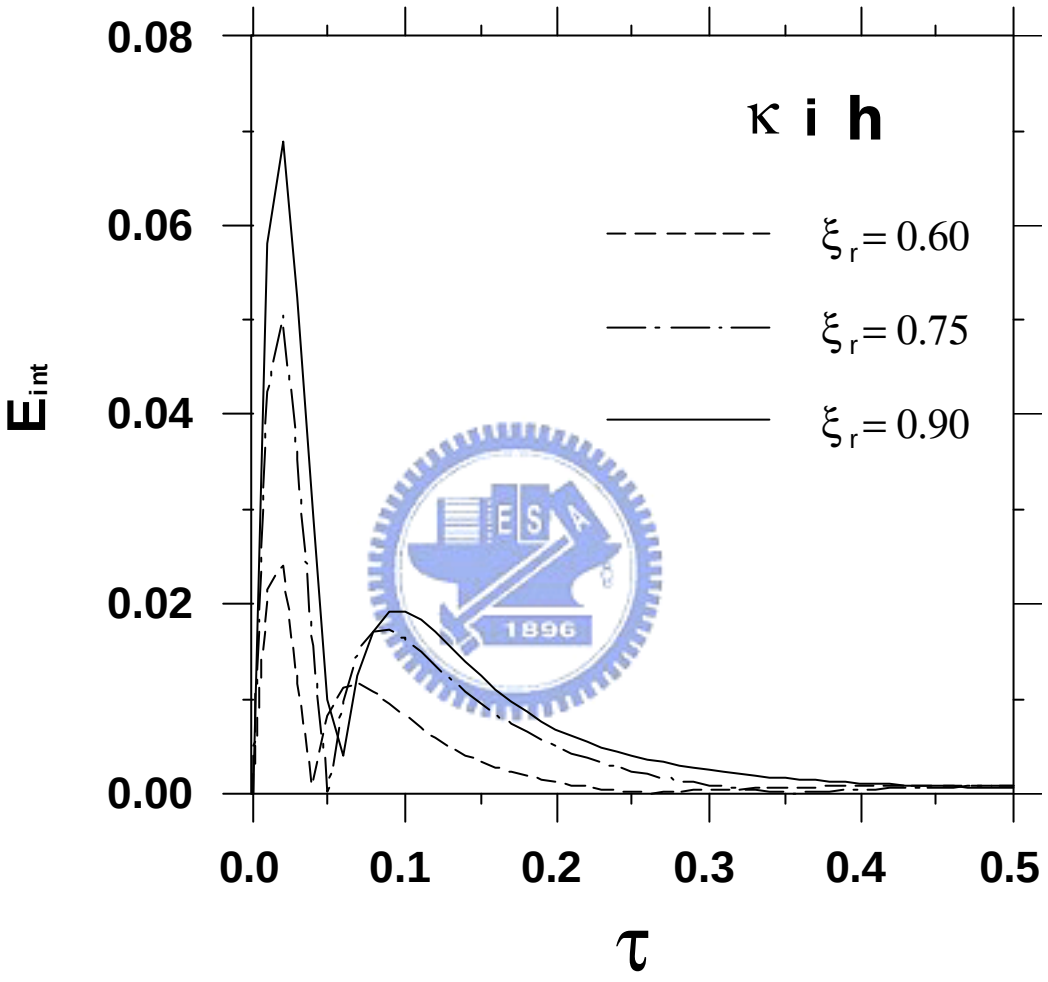

Fig. 6.9 Inverse estimation error at the interface for various sensor locations with $k \to \infty$.

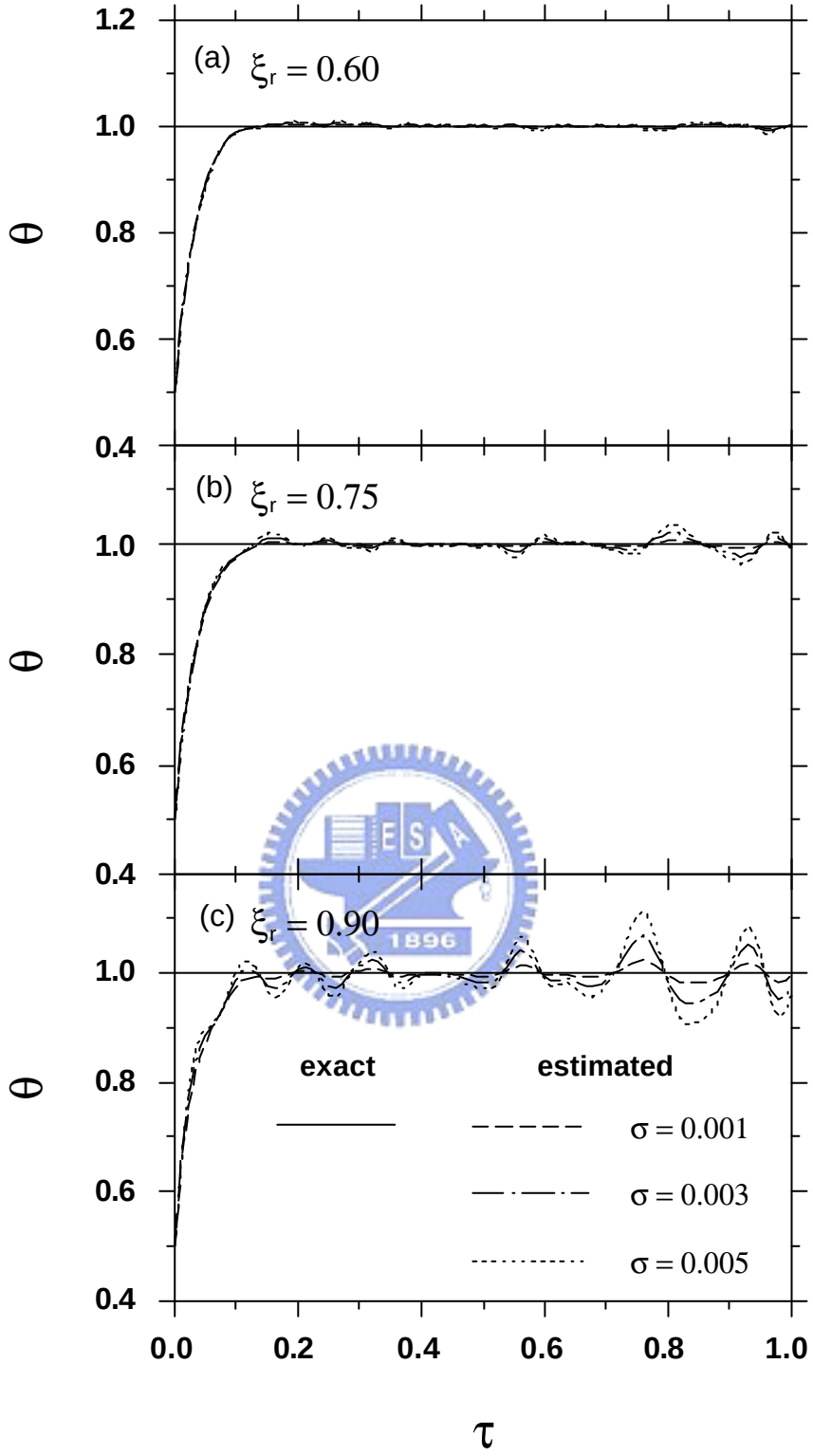

Fig. 6.10 Exact and estimated surface temperature histories for measurement errors 0.1%, 0.3%, and 0.5%, with $k = 1\times10^{-3}$ with the first sensor located at (a) $x_r = 0.60$, (b) $x_r = 0.75$, (c) $x_r = 0.90$.

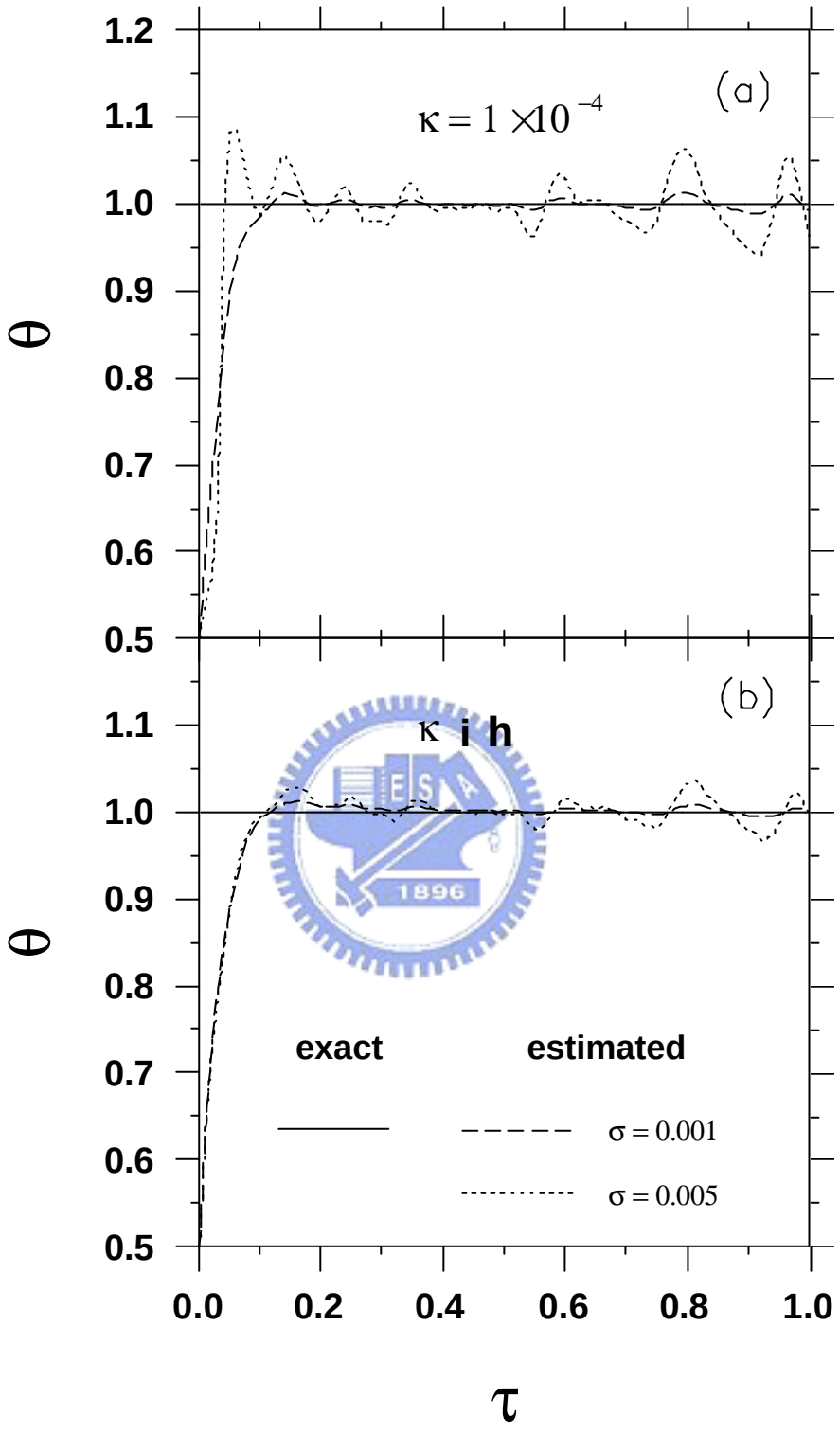

Fig. 6.11 Exact and estimated surface temperature histories for measurement errors 0.1% and 0.5% with interface thermal resistance (a) $k = 1\times10^{-4}$, (b) $k \to \infty$.

7. CONCLUSIONS AND RECOMMENDATION

This thesis discusses microscale heat transfer phenomena in solid-state multilayer structures. We examine the size, interface and geometry effects on the thermal conductivity of materials. This chapter draws some conclusions as well as directions for future work in this area.

The phonon radiative transfer model is partially ballistic, partially wavelike, and partially diffusive. EPRT approaches to Fourier limit (totally diffusive) when the thickness of the film is much greater than the phonon mean free path. However, EPRT reduces to Casimir limit (totally ballistic) when the thickness of the film is much less than the phonon mean free path. The study suggests a profile for engineers to apply conduction heat transfer models in different film thickness. When the ratio of film thickness to phonon mean free path is great than 100, Fourier law is a good approximation to deal with conduction heat transfer problem in dielectric thin film.

Extending the one-layer system to a two-layer system, the interface effect on the thermal conductivity must be considered. Microscale heat transport in a two-layer concentric circular cylinder with interface thermal resistance is examined in this study. The size and curvature effects on the effective thermal conductivity and the interface thermal resistance are examined in detail. The results show that the reduction of size will reduce the effective thermal conductivity. In addition, the effective thermal conductivity increases as the curvature increases. However, the size and curvature effects on interface thermal resistance are not significant when the DMM is employed to describe the interface condition.

Microscale heat transfer in two-dimensional micro tubes is also examined. The results show that the curvature effect on the effective thermal conductivity is not

significant. However, the reduction of thickness or height will reduce the effective thermal conductivity. Thus, the miniaturization of microelectronic devices will reduce the ability of heat transfer and may cause the failure of devices if the size effect is ignored.

Extending the foregoing analysis on microscale heat transfer, size effects on the performance of thermoelectric micro coolers are explored in detail. Thin film, nano wire and nano tube superlattices are utilized to make thermoelectric micro coolers and EPRT as well as DMM are used to model the microscale heat transfer in the micro cooler. The results show that the layer thickness has significant influence on the effective thermal conductivity of thermoelectric materials in superlattice structures. The reduction of the layer thickness will reduce the thermal conductivity of superlattices and thus enhance their thermoelectric performance. For a fixed total film thickness, increasing number of periods means decreasing layer thickness of each layer and increasing number of interfaces. Thus, the thermal conductivity decreases with increasing number of periods. In addition, low-dimensionality offers more boundary scattering and causes further reduction in thermal conductivity of low-dimensional thermoelectric materials. Nano wire or nano tube superlattices are potential materials for high performance thermoelectric devices.

After knowing what parameters affecting the effective thermal conductivity and how they influencing, the thermophysical properties of materials can be properly defined. The effective thermal conductivity and the temperature histories in the interior points are used to estimate the surface temperature in thin-film/substrate systems. This study presents a numerical analysis of estimating transient behavior of surface temperatures for thin-film/substrate system using an inverse method. The acoustic mismatch model was employed to model the interface thermal resistance

between thin-film and substrate. The space-marching technique is adopted for the analysis of the inverse heat conduction problem. Numerical results show that the inverse method accurately estimated the surface conditions and temperature distributions in a two-layer system even with an abrupt temperature drop in the interface. Sensor locations and interface thermal resistance just slightly affected the accuracy of the inverse estimation during the transient process when exact input data (without measurement errors) were applied. However, inaccuracy might be amplified by interface thermal resistance and sensor locations if measurement errors exist.

Thermal transport theory based on Boltzmann equation successfully describes the microscale heat transfer phenomena in solids. This study closely examines the size effects on the thermal conductivity of solid-state devices with multilayer structures. In addition, the study of size effects on the electrical conductivity can be found elsewhere. However, there are rare studies that simultaneously deal with heat and electron transport in solids. It would be more valuable to simultaneously predict the thermal and electrical conductivity of a miniaturized thermoelectric device since heat transfer and electron transfer are not independent. Besides, we need more experimental results to demonstrate the validity of the microscale heat transfer theory. Unfortunately, the reported thermophysical properties of materials in small scale are very few. It is difficult to fabricate perfect micro structures and measurements of thermophysical properties are not easy. Future work should be emphasized in experimental researches, particularly in developing the measurement method that simultaneously measures the thermal conductivity, the electrical conductivity and the Seebeck coefficient of thermoelectric materials.

REFERENCES

1. Tien, C. L., Majumdar, A., and Gerner, F. M., 1998, *Microscale Energy Transport*, Taylor & Francis, Washington, DC.
2. Lambropoulos, J. C., Jacobs, S. D., Burns, S. J., Shaw-Klein, L., and Hwang, S. S., 1991, "Thermal Conductivity of Thin Films: Measurement and Microstructural Effects," ASME HTD, **184**, pp. 21-32.
3. Tien, C. L. and Chen, G., 1994, "Challenges in Microscale Radiative and Conductive Heat Transfer," ASME Journal of Heat Transfer, **116**, pp. 799-807.
4. Lee, S. M. and Cahill, D. G., 1997, "Heat Transport in Thin Dielectric Films," Journal of Applied Physics, **81**, pp. 2590-2595.
5. Ziman, J. M., 1960, *Electrons and Phonons*, Clarendon Press, Oxford.
6. Mahan, G. D., 1994, "Thermionic Refrigeration," Journal of Applied Physics, **76**, pp. 4362-4366.
7. Riffat, S. B. and Ma, X., 2003, "Thermoelectrics: A Review of Present and Potential Applications," Applied Thermal Engineering, **23**, pp. 913-935.
8. Goldsmid, H. J., 1960, *Applications of Thermoelectricity*, John Wiley & Sons, New York.
9. DiSalvo, F. J., 1999, "Thermoelectric Cooling and Power Generation," Science, **285**, pp. 703-706.
10. Chen, G., and Shakouri, A., 2002, "Heat Transfer in Nanostructures for Solid-State Energy Conversion," ASME Journal of Heat Transfer, **124**, pp. 242-252.
11. Khitun, A., Wang, K. L., and Chen, G., 2000, "Thermoelectric Figure of Merit Enhancement in a Quantum Dot Superlattice," Nanotechnology, **11**, pp. 327-331.
12. Esaki, L., and Tsu, R., 1970, "Superlattice and Negative Differential

Conductivity in Semiconductors," IBM Journal of Research and Development, **14**, pp.61-65.

13. Tamura, S., and Tanaka, Y., 1999, "Phonon Group Velocity and Thermal Conduction in Superlattices," Physical Review B, **60**, pp. 2627-2630.
14. http://www.elcot.com/nano/nanomachine.htm
15. Dillon, A. C., Jones, K. M., Bekkedahl, T. A., Kiang, C. H., Bethune, D. S., and Heben, M. J., 1997, "Storage of Hydrogen in Single-Walled Carbon Nanotubes," Nature, **386**, pp. 377-379.
16. Gao, B., Kleinhammes, A., Tang, X. P., Bower, C., Fleming, L., Wu, Y., and Zhou, O., 1999, "Electrochemical Intercalation of Single-Walled Carbon Nanotubes with Lithium," Chemicl Physics Letters, **307**, pp. 153-157.
17. Yang, J., Lu, F, Kostiuk, L. W., and Kwok, D. Y., 2003, "Electrokinetic Microchannel Battery by Means of Electrokinetic and Microfluidic Phenomena," Journal of Micromechanics and Microengineering, **13**, pp. 963-970.
18. Kim, J., Kang, Y. T., and Choi, C. K., 2004, "Analysis of Convective Instability and Heat Transfer Characteristics of Nanofluids," Physics of Fluids, **16**, pp. 2395-2401.
19. Keblinski, P., Phillpot, S. R., Choi, S. U. S., and Eastman, J. A., 2002, "Mechanisms of Heat Flow in Suspensions of Nano-Sized Particles (Nanofluids)," International journal of Heat and Mass Transfer, **45**, pp. 855-863.
20. Shaheen, S. E., Brabec, C. J., Sariciftci, N. S., Padinger, F., Fromherz, T., and Hummelen, J. C., 2001, "2.5% Efficient Organic Plastic Solar Cells," Applied Physics Letters, **78**, pp. 841-843.
21. Huynh, W. U., Dittmer, J. J., Libby, W. C., Whiting, G. L., and Alivisatos, A. P., 2003, "Controlling the Morphology of Nanocrystal-Polymer Composites for

Solar Cells," Advanced Functional Materials, **13**, pp. 73-79.

22. Huynh, W. U., Dittmer, J. J., and Alivisatos, A. P., 2002, "Hybrid Nanorod-Polymer Solar Cells," Science, **295**, pp. 2425-2427.
23. Abramson, A. R., Tien, C. L., and Majumdar, A., 2002, "Interface and Strain Effects on the Thermal Conductivity of Heterostructures: A Molecular Dynamics Study," ASME Journal of Heat Transfer, **124**, pp. 963-970.
24. Maxwell, J. C., 1867, "On the Dynamic Theory of Gases," Philosophical Transaction, **157**, pp. 49-88.
25. Cattaneo, C., 1958, "A Form of Heat Conduction Equation which Eliminates the Paradox of Instantaneous Propagation," Compute Rendus, **247**, pp. 431-433.
26. Vernotte, P., 1958, "Les Paradoxes de la theorie continue de l'equation de la chaleur," Compute Rendus, **246**, pp. 3145-3155.
27. Kaganov, M. I., Lifshitz, I. M. and Tanatarov, 1957, "Relaxation Between Electrons and Crystalline Lattices," Soviet Phys. JETP, **4**, pp. 173-178.
28. Anisimov, S. I., Kapeliovich, B. L. and Perel'man, T. L., 1974, "Electron Emission from Metal Surfaces Exposed to Ultra-Short Laser Pulses," Soviet Phys. JETP, **39**, pp. 375-377.
29. Qiu, T. Q. and Tien, C. L., 1993, "Heat Transfer Mechanisms During Short-Pulse Laser Heating of Metals," ASME Journal of Heat Transfer, **115**, pp. 835-841.
30. Guyer, R. A. and Krumhansl, 1966, "Solution of the Linearized Boltzmann Equation," Physical Review, **148**, pp. 766-778.
31. Majumdar, A., 1993, "Microscale Heat Conduction in Dielectric Thin Films," ASME Journal of Heat Transfer, **115**, pp. 7-16.
32. Marshall, C. D., Fishman, I. M., Dorfman, R. C., Eom, C. B., and Fayer, M. D., 1992, "Thermal Diffusion, Interfacial Thermal Barrier, and Ultrasonic

Propagation in $YBa_2Cu_3O_7$ Thin Films: Surface-Selective Transient-Grating Experiments," Physical Review B, **45**, pp. 10009-10021.

33. Prasher, R. S. and Phelan, P. E., 1997, "Review of Thermal Boundary Resistance of High-Temperature Superconductors," Journal of Superconductivity, **10**, pp. 473-484.
34. Herth, P. and Weis, O., 1970, "Radiation Temperature of Thermal Phonon Radiator," Z. Angew. Phys., **29**, pp. 101-109.
35. Swartz, E. T. and Pohl, R. O., 1989, "Thermal Boundary Resistance," Reviews of Modern Physics, **61**, pp. 605-668.
36. Prasher, R. S. and Phelan, P. E., 2001, "A Scattering-Mediated Acoustic Mismatch Model for the Prediction of Thermal Boundary Resistance," ASME Journal of Heat Transfer, **123**, pp. 105-112.
37. Flik, M. I., Choi, B. I. and Goodson, K. E., 1992, "Heat Transfer Regimes in Microstructures," ASME Journal of Heat Transfer, **114**, pp. 666-674.
38. Majumdar, A, 1998, "Microscale Transport Phenomena," Chapter in *Handbook of Heat Transfer*, Editors: Rohsenow, W. M., Hartnett, J. P. and Cho, Y. I., McGraw-Hill, New York.
39. Kittel, C., 1986, *Introduction to Solid State Physics*, Wiley, New York.
40. Chen, G., 1999, "Phonon Wave Effects on Heat Conduction in Thin Films," ASME Journal of Heat Transfer, **121**, pp. 945-953.
41. Mazumder, S. and Majumdar, A., 2001, "Monte Carlo Study of Phonon Transport in Solids Thin Films Including Dispersion and Polarization," ASME Journal of Heat Transfer, **123**, pp. 749-759.
42. Gombosi, T. I., 1994, *Gaskinetic Theory*, Cambridge University Press, New York.

43. Joshi, A. A. and Majumdar, A., 1993, "Transient Ballistic and Diffusive Phonon Heat Transport in Thin Films," Journal of Applied Physics, **74**, pp. 31-39.

44. Nahum, M., Verghese, S., Richards, P. L., and Char, K., 1991, "Thermal Boundary Resistance for $YBa_2Cu_3O_{7-\delta}$ Films," Applied Physics Letters, **59**, pp. 2034-2036.

45. Levey, C. G., Etemad, S., and Inam, A., 1992, "Optically Detected Transient Thermal Response of High T_c Epitaxial Films," Applied Physics Letters, **60**, pp. 126-128.

46. Marshall, C. D., Fishman, I. M., and Fayer, M. D., 1991, "Ultrasonic Wave Propagation and Barrier-Limited Heat Flow in Thin Films of $YBa_2Cu_3O_{7-x}$," Physical Review B, **43**, pp. 2696-2699.

47. Leung, M., Hsieh, C. K., and Goswami, D. Y., 1998, "Prediction of Thermal Contact Conductance in Vacuum by Statistical Mechanics," ASME Journal of Heat Transfer, **120**, pp. 51-57.

48. Kelkar, M., Phelan, P. E., and Gu, B., 1997, "Thermal Boundary Resistance for Thin-Film High-T_c Superconductors at Varying Interfacial Temperature Drops," International Journal of Heat and Mass Transfer, **40**, pp. 2637-2645.

49. Little, W. A., 1959, "The Transport of Heat between Dissimilar Solid at Low Temperature," Canadian Journal of Physics, **37**, pp. 334-349.

50. Phelan, P. E., 1998, "Application of Diffuse Mismatch Theory to the Prediction of Thermal Boundary Resistance in Thin-Film High-T_c Superconductors," ASME Journal of Heat Transfer, **120**, pp. 37-43.

51. Chen, G., 1997, "Size and Interface Effects on Thermal Conductivity of Superlattices and Periodic Thin-Film Structures," ASME Journal of Heat Transfer, **119**, pp. 220-229.

52. Chen, G., 1998, “Thermal Conductivity and Ballistic-Phonon Transport in the Cross-Plane Direction of Superlattices,” Physical Review B, **57**, pp. 14958-14973.

53. Capinski, W. S. and Maris, H. J., 1996, “Thermal Conductivity of GaAs/AlAs Superlattices,” Physica B, **220**, pp. 699-701.

54. Zeng, T., and Chen, G., 2001, “Phonon Heat Conduction in Thin Films: Impacts of Thermal Boundary Resistance and Internal Heat Generation,” ASME Journal of Heat Transfer, **123**, pp. 340-347.

55. Chantrenne, P., and Raynaud, M., 2002, Study of Phonon Heat Conduction of Metallic Solids at the Atomic Scale, 12th International Heat Transfer Conference, Grenoble, France.

56. Goldsmid, H. J., “Introduction,” in *Semiconductors and Semimetals*, *Recent Trends in Thermoelectric Materials Research I*, **69**, pp. 1-24.

57. Goldsmid, H. J., 1964, *Thermoelectric refrigeration*, Plenum Press, New York.

58. Chen, G., Dresselhaus, M. S., Dresselhaus, G., Fleurial, J. P., and Caillat, T., 2003, “Recent Developments in Thermoelectric Materials,” International Materials Reviews, **48**, pp. 45-66.

59. Min, G., and Rowe, D. M., 1999, “Cooling Performance of Integrated Thermoelectric Microcooler,” Solid-State Electronics, **43**, pp. 923-929.

60. Slack, G. A., 1995, in *CRC Handbook of Thermoelectrics*, Editor: Rowe, D. M., CRC Press, Boca Raton, pp. 407-440.

61. Nolas, G. S., Sharp, J. and Goldsmid, H. J., 2001, *Thermoelectrics Basic Principles and New Materials Developments*, Springer-Verlag, Berlin.

62. Mahan, G. D., Sales, B., and Sharp, J., 1997, “Thermoelectric Materials: New Approaches to an Old Problem,” Physics Today, **50**, pp. 42-47.

63. Chen, G., 2001, "Phonon Transport in Low-Dimensional Structures," in *Semiconductors and Semimetals, Recent Trends in Thermoelectric Materials Research III*, **71**, pp. 203-259.

64. Dresselhaus, M. S., Dresselhaus, G., Sun, X., Zhang, Z., Cronin, S. B., and Koga, T., 1999, "Low-Dimensional Thermoelectric Materials," Physics of the Solid State, **41**, pp. 679-682.

65. Dresselhaus, M. S., Lin, Y. M., Cronin, S. B., Rabin, O., Black, M. R., Dresselhaus, G., and Koga, T., 2001, "Quantum Wells and Quantum Wires for Potential Thermoelectric Applications," in *Semiconductors and Semimetals, Recent Trends in Thermoelectric Materials Research III*, **71**, pp. 1-121.

66. Ettenberg, M. H., Jesser, W. A. and Rosi, F. D., 1996, "A New n-type and Improved p-type Pseudo-ternary $(Bi_2Te_3)(Sb_2Te_3)(Sb_2Se_3)$ Alloy for Peltier Cooling," Proceeding of 15th International Conference on Thermoelectrics, IEEE, Piscataway, NJ, pp. 52-56.

67. Polvani, D. A., Meng, J. F., Meng, Chandra Shekar, N. V., Sharp, J. and Badding, J. V., 2001, "Large Improvement in Thermoelectric Properties in Pressure-Tunned p-Type $Sb_{1.5}Bi_{0.5}Te_3$," Chemistry of Materials, **13**, pp. 2068-2071.

68. Hsu, K. F., Loo, S., Guo, F., Chen, W., Dyck, J. S., Uher, C., Hogan, T., Polychroniadis, E. K. and Kanatzidis, M. G., 2004, "Cubic $AgPb_mSbTe_{2+m}$: Bulk Thermoelectric Materials with High Figure of Merit," Science, **303**, pp. 818-821.

69. Venkatasubramanian, R., Siivola, E., Colpitts, T., and O'Quinn, B., 2001, "Thin-Film Thermoelectric Devices with High Room-Temperature Figures of Merit," Nature, **413**, pp. 597-602.

70. Yao, T., 1987, "Thermal Properties of GaAs/AlAs Superlattices," Applied

Physics Letters, **51**, pp. 1798-1800.

71. Yu, X. Y., Chen, G., Verma, A., and Smith, J. S., 1995, "Temperature Dependence of Thermophysical Properties of GaAs/AlAs Periodic Thin Film Structure," Applied Physics Letters, **67**, pp. 3553-3556.
72. Cahill, D. G., 1990, "Thermal Conductivity Measurement from 30 to 750K: the 3ω Method," Reviews of Scientific Instruments, **61**, pp. 802-808.
73. Lee, S. M., Cahill, D. G., and Venkatasubramanian, R., 1997, "Thermal Conductivity of Si-Ge Superlattices," Applied Physics Letters, **70**, pp. 2957-2957.
74. Huxtable, S. T., Abramson, A. R., Tien, C. L., Majumdar, A., LaBounty, C., Fan, X., Zeng, G., Bowers, E., Shakouri, A., and Croke, E. T., 2002, "Thermal Conductivity of Si/SiGe and SiGe/SiGe Superlattices," Applied Physics Letters, **80**, pp. 1737-1739.
75. Yang, B., Liu, J. L., Wang, K. L., and Chen, G., 2002, "Simultaneous Measurements of Seebeck Coefficient and Thermal Conductivity across Superlattice," Applied Physics Letters, **80**, pp. 1758-1760.
76. Lee, S. M., and Cahill, D. G., 1997, "Heat Transport in Thin Dielectric Films," Journal of Applied Physics, **81**, pp. 2590-2595.
77. Kurpisz K. and Nowak A.J., 1996, *Inverse Thermal Problem*, CMP, Southampton.
78. Beck, J. V., Blackwell, B., and St. Clair, C. R., 1985, *Inverse Heat Conduction*: *Ill-Posed Problem*, Wiley, New York.
79. Beck, J. V., and Arnold, K. J., 1977, *Parameter Estimation in Engineering and Science*, Wiley, New York.
80. Alifanov, O. M., 1994, *Inverse Heat Transfer Problems*, Springer-Verlag, Berlin.

81. Weber, C. F., 1981, "Analysis and Solution of the Ill-Posed Inverse Heat Conduction Problem," International Journal of Heat and Mass Transfer, **24**, pp. 1783-1792.

82. Chen, H. T., and Chang, S. M., 1990, "Application of the Hybrid Method to Inverse Heat Conduction Problems," International Journal of Heat and Mass Transfer, **33**, pp. 621-628.

83. Bayo, E., Moulin, H., Crisalle, O., and Gimenez, G.., 1992, "Well-Conditioned Numerical Approach for the Solution of the Inverse Heat Conduction Problem," Numerical Heat Transfer, Part B, **21**, pp. 79-98.

84. Raynaud, M. and Bransier J., 1986, "A New Finite-Difference Method for the Nonlinear Inverse Heat Conduction Problem," Numerical Heat Transfer, **9**, pp. 27-42.

85. Menart, J., 1999, "Radiative Transport in a Two-Dimensional Axisymmetric Thermal Plasma Using the S-N Discrete Ordinates Method a Line-By-Line Basis," J. Quantitative Spectroscopy & Radiative Transfer, **67**, pp. 271-291.

86. Popov, V. N., 2004, "Carbon Nanotubes: Properties and Application," Materials Science and Engineering R, **43**, pp. 61-102.

87. Eastman, J. A., Choi, S. U. S., Li, S., Yu, W., and Thompson, L. J., 2001, "Anomalously Increased Effective Thermal Conductivities of Ethylene Glycol-Based Nanofluids Containing Copper Nanoparticles," Applied Physics Letters, **78**, pp. 718-720.

88. http://www.marlow.com

89. Huxtable, S. T., 2002, *Heat Transport in Superlattices and Nanowire Arrays*, Ph. D. Thesis, University of California, Berkeley.

90. Modest, M. F., 1993, *Radiative Heat Transfer*, McGraw-Hill, Inc., New York.

91. Lauhon, L. J., Gudiksen, M. S., Wang, D., and Lieber, C. M., 2002, "Epitaxial Core-Shell and Core-Multishell Nanowire Heterostructures," Nature, **420**, pp. 57-61.

92. Chen, G., 1996, "Heat Transport in the Perpendicular Direction of Superlattices and Periodic Thin-Film Structures," Proceedings of the ASME International Mechanical Engineering Congress and Exposition (Atlanta, GA), Micro-Electro-Mechanical Systems (MEMS), Dynamic Systems and Control Div., Vol. 59, American Society of Mechanical Engineers, New York, pp. 13-24.

93. Holman, J. P., 1992, *Heat Transfer*, McGraw Hill Inc., London.

94. Goodson, K. E., Käding, O. W., Rösler, M., and Zachai, R., 1995, "Experimental Investigation of Thermal Conduction Normal to Diamond-Silicon Boundaries," Journal of Applied Physics, **77**, pp. 1385-1392.

95. Partridge, P. G., Lu, G., May, P., and Steeds, J. W., 1995, "Potential High-Strength High Thermal Conductivity Metal-Matrix Composites Based on Diamond Fibres," Diamond and Related Materials, **4**, pp. 848-851.

96. Anthony, T. R., Banholzer, W. F. and Fleischer, J. F., 1990, "Thermal Diffusivity of Isotopically Enriched C-12 Diamond," Physical Review B, **42**, pp. 1104-1111.

97. da Silva, L. W., and Kaviany, M., 2004, "Micro-Thermoelectric Cooler: Interfacial Effects on Thermal and Electrical Transport," International Journal of Heat and Mass Transfer, **47**, pp. 2417-2435.

98. Fan, X., Zeng, G., LaBounty, C., Bowers, J. E., Croke, E., Ahn, C. C., Huxtable, S., Majumdar, A., and Shakouri, A., 2001, "SiGeC/Si Superlattice Microcoolers," Applied Physics Letters, **78**, pp.1580-1582.

99. Wu, Y., Fan, R., and Yang, P., 2002, "Block-by-Block Growth of Single-Crystalline Si/SiGe Superlattice Nanowires," Nano Letters, **2**, pp. 83-86.

100. Touzelbaev, M. N., Zhou, P., Venkatasubramanian R., and Goodson, K. E., 2001, "Thermal Characterization of Bi_2Te_3/Sb_2Te_3 Superlattices," Journal of Applied Physics, **90**, pp. 763-767.

101. Touloukian, Y. S., Powell, R. W., Ho, C. Y., and Klemens, P. G., 1970, *Thermophysical Properties of Matter*, Plenum, New York.

102. Lin, J. H., Chen, C. K., and Yang, Y. T., 2000, "The Inverse Estimation of the Thermal Boundary Behavior of a Heated Cylinder Normal to a Laminar Air Steam," International Journal of Heat and Mass Transfer, **43**, pp. 3991-4001.

103. D' Souza, N., 1975, "Numerical Solution of One-Dimensional Inverse Transient Heat Conduction by Finite Difference Method," ASME Paper No. 75-WA/HT-81.

104. Ruperti, N. J., Raynaud, M., and Sacadura, J. F., 1996, "A Method for the Solution of the Coupled Inverse Heat Conduction-Radiation Problem," ASME Journal of Heat Transfer, **118**, pp. 10-17.